Freezing and melting behaviors of aqueous multiwall carbon nanotube nanofluids

Jason Ivall

Department of Chemical Engineering
McGill University
Montréal, Québec

August 2016

A thesis submitted to McGill University in partial fulfillment of the requirements of the degree of Doctor of Philosophy

Abstract

This thesis investigates the freezing and melting behaviors of aqueous, oxygen-functionalized multiwall carbon nanotube (f-MWCNT) nanofluids in order to provide a more complete understanding of the effects of the phase change process on the colloidal system. The solidification behavior of f-MWCNT nanofluids was assessed over a range of temperature driving forces through visual characterization of droplet morphology. It was found that the degree of f-MWCNT inclusion into the fully solidified droplet was strongly related to driving force, and by extension, crystallization velocity. Low crystallization speeds led to complete expulsion of f-MWCNTs from the frozen droplet, while increasing crystallization speeds allowed for greater f-MWCNT inclusion inside the solid, seemingly within void spaces such as air volumes and grain boundaries. Even at the highest driving force applied, the critical velocity needed for f-MWCNT incorporation into the ice matrix was not reached. The freezing process resulted in the clustering of the f-MWCNTs and an ultimately destabilized colloidal system. The melting behavior of the solidified droplet was then investigated through similar visual characterization of pure water and MWCNT-containing systems. The sessile droplets were melted from below over a range of temperatures. Tracking of MWCNT clusters revealed the occurrence of rapid convective cells in the liquid during melting. This circulation was conditional on the presence of floating ice within the system, as convective cells quickly degraded following the disappearance of the ice phase. Visual characterization of the flow fields, evaluations of the direction of circulation patterns, and dimensionless analysis of temperature-dependent convective forces strongly supported a thermocapillary (surface-tension)-driven transport mechanism. The presence of MWCNT clusters was shown to increase melting times compared to pure water samples as a result of interfering with surface tension effects. Finally, the long-term stability of f-MWCNT nanofluids was assessed over the course of repeated phase change cycling. Though some MWCNT clusters formed during the crystallization part of the freeze/thaw cycles, ultrasonication was sufficient to break them apart and redisperse the nanofluids. Concentration and particle size analyses demonstrated moderate

recoverability of initial attributes, and XPS and zeta potential measurements indicated the preservation of oxygen content on f-MWCNT surfaces. The clustering of f-MWCNTs during phase change is likely a reversible process, which is promising for the use of f-MWCNT nanofluids in liquid/solid phase change processes.

Résumé

Cette thèse a comme objectif d'étudier le comportement des nanofluides aqueux composés de nanotubes de carbone multi-parois fonctionnalisés avec l'oxygène (f-NTCMP) au cours du gel et de la fonte afin de fournir une compréhension plus complète des effets du processus de changement de phase sur le système colloïdal. Le comportement des nanofluides f-NTCMP lors de la congélation a été évalué sur une gamme de températures induisant le processus (force motrice) via la caractérisation visuelle de la morphologie des gouttelettes. Il a été constaté que le degré d'inclusion des f-NTCMPs à l'intérieur d'une gouttelette complètement solidifiée est fortement lié à la force motrice, et par extension la vitesse de cristallisation. Les faibles vitesses de cristallisation ont mené à l'expulsion complète des f-NTCMP de la phase solide, tandis que des vitesses de cristallisation plus élevées ont permis une plus grande inclusion de f-NTCMPs à l'intérieur du solide. Les espaces vides tels que les volumes d'air et les joints de grains sont apparemment plus précoces à cette inclusion. La vitesse critique nécessaire pour l'incorporation des NTCMPs dans la matrice de la glace n'a jamais été atteinte dans la gamme de forces motrices utilisée. Le processus de congélation a entrainé le regroupement des f-NTCMPs, et ultimement la déstabilisation du système colloïdal. La fonte de la goutte solidifiée a ensuite été étudiée visuellement en comparant les comportements de l'eau pure à des nanofluides NTCMPs aqueux. Les gouttelettes sessiles ont été fondues en appliquant de la chaleur à leur base et sur une gamme de températures. La visualisation des amas de NTCMPs a révélé l'existence de cellules de circulation rapides dans le liquide pendant la fonte. L'existence de ces circulations de fluide était conditionnelle à la présence de glace flottante à l'intérieur du système, car les mouvements de circulation s'atténuent rapidement lorsque la glace disparait. L'observation des champs d'écoulement, l'évaluation quantitative des directions de circulation, et une analyse adimensionnelle des forces en jeu appuient l'hypothèse que les mouvements de liquides sont causés par un effet thermocapillaire induit par le gradient de tension superficielle, lui-même induit par le gradient de température. Il a été démontré que la présence d'amas de NTCMPs augmente le temps de fonte

comparativement aux échantillons d'eau pure. Cette augmentation est la conséquence d'interférence des effets de tension superficielle. Enfin, la stabilité à long terme des nanofluides de f-NTCMPs a été évaluée sous conditions de gel-dégel cyclique. Bien que des amas de f-NTCMPs se forment durant les phases de cristallisation des cycles gel-dégel, une sonification intense est suffisante pour briser les amas et assurer une ré-dispersion complète. Les analyses de concentration et de taille des particules ont démontré une récupération partielle des attributs initiaux. L'analyse de la chimie de surface des f-NTCMPs par SPX et les mesures de potentiel zêta ont démontré que la teneur en oxygène est maintenue. La formation d'amas de f-NTCMPs durant le changement de phase semble donc être un processus réversible, ce qui est prometteur pour l'utilisation des nanofluides de f-NTCMP dans les applications de changement de phase liquide/solide.

Acknowledgements

A thesis might have one name on it, but you get a lot of help along the way. First and foremost I would like to thank my supervisor Dr. Phillip Servio for the incredible years at graduate school. The freedom to explore curiosities, the opportunities to attend conferences in Edinburgh and Calgary, and the unwavering support have made for a truly enriching experience. The friendship, the humor, the stories, and the Halo® nights are what made this adventure so special. I would also like to thank Dr. Sylvain Coulombe for the keen insight, a most meticulous eye for detail, and an inspiring pursuit of discovery.

To current and former colleagues of the hydrate crew: This experience would never have been the same without the close-knit group that we had. As an outsider coming in from a different background, it's been quite the learning process, and I'm much obliged for your support. Dany you took me under your wing, and after all these years I finally see the wisdom in "tighten more and don't touch it… and don't tell Frank". Edwin, the care and devotion you put into all things you do is an inspiration. I still can't believe that winter gear is an all-season outfit for you, but I suppose the Canadian climate is always colder than…Singapore? Seb as my MWCNT dealer, coder and homebrew consultant, none of my projects would have taken off without your expertise. Oleg thank you for your astute insights into the world of droplets and for the pointers on operating a camera (that goes for you too Faraz, especially surrounding the software). Once you get it figured out it really is like riding a bicycle. Thomas thanks so much for hosting our soirées, and Matt and Paul, thanks for all the neighborly chats and coffee boosts; nothing gets you buzzed like a sip from your caffeinated sludge.

Special thanks go out to James, Francis and Jon for the pleasant conversations and countless unforgettable moments. Jon I've never met a better teacher, and I relished in all our exchanges on philosophical points. James, mellonamin. Lle holma ve' edan. Aa' menle nauva calen ar' ta hwesta e' ale'quenle. Francis, getting a Ph.D. is one thing, but

winning a championship is on a whole other level and I'm stoked that we got to share in the glory together as our legend lives on in the annals of intramural recreational hockey.

No setups would have been possible without the savvy expertise of the technical staff. Andrew Golsztajn, Lou Cusmich, Ranjan Roy, Gerald Lepkyj, and particularly Frank Caporuscio, I thank you all tremendously for you generous time and efforts. Whatever troubles we had, you had an answer for it. I strived to soak up as much knowledge as I could, a monumental task. To the Machine Shop crew, Roberto Tariello, Csaba Szalacsi and Raymond Lemay, your input into the design was invaluable and the quality of your work is second to none. To Melanie Gorman and Lisa Volpato, your cheerful help and regular reminders were key in getting my work done promptly. For all the heavy lifting of the endless paperwork, thanks to Louise Miller-Aspin and especially Jo-Ann Gadsby, who was always there in 3A with a warm welcome and an eagerness to help.

To the other professors in the Department with whom I've had the opportunity to interact: Professors Rey, Leask, Omanovic, Gostick, Maríc and Kietzig. It's a privilege to be surrounded by such great minds that challenge your understanding and broaden your knowledge, which makes for a genuinely scholastic experience. I would also like to extend this sentiment to Nathan, Larissa, and Adya, who fielded countless questions pertaining to nanotubes with the patience and knowledge of true scholars.

The steadfast support from my family – my parents, my sister, my grandparents, my parents-in-law, the siblings-in-law, Pip– and my friends has been fundamental to the completion of my very prolonged studies. You're always there for me, and I'm very grateful for it.

And Elena, my darling. You probably know just as much as I do about my thesis by now, likely more. You've always been my anchor, patiently listening, encouraging, advising, and feeding me at every step. I can't tell you how much I appreciate the unconditional love and support that you give. I love you so much, and I can't wait to share all of our next adventures with you!

Financial Support

Innovation is the foundation of progress, and new ideas and different approaches are instrumental to global development. Research programs such as graduate school help to educate, inspire and broaden the perspectives of those who pass through it, and the better one understands the world, the better one can shape it. Funding is the core of every research program, and I would like to thank the following agencies for financial support over the course of the various projects:

- The Natural Sciences and Engineering Research Council of Canada (NSERC)
- The Fonds de recherche du Québec – Nature et technologies (FRQNT)
- The Canada Research Chair program (CRC)
- Imperial Oil

The financial assistance provided by student scholarship programs allows more focus to be directed to your research and also supports the pursuit of other endeavors. This enriches the graduate student experience and I truly believe leads to more well-rounded individuals. For personal funding, I am grateful to the following agencies:

- The Fonds de recherche du Québec – Nature et technologies (FRQNT) for both the Masters (B1) and Doctoral (B2) scholarships
- The McGill Engineering Doctoral Award (MEDA) provided by the Faculty of Engineering at McGill. This award is made possible by generous donations from numerous benefactors to the Faculty, and I was privileged to receive my award as a fellowship in the name of the following donors:
    - The Vadasz Fellowship
    - The Hydro-Québec Fellowship
- The Department of Chemical Engineering at McGill University

Contents

List of Figures

List of Tables

List of Abbreviations

CI	Confidence interval
CNT	Carbon nanotube
CTES	Cool thermal energy storage
CVD	Chemical vapor deposition
DF	Driving force
DLS	Dynamic light scattering
DLVO	Derjaguin-Landau-Verwey-Overbeek
DS	Degree of supercooling
f-MWCNT	Functionalized MWCNT
LHTES	Latent heat thermal energy storage
MWCNT	Multiwall carbon nanotube
p-MWCNT	Pristine MWCNT
PCM	Phase change material
PDI	Polydispersity index
PS	Particle size
PTFE	Polytetrafluoroethylene
SDS	Sodium dodecyl sulfate
SS	Stainless steel
SHSES	Sensible heat thermal energy storage
TE	Thermoelectric
TES	Thermal energy storage
XPS	X-ray photoelectron spectroscopy
ZP	Zeta potential

Contributions of Authors

This thesis is organized as a manuscript-based document consisting of two published peer-reviewed articles, and one article that has been submitted for consideration to a peer-reviewed journal. The author of this dissertation was responsible for the conceptualization, the literature search, the experimental design, the experimental work, as well as the data analysis for each study, together with the writing and preparation of each article. As the major contributor to all of the studies, the present author is listed as first author on all of the articles. Co-authors Hachem and Langlois-Rahme conducted experimental replicates as part of summer research projects. Co-author Renault-Crispo developed the MATLAB® script required for the particle tracking software and synthesized multiwall carbon nanotube samples. Co-authors Coulombe and Servio provided guidance as supervisors of this doctoral research project.

- Ivall, J., Hachem, M., Coulombe, S., Servio, P. Behavior of surface-functionalized multiwall carbon nanotube nanofluids during phase change from liquid water to solid ice. *Cryst. Growth Des.* 2015, 15 (8), 3969-3982.

- Ivall, J., Renault-Crispo, J. -S., Coulombe, S., Servio, P. Ice-dependent liquid-phase convective cells during the melting of frozen sessile droplets containing water and multiwall carbon nanotubes. *Int. J. Heat Mass Transfer*. 2016, 101, 27-37.

- Ivall, J., Langlois-Rahme, G., Coulombe, S., Servio, P. Quantitative analysis into the stability of aqueous oxygen-functionalized multiwall carbon nanotube nanofluids after liquid/solid phase change cycling (submitted for consideration to *Nanotechnology*, 2016).

Original Contributions

The original contributions to knowledge provided by this work can be summarized as follows:

- An explicit investigation into the solidification behavior of aqueous f-MWCNT nanofluid systems through a morphological analysis.

- Associating temperature driving force and crystallization velocities to the morphology of freezing systems, and providing insights into the critical velocities required for f-MWCNT inclusion into the solid ice matrix.

- Discovery of thermocapillary-driven convective processes occurring within melting sessile droplets composed of water and ice.

- Determination of the impact of MWCNT clusters on the melting of frozen sessile water droplets.

- Quantitative evaluation of bulk stability of f-MWCNT nanofluids after repeated freeze/thaw cycles. Characterization of the functional groups on the MWCNT surface after phase change cycling.

- Assessments of the clustering mechanism of MWCNTs as a result of the phase change process.

- Observing cation leaching from borosilicate glass and linking this occurrence to long-term f-MWCNT nanofluid stability.

Chapter 1

Introduction

The phase change of water between liquid and solid states is a universal process that is continuously studied in order to gain a better understanding of the physical processes controlling both the natural environment and our man-made technologies. Historically, water/ice systems have been largely employed in refrigeration applications. Recently, attention has turned to using water-based phase change technologies for thermal energy storage and temperature control in building spaces owing to the economic, energetic and environmental benefits they offer. Incorporating nanotechnology into the design can further enhance these savings. Many research factions seek to modify the properties of the phase change process – and of the liquid or solid systems themselves – through the addition of nanomaterials. Multiwall carbon nanotubes (MWCNTs) stand out amongst these candidates with some of the best mechanical, electrical and thermal properties known to date.

In the literature, MWCNT-based nanofluids have shown great promise as enhancers of the crystallization process of water. While the outlook is bright, a great deal of research is still required to fully characterize these systems and fill certain knowledge gaps. With regards to the crystallization process, the dispersibility of MWCNTs into the solid phase must be considered since it is closely linked to its material properties and the overall stability of the colloid. The melting side of the phase change process has received considerably less attention, and it is thus important to understand the effects that MWCNTs may have on the transport phenomena controlling the melting process. Finally, the stability of MWCNT nanofluid dispersions must be tested over multiple phase change cycles to evaluate their long-term performance. All of these

studies provide a more complete understanding of the mutual effects that the phase change of water and MWCNT nanofluids have on each other.

This thesis explores each of these questions. Chapter 2 offers pertinent information to complement the material covered in subsequent chapters. Owing to the multidisciplinary nature of this work, this background section is structured thematically. The first section (2.1) focuses on water, its properties and the essentials of crystallization and melting theory. This outlines the basic principles that underlie the stability of aqueous MWCNT nanofluids, as well as the phenomena observed in Chapters 3 and 4, respectively. The second section (2.2) discusses various facets of multiwall carbon nanotubes that are relevant to assessing nanofluid behavior. Chapter 2 concludes with the intersection of the two fields and gives an overview of the work that has been conducted surrounding MWCNT nanofluids and liquid/solid phase change. Chapter 3 examines the crystallization behavior of f-MWCNT nanofluids across a range of temperature driving forces through a morphological analysis. Chapter 4 investigates the melting behaviors of frozen aqueous MWCNT nanofluid systems and evaluates the transport phenomena occurring in melting water droplets. Chapter 5 examines the effect of phase change on f-MWCNT functional groups and assesses the long-term stability of nanofluids over the course of extended phase change cycling.

Chapter 2

Background

2.1 Water

Water is the most abundant substance on the surface of Earth. Its existence in three phases - vapor, liquid, and solid – and its continuous conversion between these states makes up the hydrological cycle that governs the geophysical and biological processes occurring on our planet. The evaporation and condensation of water generates far-reaching convective atmospheric wind currents that dictate globate climate and weather patterns. The seasonal freezing and melting processes on surface waters in oceans, lakes, rivers, etc., is responsible for large-scale ocean currents and river swells, and is essential to the preservation of the marine life beneath. The commonality between all these phenomena is the perpetual exchange of energy, a process that is enabled by water's unique ability to absorb vast quantities of it, both during phase change (latent heat capacity) and within a given phase (sensible heat capacity). This buffering property is essential to the energy storage and transfer processes at all scales. Not only does water support life as a biological ingredient, but its material properties are equally important to the shaping of our natural environment.

From an anthropocentric perspective, the use of water has been integral to the development of society, and today's industrial processes are heavily reliant on water's distinctive properties. Water is an abundant, inexpensive, non-toxic, non-flammable and versatile solvent suitable for myriad manufacturing and resource transformation processes. Its ability to absorb large quantities of heat without a large change in temperature make it ideal for heat transfer and thermal energy storage (TES)

applications. Liquid water boasts one of the highest sensible heat capacities and is used extensively as a working fluid in heat exchangers, geothermal and solar energy harvesting, as well as coolants in nuclear and thermal power plants (Andrews and Jelley, 2013). Due to its high latent heat of evaporation, water is a common working fluid in many Rankine-based thermal power plants, and its high latent heat of fusion makes it a universal material for refrigeration and cooling applications.

Many of water's signature chemical and physical properties are governed by its ability to hydrogen bond (H-bond), a feature exclusive to a very small group of substances. Two main electronic attributes contribute to this effect: a fixed charge separation within the molecule and the spatial arrangement of these charged regions. The high electronegativity of the oxygen atom draws electrons from its two hydrogen atoms toward its two lone pairs, producing a negatively-charged pole and two positively-charged poles. The asymmetric bent molecular geometry then leads to a net dipole moment. Water's strong polarity gives rise to one of the highest dielectric constants of all liquids, and also affords it an amphoteric character, as it self-ionizes into a hydronium cation (H_3O^+) and hydroxide anion (OH^-) (Geissler et al., 2001). This property makes it the "the universal solvent" capable of dissolving a wide range of substances (Lynden-Bell et al., 2010). H-bonding between water molecules arises from these electrostatic dipole-dipole interactions as electron-poor hydrogen atoms seek out electron-rich lone pairs on other oxygen atoms. Each water molecule is capable of forming four H-bonds, and in a liquid state, H-bonding networks are a dynamic occurrence as bonds are continuously switched between molecules (Eaves et al., 2005). The energy of a single H-bond is relatively weak, but the cumulative association of water molecules can yield some very substantial effects. These strong cohesive forces afford it one of the highest surface tension of all liquids, as well as anomalously high melting and boiling temperatures for its molecular size (Lynden-Bell et al., 2010). H-bonding is also responsible for its high specific heat capacity (4.18 J/g-K at 25 °C), latent heat of fusion (334 J/g) and latent heat of vaporization (2261 J/g) (Perry and Green, 1997). The final peculiarities of water that are relevant to this thesis are that its maximum liquid density occurs at 4 °C, not at its melting point, and that its crystal form is less dense than its liquid form. The thermal expansion it experiences from 4 °C to 0 °C is brought on by the

coordination of molecules into the more restricted and expanded hexagonal network of H-bonding that resembles its crystalline form.

2.1.1 Crystallization

Crystallization involves the organization of molecules into a highly ordered, periodic, and typically rigid lattice. To date, pure water has been experimentally observed to assume 17 unique crystal structures, depending on temperature and pressure (Petrenko and Whitworth, 2002; Falenty et al., 2014). Most ice formed on earth (i.e. ordinary ice) exists as the Ih structure, shown in Figure 2.1 (Pauling, 1935). This configuration is completely delineated by hydrogen bonding where the ideal or perfect crystalline structure conforms to the aptly named "ice-rules" outlined by Bernal and Fowler (1933). These rules state that each oxygen atom is coordinated with four hydrogen atoms (two covalently, two H-bonded), and only one hydrogen atom is present between any two oxygen atoms. This makes for a near-perfect tetrahedral packing (109.5°) of water molecules, and gives rise to a very stable matrix. The overall crystal lattice exhibits a hexagonal symmetry with a relatively open packing, which explains the approximately 9 % increase in volume of ice Ih compared to liquid water (at 0 °C). This rare attribute is essential to the existence of aquatic life, as the floating of ice allows for their survival in the liquid depths beneath, and also insulates them from further cooling effects (Tyson, 2014). There is no long-range order in the arrangement of water molecules or the hydrogen bonds in the ice Ih structure (Petrenko and Whitworth, 2002). Water may adopt six different geometric H-bond configurations with its neighbors. While the positions of oxygen atoms are topologically fixed, those of the hydrogen atoms are more flexible, and this disorder is tolerated as long as the Bernal-Fowler rules are satisfied (Bartels-Rausch et al., 2012).

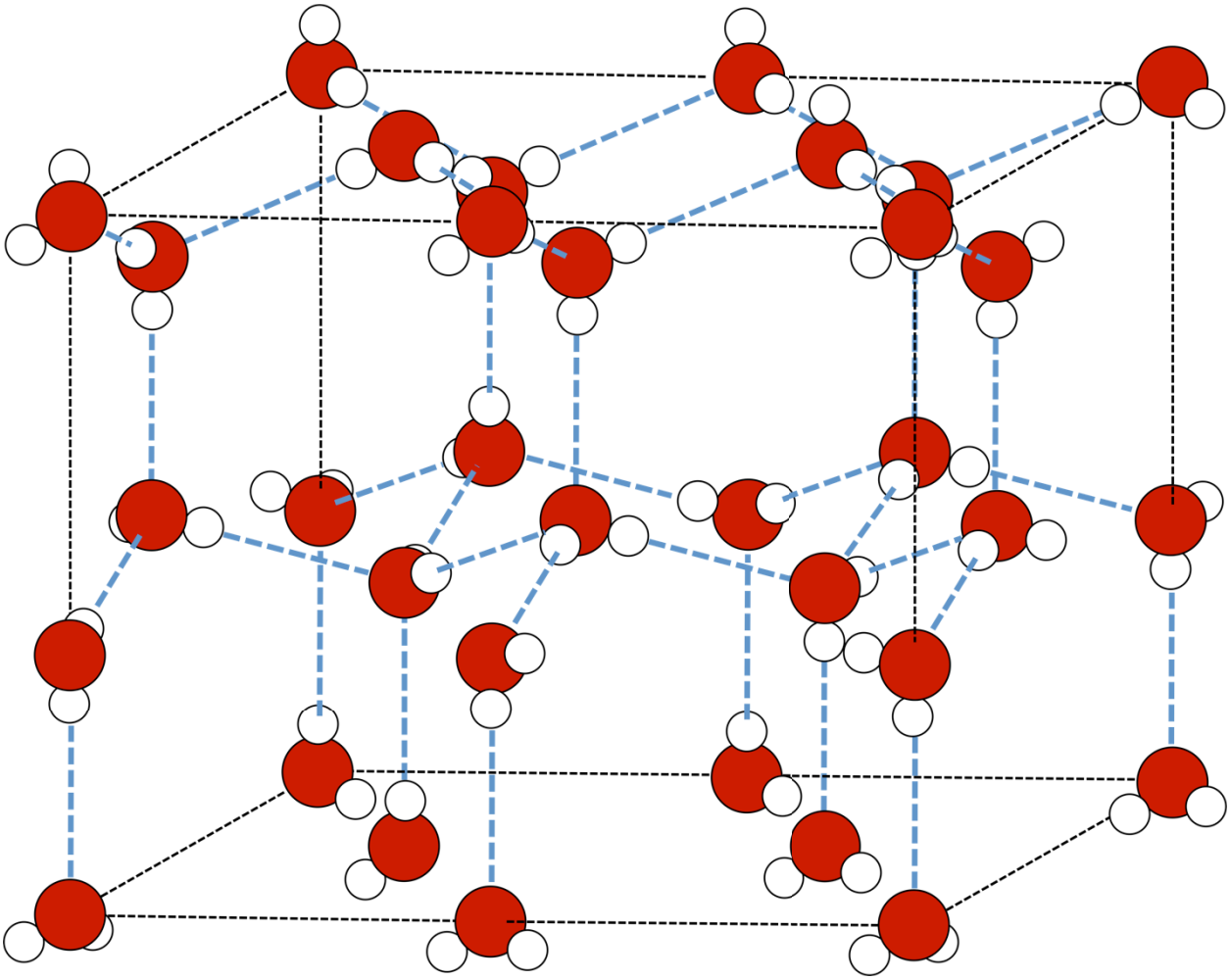

Figure 2.1: Crystal structure of ice Ih (adapted from Fletcher (1970)). Red circles: oxygen atoms; white circles: hydrogen atoms; dashed blue lines: hydrogen bonds.

The crystallization of water may proceed at any temperature below 0 °C (at atmospheric pressure), as a system at equilibrium remains unchanged. The driving force for crystallization, also known as the degree of supercooling, is defined as the magnitude of the difference between the system temperature (T_S) and the equilibrium temperature (T_{EQ} = 0 °C). Once supercooled, crystallization is controlled by both thermodynamic and kinetic factors, and proceeds through two major steps: nucleation and growth. In terms of thermodynamics, the decrease in entropy suffered by the system (ΔS_{SYS}) in becoming a more ordered state is overcompensated by an increase in entropy to the environment (ΔS_{SURR}) caused by exothermic heat release from crystallization (ΔH_f) (Equation 2.1). Multiplying Eq. 2.1 through by ($-T$) gives the expression for Gibbs free energy

(Equation 2.2). Phase change is spontaneous when the temperature drops below equilibrium, and it is a solely entropy-driven process.

$$\Delta S_{Total} = \Delta S_{SURR} + \Delta S_{SYS} = -\frac{\Delta H_f}{T} + \Delta S_{SYS} \quad \text{Eq. 2.1}$$

$$\Delta G = \Delta H_f - T\Delta S_{SYS} \quad \text{Eq. 2.2}$$

With the creation of a volume of crystal phase comes the generation of a new interface within the system. The total change in free energy associated with nucleation can be formulated by the contribution of each energetic effect:

$$\Delta G = \Delta G_S + \Delta G_V = \frac{4}{3}\pi r^3 \Delta g_V + 4\pi r^2 \sigma \quad \text{Eq. 2.3}$$

where ΔG is the overall excess free energy, ΔG_S is the surface excess free energy associated with the creation of a new interface, ΔG_V is the volume excess free energy associated with the creation of the solid, r is the radius of the solid crystal (assumed to be spherical), Δg_V is the free energy change of crystallization per unit volume, and σ is the liquid/solid interfacial or surface tension. The exothermic nature of crystallization makes ΔG_V a negative quantity, while the formation of a new interface requires work and makes ΔG_S a positive quantity. Therefore, despite favorable formation conditions, crystal growth is hindered by interfacial tension. The addition of surface and volume terms as a function of crystal size causes a maximum value in ΔG (ΔG_C) at what is known as the critical radius (r_C). The critical radius represents the minimum stable cluster size beyond which growth constitutes a reduction in free energy (Mullin, 2001). Spontaneously-formed clusters that fall below this size dissolve, and the liquid must reorganize until r_C is attained and sustained growth can proceed. The nucleation stage thus describes a metastable period in which the system continuously attempts to overcome this energetic barrier. Nucleation is by nature a stochastic and unpredictable process, and water especially is known for extended nucleation periods (Wilson and Haymet, 2012). The above expressions apply for the case of homogeneous nucleation and denote the maximum activation energy required. Nucleation is greatly assisted by

the presence of impurities (surfaces, interfaces, colloidal particles, etc.). These foreign bodies provide a surface onto which precursor clusters can assemble. This reduces the contribution of surface tension energies, which in turn reduces the maximum activation energy ΔG_C by a factor of ϕ, where $0 \leq \phi \leq 1$ (Equation 2.4). Nucleation is facilitated by requiring a smaller critical volume and hence less molecules to form the critical cluster, and it can be induced at lower degrees of supercooling. Heterogeneous nucleation is widely accepted as being the universal occurrence (Mullin, 2001).

$$\Delta G_C' = \phi \Delta G_C \qquad \text{Eq. 2.4}$$

Growth follows a nucleation event and it can be divided into three broad kinetic steps (Glicksman et al., 1994). In some cases, an initial spread of crystal may occur that lasts on the order of < 1 second. This formation is more prominent at greater supercoolings, but is always a self-limiting process due to recalescence of the surrounding liquid (Mullin, 2001). The second and principal stage consists of the general bulk conversion of liquid into solid, and is what is usually studied experimentally. This growth process takes place in the range of minutes to hours, depending on system size and supercooling, and it is typically heat-transfer limited, as exothermic heat release must be removed from the advancing crystal front to either the bulk liquid or the solid, depending on the geometry of heat extraction. The final stage of growth consists of solid-state diffusional adjustments to remedy crystallographic defects, such as resolving grain boundaries or extruding trapped impurities. This process transpires over prolonged periods – days to months – and is therefore not as frequently considered in experimental settings (Glicksman et al., 1994). The overall rate of crystallization (typically stages 1 and 2) is a key parameter to industrial applications that is mainly influenced by the degree of supercooling. As temperature decreases, the increased rate of heat dissipation allows for an accelerated growth rate of the solid interface. The probability of nucleation also increases, producing multiple nuclei that contribute to the net conversion of material (Mullin, 2001).

The quality of the crystal structure is an important factor in dictating the material properties of ice. Many of these properties are calculated based on a chemically pure and fully developed hydrogen-bonded matrix, but these can be enormously influenced by non-ideal effects. Polycrystalline ice formed from dendrite growth and multiple nucleation centers contains grain boundaries at the intersection of crystal fronts, which reduces the strength of the ice (Petrenko and Whitworth, 2002). The presence of dissolved components in liquid water (due to its solvation power) becomes an issue for its crystal form, as the ice matrix prefers compositional homogeneity. At low crystallization speeds, the slowly developing matrix rejects impurities from the crystal front into the liquid, but this ability is overcome at higher growth rates by the propensity to freeze (Mullin, 2001). The crystallization speed at which impurities become entrapped in the solid matrix is known as the critical velocity. This parameter is influenced in concerted fashion by the chemical, physical and morphological characteristics of the impurities (Korber, 1988). Some examples of the inclusion/exclusion of foreign molecules are air bubbles trapped inside an ice cube that give it a white appearance, brine exclusion in ice formed from sea water that gives rise to thermohaline circulation, and the rejection of colloidal particles. A full understanding and prediction of the phase transition of water still remains a complex problem due to the multitude of variables affecting the system. This scenario of a two-phase, multi-component, dynamic, moving boundary system is commonly known as the Stefan problem, and significant research is devoted to simultaneously accounting for temperature gradients, cooling rates, interface morphology, and foreign particle effects in order to obtain a better model of phase transition (Hu and Argyropoulos, 1996).

2.1.2 Melting

Melting designates the breakdown of an ordered crystal lattice through the absorption of energy. Melting is an entirely heat-transport limited process; the melting rate is directly related to the applied temperature. As energy is transferred to crystal-locked molecules, vibrational motion increases until their energy overcomes the hydrogen bonding forces and the molecules become liberated. Note that freely moving liquid water molecules are closer to each other than in solid state due to the contraction of water.

An interesting aspect of the melting process of pure water that is relevant to this thesis surrounds the transport processes that may occur within the liquid. Depending on the geometry of the system, the temperature gradients in the melt can lead to density (ρ) and/or surface tension (σ) differences between fluid elements, since both phenomena are strongly influenced by temperature. These differences in forces can then generate convective flow. Density-driven flow is known as natural, gravity or thermogravitational convection. In order for thermogravitational convection to develop, the density of upper fluid elements must be greater than that of the lower fluid elements (Rayleigh, 1916). This requires a colder upper fluid volume (at $\rho+$) and a warmer lower fluid volume (at $\rho-$), shown in Figure 2.2. This happens to be a common scenario. When a body of water is frozen from the top, such as in lakes or oceans, or when a mass of ice is melted from the side or below, such as in laboratory situations involving container heating, the floating of ice at the surface cools the upper fluid elements and promotes the development of thermogravitational flow.

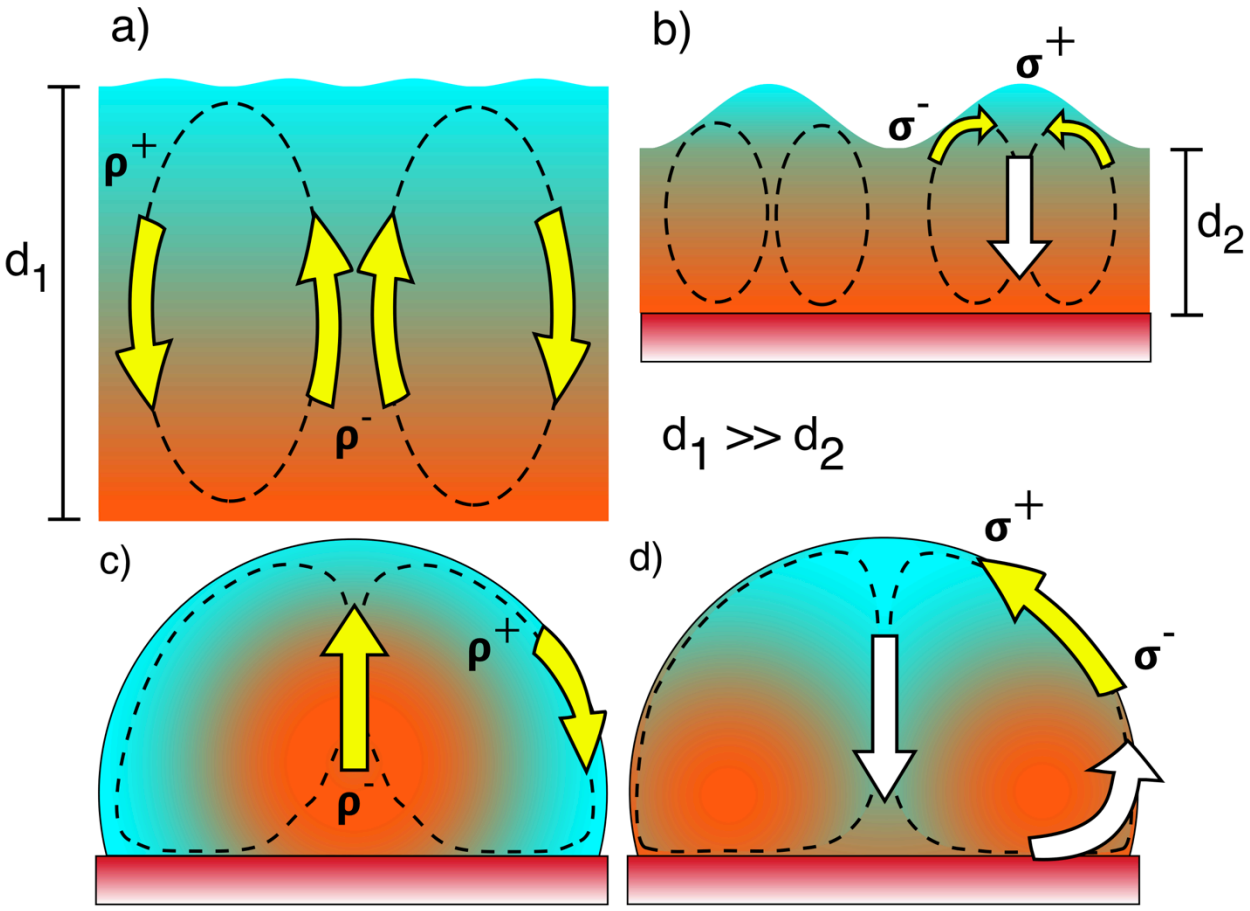

Figure 2.2: Schematic of temperature gradients (blue = colder fluid, red = warmer fluid) conducive to a) thermogravitational flow in a planar geometry; b) thermocapillary flow in a planar geometry; c) thermogravitational flow in a droplet geometry; d) thermocapillary flow in a droplet geometry. Yellow arrows designate phenomena driving convective flow. The red surface designates a heat source. Notation: (σ) surface tension, (ρ) density, (+) higher magnitude of force, (–) lower magnitude of force.

The presence of an interface in a system offers another mechanism by which temperature-dependent convective transport may develop, a phenomenon known as thermocapillary convection. Temperature gradients along an interface cause differences in surface tension whereby colder molecules (at σ+) exert a pulling force on warmer molecules (at σ–). Convective cells are established from these contractile forces at the interface and the transmission of momentum into the bulk interior (see Figure 2.2). Owing to its remarkably high cohesiveness, water is capable of experiencing large

gradients in surface tension across an interface. Furthermore, water is often found in droplet form, a geometry that boasts the highest surface area to volume ratio. Both of these factors make water particularly conducive to thermocapillary flow. This manifestation is commonly observed in the evaporation of water droplets from surfaces, however it was first discovered in thin liquid films by Bénard (1900a), which consists of a planar geometry (Figure 2.2b).

The presence of a temperature gradient in a fluid does not necessarily guarantee that thermogravitational or thermocapillary convection will develop. Both require certain conditions to be met (discussed in greater detail in Chapter 4), most notably reaching critical temperature gradients and/or critical distances over which a given temperature gradient exists. As a bulk phenomenon, thermogravitational convection usually occurs in large systems, while thermocapillary effects take place at smaller dimensions. Myriad numerical and experimental studies are directed toward analyzing different configurations of the various parameters affecting convection. These analyses are important for modeling heat transport processes governing phase change (both crystallization and melting) and are invaluable to understanding a wide range of processes ranging from droplets, to planetary systems, and to industrial applications (Lynden-Bell et al., 2010).

2.1.3 Applications of the Water/Ice Phase Change Process

An emerging application for the solid/liquid phase change of water involves its use as a phase change material (PCM) for latent heat thermal energy storage (LHTES). The high latent heat of fusion of PCMs enables the absorption and release of large quantities of energy with minimal changes in temperature. Further, the high energy storage density can be used to deliver long-lasting temperature control. Numerous materials are tested as PCMs, such as inorganics (e.g. water, metals), eutectics (e.g. water + salts), and organics (e.g. paraffins and fatty acids) (Hasnain, 1998). Water boasts many of the desirable characteristics for a PCM, namely good thermophysical and chemical properties, economics, and durability, and it is by far the most widely investigated PCM for low temperature applications (Oro et al., 2012). A common use is for insulated packaging (Cryopak; Sofrigam), since compared to other materials, water has a relatively low freezing temperature that is suitable for food preservation and the transport of temperature-sensitive items (Oro et al., 2012). On a much larger scale, LHTES can be used for improved thermal management of building spaces. During the daytime, warm air is cooled by being circulated over the frozen PCM, and overnight, the heat from the now-melted PCM is removed through re-freezing. Energy consumption is decoupled from peak demand, which eases load on the grid, improves efficiency, reduces the carbon footprint, and saves costs (Dincer and Rosen, 2001). While this is a well-established concept, it has drawn renewed interest in recent years due to heightened priorities surrounding energy, environment and economics. After demonstrating their viability at both the theoretical level and pilot scale testing (Bedecarrats et al., 1996; Oro et al., 2012), water-based PCMs have found commercial success in companies such as Calmac, Evapco, IceEnergy and the Baltimore Aircoil Company. These technologies are slowly being integrated for space cooling in buildings such as the Kraft General Foods Headquarters (Illinois) and the San Francisco Marriot Hotel, as well as John Hopkins University, the University of Pennsylvania and Guangzhou University City in China (Evans, 1998; Dincer and Rosen, 2001). These organizations have all reported significant reductions in energy consumption, and of

course cost. This proven efficiency and reliability of water-based PCMs thus makes them a viable technology for cold energy storage. However, there exist two significant limitations that hinder the wide-scale use of water - and nearly every other PCM - for LHTES. These will be discussed in section 2.2.6.

The crystallization and melting of gas hydrate systems is another area of significant research interest involving the phase change of water. Gas hydrates are an allotropic crystalline structure of water that contain small gas molecules (methane, ethane, CO_2) within a caged structure. These compounds are also being considered as PCMs (PCM Products), but are particularly well-suited for natural gas transport, carbon dioxide capture and sequestration, and separation technologies due to very high gas storage capacities (Sloan, 2008).

Lastly, the intense convection observed in evaporating liquid droplets has spurred the development of several microfabrication technologies. These incorporate microfluidics for deposition of colloidal particles to engineer next-generation miniature devices and sensors through surface patterning (Squires and Quake, 2005; Dash et al., 2014; Prasad et al., 2014). While convection has been observed in the freezing and melting of water in various geometries, the droplet system, to the best of the author's knowledge, has not yet been explored.

2.2 Multiwall Carbon Nanotube Nanofluids

2.2.1 Carbon Nanotubes

The prefix “nano” is applied to materials with a least one dimension below 100 nm and commonly marks the realm where material properties can differ significantly compared to those observed at bulk scales. Carbon nanotubes (CNT) are nanometer-thick and micrometer-long cylindrical structures made from rolled sheets of graphitic carbon. Multiwall carbon nanotubes (MWCNT) were first discovered by Iijima in 1991, and singlewall nanotubes (SWCNT) were reported two years later by Iijima (1993) and Bethune et al. (1993). The past few decades have seen an explosive growth in the literature and patents devoted to CNTs at a rate of ~ 8% growth per year between 2000-2010 (Golnabi, 2012). Production volumes are steadily rising, costs are dropping (Evans, 2007), and market demand is booming, with multiwall carbon nanotubes commanding the overwhelming share of the CNT market (Transparency Market Research, 2016). Carbon nanotubes are touted as leaders amongst nanomaterials in a wide range of attributes, the most notable of which are mechanical, thermal, electronic, and optical properties. Current applications include electronics (e.g. quantum computing), energy (e.g. hydrogen fuel cells), mechanical (e.g. ultra-strong, lightweight composite materials), sensors, and drug delivery (De Volder et al., 2013). At only 25 years since their initial discovery, the pace at which the field of carbon nanotube science is progressing is remarkable. With the focus now shifting from discovery to technology, carbon nanotubes are likely entering a golden age of development, and marrying their capabilities with other disciplines will undoubtedly open up new and exciting applications (Jorio et al., 2008).

2.2.2 MWCNT Structure

Carbon can be found in several crystalline structures due to the numerous electronic states that it can assume. The three prevalent allotropes are diamond, graphite and the fullerene family. Diamond consists of a 3D tetrahedral matrix where each carbon is covalently bound to four other carbons in an sp^3 hybridization, and until recently, it was the hardest known material (Pan et al., 2009). Graphene consists of a one-atom thick, 2D planar sheet where each carbon atom is bound to three other carbons in an sp^2 hybridization. The remaining electron on each carbon is located to the p orbital, creating an aromatic hexagonal or honeycomb lattice where the electrons are delocalized. Graphite is assembled from the stacking of graphene sheets. The layers are spaced 0.335 nm apart and this distance is maintained by weak van der Waals forces between p orbitals (Iijima, 1991). This weak interaction allows the sheets to slide by each other, known as telescopic motion (Saito et al., 2001). Together, the strong hybridized binding of intralayer atoms and the π bonding between layers make graphite the most thermodynamically stable form of carbon at standard conditions (Wang et al., 2013).

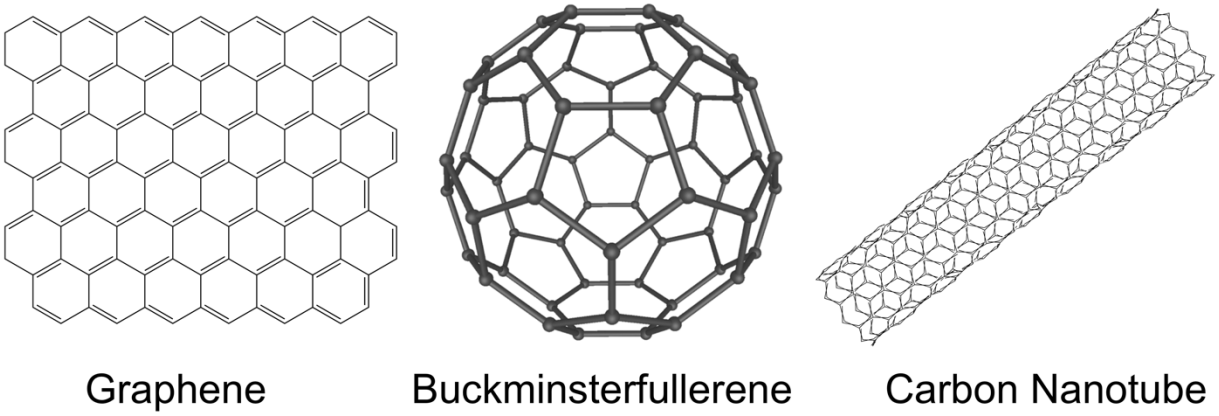

Figure 2.3: Allotropes of carbon.

Fullerenes are hollow geometries of carbon. The most popular structures are spheres, such as the C_{60} buckminsterfullerenes or 'buckyballs', and cylindrical carbon nanotubes. The formation of fullerenes can be imagined as the closing of planar graphene sheets in order to reduce the high energy of unsatisfied carbon atoms along the fringes (Dresselhaus et al., 2001). A small amount of strain energy is introduced though as a

result of surface bending. Carbon nanotubes consist of the rolling of graphene sheets into a seamless cylinder (Figure 2.3). The ends of the cylinders are often capped with a hemisphere for similar energy minimization reasons. SWCNTs typically have diameters around 1 nm. MWCNTs consist of two or more discrete concentric layers that can have diameters ranging from 2 to 100 nm (at which point they may not be considered "nano" any more) (De Volder et al., 2013). Both types are usually grown to micrometer lengths, although millimeter-long nanotubes have been created (Zheng et al., 2004). Accordingly, the aspect ratio (length/diameter) can vary substantially from two to seven orders of magnitude, and it is a unique feature of CNTs (Jorio et al., 2008). Similar to graphite, the interlayer spacing in MWCNTs is ~ 0.34 nm (or 3.4 Å), and the loose interlamellar coupling also permits telescopic motion within the MWCNTs (Dresselhaus et al., 2001). Finally, the manner by which the graphene sheet is "rolled" gives rise to a range of different configurations of the hexagonal patterns in the nanotube structure. The chiral angle refers to the alignment of such patterns with respect to the nanotube axis and it varies between 0° (zigzag structure) and 30° (armchair structure). This helicity plays a significant role in the properties of a CNT, such as whether it is metallic or semiconducting (Ajayan and Ebbesen, 1997).

2.2.3 MWCNT Synthesis and Functionalization

Carbon nanotubes can be fabricated by various methods, but the three prevalent techniques are arc discharge, laser ablation and chemical vapor deposition (CVD). The first two procedures make use of elevated temperatures to produce highly crystalline CNTs that are relatively defect-free. The major drawbacks of these methods are low production volumes and the need for purification of the CNT products from soot. The low-temperature CVD process allows for greater control over CNT features (length, number of walls, etc.). A consequence of this process is a reduction in crystallinity that gives rise to more structural defects, however these can be used as sites for chemical modification of the CNT surface. This provides the opportunity for tuning CNT properties, such as preventing agglomeration and making them dispersible in solvents

(Prasek et al., 2011). CVD has been the standard method for CNT production owing to good economics and production volumes, but new thermal plasma methods are becoming popular in industrial processes due to more favorable cost and production quantities. A thermal CVD preparation method was employed to fabricate the MWCNTs used in this study.

The general synthesis process is outlined in the experimental section of Chapters 3, 4, and 5. The complete details can be found in Baddour et al. (2009); Vandsburger et al. (2009); Hordy et al. (2013a) and references therein. Briefly, MWCNTs are grown on a catalytic stainless steel mesh substrate where the iron acts as the catalyst. A vapor mixture of Ar/C_2H_2 is flowed over the support catalyst in a furnace set to 700 °C. At these conditions, the hydrocarbon chemically decomposes with the help of the catalytic substrate and diffuses into the metal matrix. The high concentrations of carbon cause a eutectic transformation that enables MWCNT growth through a phase separation. MWCNTs then assemble vertically, and a tubular structure is preferred over other forms due to the minimization of energy in forming a closed structure (Dresselhaus et al., 2001). The length and diameter of the CNTs can be controlled by the amount of hydrocarbon injected (Hordy et al., 2013b). The resulting meshes consist of a forest of MWCNTs measuring on average 4 μm in length and 35 nm in diameter (Hordy et al., 2015).

As-produced MWCNTs are termed pristine (p-MWCNTs). They can be used as such or modified further if other functionalities are desired. In this thesis, MWCNTs are treated to covalently add various chemical groups to the outer surface. This requires breaking the strong sp^2 hybridization, which necessitates aggressive, high-energy techniques. Wet methods make use of strong acids (sulfuric, nitric) to oxidize the outer surfaces of p-MWCNTs (Hiura et al., 1995). These methods are relatively straightforward, but some drawbacks are that they may induce further defects, they require hazardous reagents, and they can have long processing times (Tseng et al., 2008). Another approach is through plasma treatment, which is the method that was used in this study. Processing non-equilibrium (cold) plasmas, such as the ones produced by capacitively coupled radio-frequency glow discharges, offer high-energy and reactive species required for

chemical insertion, but are less destructive to the MWCNTs owing to the low temperatures of reaction (Hordy, 2014). The plasma method is quick, simple and effective. Briefly, the mesh containing the p-MWCNT forest is transferred to a reactor where a mixture of $Ar/C_2H_6/O_2$ vapor is used to graft several types of oxygen functionalities onto the exterior surface, the most predominant being hydroxyl, carbonyl and carboxylic acid (OH, C=O, COOH) groups (Hordy et al., 2013a).

2.2.4 MWCNT Properties

CNTs constitute an extraordinary class of nanomaterials. They are arguably most renown for their incredible strength, as SWCNTs demonstrate some of the highest tensile strengths and Young's moduli of all materials discovered to date (Yakobson et al., 1996; Yu et al., 2000). Combined with a relatively low density, CNTs possess some of the highest strength-to-weight ratios, at 1-2 orders of magnitude greater than steel (Ajayan and Ebbesen, 1997). From a structural perspective, the valency of carbon allows for the formation of some very exotic structures. While chemically inert, CNT surfaces can act as scaffolding for the adsorption of polymers, biomolecules or other nanomaterials (De Volder et al., 2013). CNTs also exhibit outstanding electrical and thermal conductivities, even compared to metal nanomaterials such as copper and gold (Murshed and de Castro, 2014). Their electrical conductivity arises from the delocalization of electrons that allows for rapid and unimpeded transmission of current in the axial direction, known as ballistic conduction (Jorio et al., 2008). CNTs can be metallic or semiconducting based on their chirality and diameter.

Their remarkable thermal conductivity is due to the rigid structure that facilitates phonon transmission. Theoretical calculations for SWCNTs suggest that thermal conductivities on the order of 6600 W/m-K are possible, which surpasses that of diamond (Berber et al., 2000). Experimentally, much lower values have been observed, typically around 3000 W/m-K for SWCNTs (Kim et al., 2001) and 20-1000 W/m-K for MWCNTs (Choi et al., 2005; Xie et al., 2007). Note that both electrical and thermal conductivities apply only in the axial direction, as MWCNTs are radially insulating to

both effects due to the gap present between layers (Dresselhaus et al., 2001). The main reason why the measured properties fall short of theoretical predictions is due to the presence of structural imperfections, such as crystallographic defects, and geometric factors such as chirality, tube curvature, sample purity and agglomeration (Jorio et al., 2008). Furthermore, a drawback of surface functionalization is that the weaker sp^3 bonding created from chemical addition can reduce the mechanical, electrical and thermal properties of these layers (Shenogin et al., 2004). All these factors may also be a source of variation in the behavior of different batches of nanotubes produced from the same process. Nonetheless, the observed qualities are still exceptional and represent marked improvements over many current applications.

2.2.5 MWCNT Nanofluids

Choi and Eastman (1995) used a mathematical formulation to demonstrate that if nanomaterials were added to base fluids, their solid-state properties could bring about observable effects in the liquid systems. With this idea, they introduced a new avenue for the use of nanomaterials, and coined the term “nanofluid” to describe this application. Nanofluids consist of homogeneous suspensions of nanomaterials within a host liquid. Formally, these may also be categorized as colloids. The dispersions are upheld by the small sizes of the particles, as at these sizes, Brownian motion is sufficient to overcome settling forces due to gravity, and the particles may remain stably dispersed indefinitely (Taylor et al., 2013). The key to optimal nanofluid performance is to maintain particle separation, as their high aspect ratios make them prone to clustering in solution. This reduces the effective surface area to volume ratio, and more importantly, forms large masses that settle and no longer contribute to volume effects. The nature of the clustering interactions between particles can be classified into two mechanisms: reversible (agglomeration) and irreversible (aggregation), where the strength of the physical interaction is the differentiating feature (Sokolov et al., 2015). Experimentally, it is often difficult to distinguish between the two mechanisms owing to

challenges with characterization, however this distinction does serve to help categorize certain particle-particle interactions on a fundamental level.

Pristine carbon nanotubes are superhydrophobic in character (Vandsburger et al., 2009). In non-polar environments, p-MWCNTs can be stable, however in polar solvents such as water (used in this thesis), they will rapidly agglomerate and settle out of suspension. Chemical adjuvants – typically surfactants – are often added to the aqueous systems in order to aid in p-MWCNT dispersion. The nonpolar hydrocarbon chain adsorbs onto the p-MWCNT surface, leaving the water-soluble head group to interact with water (Vaisman et al., 2006). These amphiphilic molecules thus act as an interface friendly to both phases. The simplicity, versatility and cost-effectiveness of surfactant use make it a widely employed technique. Some of the drawbacks, however, are that the presence of additional chemical species increases the complexity of the system, possibly engendering unwanted secondary effects. Further, if the systems are brought to high temperatures, the stability of surfactants may be compromised (Hordy et al., 2014). This is where oxidized MWCNTs (f-MWCNTs) become advantageous. The acquisition of polar moieties by surface oxidation renders the f-MWCNTs intrinsically more compatible with water. There are two mechanisms that contribute to stability, depending on the type of functional groups. Oxygen groups that do not get ionized in solution, such as OH and C=O groups, form hydrogen bonding networks with water. The second and more significant contributor to f-MWCNT dispersibility in water is the carboxylic acid functionalities (Smith et al., 2009b). In water, at a pH below 6, deprotonation of the carboxylic acid creates a negative surface charge that helps to electrically stabilize the f-MWCNTs vis-à-vis the liquid and repel other particles due to similar electric charges. The formation of an electrostatic double layer is a common stability mechanism for colloidal suspensions (Derjaguin and Landau, 1941; Verwey and Overbeek, 1948). Unfortunately, these charged regions also invite impurities, and the stability of f-MWCNTs is highly sensitive to a multitude of parameters including pH, ionic strength, contaminants and dissolved organic content (Smith et al., 2009a).

Currently, the f-MWCNT nanofluids produced in-house have achieved year-long stability in water (Hordy et al., 2014). MWCNTs are excellent broadband absorbers of

light, especially in the visible range, as they appear black in solution, which is an excellent trait for direct absorption of solar energy (Hordy et al., 2014). The enhancements in heat transfer characteristics are probably the most investigated aspect of MWCNT nanofluids, and tremendous amounts of research energy are expended to precisely quantifying these properties. While MWCNT nanofluids have certainly shown augmented effective thermal conductivities compared to pure water, the extent and reproducibility of these effects is quite mixed (Murshed and de Castro, 2014; Xing et al., 2016). On the experimental side, the reported enhancements span a range of values, anywhere from minimal to 40%, although there is a general correlation between MWCNT loading and thermal conductivity increase (Jiang et al., 2015). Many of these values are influenced by the measurement techniques used, and the morphological characteristics of the MWCNTs may also play a role in these differences (Estellé et al., 2015). Recently, a broad study conducted by 30 research groups worldwide on identical nanofluid samples (of different nanofluid types) found good agreement between experimental values (~ 5%) and with mean-field theory predictions (based on Maxwell's model) (Maxwell, 1881; Buongiorno et al., 2009). Instances where experimental behaviours deviate significantly from classical theory are now mostly attributed to the inability to properly disperse the nanoparticles. The formation of clusters may significantly affect the observed enhancements by creating percolation networks. Despite these inconsistencies, MWCNT nanofluids remain prime candidates for improving heat transport in conventional process fluids, and many studies are now fine-tuning their methodologies to better elucidate the dominant parameters contributing to performance.

2.2.6 MWCNT Nanofluids in Liquid/Solid Phase Change

Most of the studies evaluating nanomaterials for phase change enhancement surround LHTES technologies. As discussed in Section 2.1.3, water is a most versatile and popular material. The main issue with water, and nearly all PCMs, is poor thermal conductivity. Water has the additional problem of long and unpredictable nucleation periods. Since

freezing and melting rates are central to the design of LHTES, it is ideal to maximize the thermal response of PCMs (Bugaje, 1997). Researchers have approached this task from many angles with methods including the placement of fins, metal matrix structures or brushes inside PCMs, and altering vessel material and geometry (Zalba et al., 2003). With the advent of nanotechnology, a new approach is the insertion of high conductivity particles within PCMs (Siegel, 1977). Materials such as CNTs can have thermal conductivities that are orders of magnitude greater than those of liquid water (0.6 W/m-K) and ice (2.3 W/m-K) (Perry and Green, 1997). Ideally, these are added at concentrations such that the heat capacity and equilibrium temperature are negligibly affected, usually below 1 wt%. The outstanding properties that MWCNTs offer have naturally sparked interest in their use as performance-enhancing additives to PCM systems.

Most of the work on MWCNT-enhanced PCMs has been conducted using p-MWCNTs in organic PCMs. Surprisingly, there are only a few studies to date that examine aqueous f-MWCNT systems. The presence of MWCNTs has been consistently reported to facilitate the nucleation of water by acting as foreign bodies for heterogeneous nucleation (Mo et al., 2011; Kumaresan et al., 2013; Jia et al., 2014). Since nucleation occurs at temperatures closer to the melting point, this increases the efficiency of LHTES. In terms of thermal response, MWCNTs have been shown to enhance the rate of sensible cooling, the rate of solidification, and even the total amount of water converted to ice (Mo et al., 2011; Kumaresan et al., 2013; Chandrasekaran et al., 2014; Jia et al., 2014). Our group investigates the impacts of MWCNTs on the crystallization of gas hydrate systems and found similar results on growth rate enhancement in methane, carbon dioxide and tetrahydrofuran hydrate systems (Pasieka et al., 2013a; Pasieka et al., 2013b; Pasieka et al., 2015). Park et al. (2010) and Kim et al. (2011) also noted increased conversion of liquid to gas hydrates with MWCNT addition. These results are consistent with those for MWCNTs in other PCMs. Collectively, these studies demonstrate the ability of MWCNTs to improve the efficiency of phase change processes.

The solidification of aqueous MWCNT nanofluids is the most studied facet of phase change enhancement. The melting process has garnered much less attention, especially

surrounding MWCNTs, owing to the relative novelty of the field. The presence of MWCNTs in other types of PCMs, or the presence of other types of nanomaterials (mostly metal oxides) in water, have shown either enhancing or inhibiting effects on melting (MacDevette and Myers, 2016). These effects are mostly dependent on whether the melting process is under a conductive or convective regime, which is mostly influenced by container geometry. In conductive regimes, nanomaterials typically expedite melting rates due to increased heat transfer. In systems that would normally see convection develop, nanomaterials often weaken convective forces through increases in viscosity and thermal conductivity (Phuoc et al., 2011; Zeng et al., 2013). This increases melting times, which is not ideal. On the other hand, Ding et al. (2006) reported enhancements in convective heat transfer of an aqueous CNT system in a horizontal cylinder (this system did not undergo phase change). Therefore it is important to characterize what type of mechanism will develop under a particular geometry to fully understand the effects of MWCNTs on both sides of the phase change process.

Finally, the stability of colloidal dispersions is by far the most critical aspect to the performance of nanofluids. It is essential that homogeneous dispersions exist for both liquid and solid systems so as to enhance the material properties of both phases, and that the nanofluids maintain uniformity across extended cycling. The issue of phase separation and particle clustering is regularly cited as a major challenge for these technologies, yet nanofluid stability is scarcely addressed in most studies, if mentioned at all. While the effects of nanomaterials on various properties of the PCMs are thoroughly described, there are little to no indications as to the quality of the dispersions during and after phase change. If comments are provided, visual descriptions of whether or not sedimentation has occurred are mostly used as a metric of stability. To be fair, the quantitative metrology of stability is difficult, and typically the contribution from several analytical techniques is required to obtain a meaningful assessment of stability (Yu and Xie, 2012; Sokolov et al., 2015). The lack of information surrounding phase change effects on MWCNT nanofluid stability signals that more work is required to fill this knowledge gap. MWCNTs have been reported to show good cycling performance in organic PCMs (again the metric for stability being whether or not visible

clusters were observed) (Wang 2008, Zeng 2008). Their resilience to the phase change of water has not yet been investigated. It follows that there is scarce data on critical velocities for MWCNT incorporation into solid PCM lattices. As discussed earlier, it is extremely difficult for modeling studies on phase change to predict for particle engulfment or rejection from solidifying materials (Fan and Khodadadi, 2012). Hence, specific studies on the dispersion of aqueous f-MWCNT nanofluids after extended phase change cycling, and a more quantitative evaluation of stability, will address this problem head-on in an attempt to better understand the relationship between phase change, nanofluids and colloidal stability.

Chapter 3

Behavior of Surface-Functionalized Multiwall Carbon Nanotube Nanofluids during Phase Change from Liquid Water to Solid Ice[1]

3.1 Preface

The enhancements that MWCNTs offer to the rate of cooling, nucleation and solidification of water systems have been well established in the literature. These experiments are usually conducted at a single temperature driving force, and seldom is there mention of the dispersion of MWCNTs in the final solid. This study focuses specifically on the solidification behavior of aqueous MWCNT nanofluids through visual characterization of their dispersibility over the course of and at the conclusion of the freezing process. A droplet geometry was chosen as it is an easy system to visualize and the basic principles governing nanofluid behavior during crystallization should extend to other geometries. These behaviours are surveyed over a range of temperature driving forces/freezing rates commonly used in the literature. Such morphological studies are essential to providing a more complete understanding of the freezing of nanofluid systems.

[1]Reproduced with permission from "Ivall, J., Hachem, M., Coulombe, S., Servio, P. Behavior of surface-functionalized multiwall carbon nanotube nanofluids during phase change from liquid water to solid ice. *Cryst. Growth Des.* 2015, 15 (8), 3969-3982." Copyright 2015 American Chemical Society. DOI: 10.1021/acs.cgd.5b00601

3.2 Abstract

Multiwall carbon nanotube (MWCNT) nanofluids have been shown to enhance the crystallization process of water to ice. While the beneficial effects of MWCNTs on phase change processes are well-documented, little work has been conducted to investigate the behavior of MWCNTs during and after exposure to freezing conditions. In this work, the crystallization morphology of water droplets containing surface-functionalized hydrophilic MWCNTs was evaluated at three driving force temperatures and two concentrations of nanofluid. At low supercoolings, the MWCNTs are completely expelled from the crystal matrix due to slow solidification rates. At high supercoolings, the MWCNTs are embedded in the solid droplet within air volumes and interdendritic regions as a result of rapid crystallization speeds. The results show that the dispersion of MWCNTs within the solid ice matrix itself was not achieved at these levels of supercooling. Under all conditions, freezing of the colloidal system results in destabilization of the MWCNTs and loss of dispersion. These effects are important considerations for applications requiring successful freeze/thaw cycling of nanofluid systems as well as in the storage and transport of colloidal suspensions.

3.3 Introduction

Nanofluids are stable suspensions of nanoparticles in a host fluid (Choi and Eastman, 1995). As the solid phase is homogeneously dispersed within the liquid phase, these biphasic systems can also be classified as colloids (Yu and Xie, 2012). The minute size of the particles enables Brownian agitation to prevail over gravitational forces, thus avoiding settling (Taylor et al., 2013). The presence of nanoparticles enhances or confers new properties to the host fluid. Among the most interesting features are augmented transport properties (heat and mass diffusivities), gas absorption, and electrical conductivity, as well as magnetic and tunable optical properties (Taylor et al., 2013). As a consequence, they are being investigated for an increasingly wide array of applications.

Multiwall carbon nanotubes (MWCNT) are a particular class of inorganic particles that consist of layered graphitic sheets rolled into a cylindrical structure (Tasis et al., 2006). In themselves, these materials offer superior mechanical strength and chemical resistance, and the abundance of source material (carbon) facilitates many aspects of their production (Das et al., 2007). When dispersed in a host fluid, MWCNTs enhance the transport coefficients and add broadband absorption properties (UV-Vis down to GHz and MHz). The performance of nanofluids is contingent on maintaining separation between particles in solution, and the main challenge with MWCNT-based nanofluids is that their carbon content gives them a hydrophobic character. Therefore, techniques are required to ensure individual particle dispersion in polar solvents in order to overcome attractive van der Waals forces. Stable suspensions can be achieved through a variety of approaches, the most common of which are the addition of chemical agents to MWCNT-containing systems or direct chemical modification of the outer surface of the MWCNTs (Yu and Xie, 2012). The mixing of surfactant molecules is ideal for economic and practical reasons; however the robustness of the additives themselves is not always sufficient, and their presence might alter the desired properties of the system. Functionalization of MWCNT surfaces can be achieved through wet or dry approaches, whereby fixation of polar groups (e.g., OH, CO, COOH, NH, NH_2) to the exterior wall renders the nanotubes hydrophilic. These moieties promote contact with water to assist dispersion throughout the base fluid (Vandsburger et al., 2009; Hordy et al., 2013a; Jorge et al., 2015). In the case of oxygenated MWCNTs, dispersion into a polar solvent causes deprotonation of the oxygen groups that leads to the creation of an electrical double layer around each particle (Taylor et al., 2013). Repulsive electrostatic (Coulombic) forces between similarly charged particles then uphold MWCNT dispersion, as outlined by DLVO theory (Missana and Adell, 2000). While these functionalization methods are perhaps more costly and technically involved, the two-component composition of the system and the robustness of the MWCNTs allows for a reliable, explicit evaluation of the nanomaterials' effects (Taylor et al., 2013). Recent advances in MWCNT synthesis and stabilization techniques have permitted functionalization of the surface through plasma treatment (Vandsburger et al., 2009). This technique is simple, requires less chemical reactants, which reduces cost and waste, and produces consistent, homogeneous nanofluids that are stable over extended periods

of time and at temperatures significantly higher than the limit for surfactants (~60 °C) (Hordy et al., 2014).

Nanofluids made containing MWCNTs (as well as other types of nanoparticles) were originally recognized for their improved conductive and convective heat transfer properties (Yu and Xie, 2012). Recently, their ability to absorb electromagnetic energy over a broad spectrum, to enhance mass transfer, to selectively absorb gaseous species, and to affect the heat capacity of the host material have been highlighted, thus opening the door to a panoply of applications, particularly energy capture and transmission technologies (Taylor et al., 2013). These advantageous effects have also begun to be evaluated for phase change enhancement of the base fluids, most commonly for liquid-to-solid transitions. Some examples of applications that are currently exploring this avenue are cool thermal energy storage (CTES), cryopreservation, and gas hydrate formation (Kumaresan et al., 2013; Pasieka et al., 2013a; Pasieka et al., 2013b; Taylor et al., 2013; Chandrasekaran et al., 2014). The study of phase change phenomena is fundamental, and analyses pertaining specifically to the behavior of colloidal systems have implications for these emerging multidisciplinary technologies. As foreign bodies, MWCNTs have been shown to facilitate nucleation in liquid-to-solid (freezing) systems (Jia et al., 2014). Since less driving force or energy is required to form the new phase, MWCNTs increase the efficiency of phase change processes. Furthermore, MWCNT nanofluids have been shown to enhance the rate of sensible cooling, the rate of solidification, and the total amount of liquid-to-solid conversion (Wang et al., 2008; Mo et al., 2011; Kumaresan et al., 2012; Kumaresan et al., 2013; Chandrasekaran et al., 2014). However, while the technical benefits of MWCNT addition to solidifying systems have been clearly established, few studies have examined the characteristics of the MWCNTs during and after freezing processes. Since the stability of nanofluids is vital to their overall performance, the impact of crystallization on MWCNTs provides a more holistic understanding regarding the feasibility of implementing colloidal technologies. In this work, the solidification behavior of static droplets made of aqueous suspensions of surface-functionalized MWCNTs is investigated through a morphological analysis. Water is chosen as the base medium, as it is one of the most common fluids for suspension and the study of its crystallization has many natural, industrial and practical

applications. The effect of two MWCNT concentrations and three driving force temperatures is assessed, and the visual characteristics of the nanofluid after melting are reported.

3.4 Experimental Method

3.4.1 MWCNT Nanofluid Synthesis

MWCNTs are grown on stainless steel (SS) meshes by thermal chemical vapor deposition (t-CVD) using acetylene as the carbon source. The as-produced MWCNTs are hydrophobic, and a subsequent process of surface functionalization using a capacitively coupled radio frequency glow discharge with an $Ar/C_2H_6/O_2$ gas mixture adds covalently bound oxygen moieties, such as hydroxyl, carbonyl, and carboxyl groups, to the exterior surface. This treatment yields polar MWCNTs that are superhydrophilic in character. The MWCNT-covered SS meshes are then placed in water treated by reverse osmosis (RO, 0.22 μm filter, conductivity of 10 μS, total organic content < 10 ppb), and the MWCNTs are broken off (no metal catalyst is transferred to the host fluid) from the mesh through ultrasonication to yield homogeneous and stable nanofluids. The removed MWCNTs have an average diameter of 31.4 nm and length of 1 μm. Further information regarding the synthesis and characterization of the MWCNTs used in this study can be found in Baddour et al. (2009), Vandsburger et al. (2009), Hordy et al. (2013a) and references therein.

3.4.2 Freezing of Aqueous MWCNT Suspensions and Visual Characterization

Figure 3.1 provides a schematic of the experimental setup. The temperature of the thermoelectric (TE) cold plate (TE Technology, Inc.) is set to -5, -10 or -20 °C. The TE cooler module consists of a Peltier cold plate (CP-200TT) connected to a temperature controller (TC-36-25) and a power supply. The temperature of the cold plate is

monitored by a general-purpose thermistor (MP-3193) with an operating range of -20 to 100 °C and a sensor tolerance of ±1.0 °C between 0 and 70 °C and +1.4/-2.2 °C at -20 °C. The controller parameters are set and recorded through the use of a National Instruments LabVIEW VI. Once the cold plate reaches the target temperature, 10 μL droplets of either pure RO water, 20 or 100 ppm MWCNT nanofluid are deposited onto a layer of poly(tetrafluoroethylene) (PTFE) tape (TaegaSeal, Mil-T-277730A, 0.064-0.089 mm thickness) that is set on top of a 1 mm thick copper plate. The sample plate is then transferred to the cold surface, and image capture is initiated. Images of the solidification process are taken with a Canon EOS 60D DSLR camera (18.0 Megapixel CMOS sensor) equipped with a Canon MP-E 65 mm f/2.8 1-5x macro lens. The camera is mounted onto an OptoSigma multiaxis manual positioner stage for fine-tuning of the focal point. The camera is angled approximately parallel to the cold plate surface and normal to the droplet. A Schott KL 2500 fiber optic LED light source illuminates the droplet from above, and a white reflective screen is fixed vertically to the copper plate behind the sample to improve brightness. The entire setup is mounted onto a Newport RS 3000 optical table to minimize vibrations. For morphological experiments, nucleation is detected visually by the appearance of a solid front at the bottom of the droplet and, in some cases, by the formation of dendritic ice. To obtain the temperature at nucleation (T_N), a 0.25 mm fine diameter thermocouple probe (Omega) with an operating range of -210 to 2100 °C and an accuracy of ± 1.1 °C is inserted into the liquid. The thermocouple is placed at the center of the base of the droplet, where the supercooling is greatest. For these thermocouple experiments, nucleation is marked by a sharp temperature increase, as crystal growth is an exothermic process. The time elapsed for nucleation to occur (t_N) from when the sample plate is placed on the cold surface is noted, and the duration of the freezing process is determined from the time stamps of the images. The average velocity of the solidification front is then calculated by dividing the height of the solidified droplet by the total time required for crystallization. After the droplet has completely frozen, the sample plate is moved to a Styrofoam surface and the system is left to melt at room temperature. Once the droplet has fully thawed, an image is taken. The liquid is then wiped off of the PTFE surface and the sample plate is rinsed and dried for a subsequent experiment.

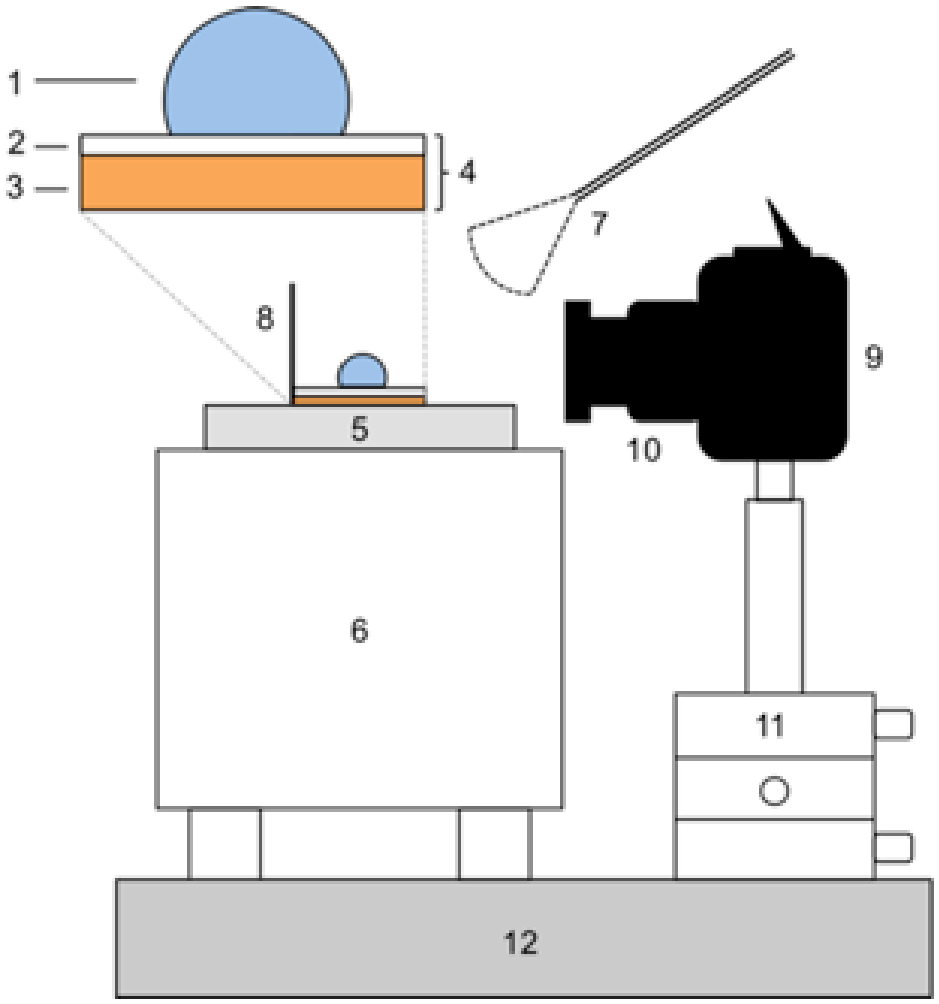

Figure 3.1. Schematic of the experimental apparatus. (1) Droplet, (2) PTFE strip, (3) copper plate, (4) sample plate, (5) TE cold plate surface, (6) TE cold plate body, (7) light source, (8) reflective surface, (9) camera, (10) lens, (11) *x,y,z* multiaxis manual positioner, and (12) optical table. Objects are not drawn to scale.

3.5 Results and Discussion

3.5.1 Effect of Driving Force on Crystallization Velocity and Correlation to Nucleation Temperature

The freezing behavior of water droplets containing two concentrations of surface-functionalized MWCNTs was analyzed at three cold plate setting temperatures. Pure water droplets were also frozen to evaluate the crystallization process in the absence of the colloidal phase. These conditions were chosen in order to assess the crystallization behavior of nanofluids over a range of driving forces. The driving force (DF) or degree of supercooling (DS) is defined as

$$\mathrm{DF} = T_{EQM} - T_N \qquad \text{Eq. 3.1}$$

where T_{EQM} corresponds to the two-phase (liquid/solid) equilibrium temperature of 0 °C (at atmospheric pressure) and T_N corresponds to the droplet temperature at nucleation. At these low concentrations, it is assumed that the presence of MWCNTs has a negligible effect on the equilibrium properties of the system (Mo et al., 2011; Kumaresan et al., 2012; Chandrasekaran et al., 2014). Throughout this article, the expression “a greater supercooling” refers to an increase in driving force and hence colder experimental temperatures.

The sessile droplets are frozen to completion based on visual inspection. The phase change process of water to ice is a heat transport problem that can be divided into three discrete kinetic stages (Glicksman et al., 1994). The first step consists of an initial fast growth of a small expanse of crystal (typically dendrites) into the bulk liquid immediately following nucleation, the extent of which is more drastic at greater supercoolings. This event occurs on the order of seconds, and the recalescence of the surrounding fluid due to the large amount of heat released from the crystallization process makes growth self-limiting (Pruppacher, 1967a; King and Fletcher, 1973; Feuillebois et al., 1995). The second step involves the conversion of the remaining bulk

liquid into solid, which takes place over the course of minutes. This solidification process is governed by conduction, as the latent heat of crystallization must be transferred from the liquid at the interface to the surrounding medium (Pruppacher, 1967a; Feuillebois et al., 1995). The final step comprises solid-state adjustments within the crystal matrix to correct imperfections, a process that proceeds over hours to days (Pruppacher, 1967b; Glicksman et al., 1994; Mullin, 2001).

For the -5 °C setting, the nucleation event was generally discerned by the gradual rise of a smooth, planar boundary from the base of the droplet (Figures 3.4b, 3.5b, and 3.6b) due to minimal dendrite formation. For the -10 and -20 °C experiments, nucleation was marked by the rapid spread of dendritic branches from the base of the droplet throughout the bulk liquid (Figures 3.7b, 3.8b, 3.9b, 3.10b, 3.11b, and 3.12b). This freeze was accompanied by exothermic heat release where the system temperature rises to equilibrium (this process was observed for all thermocouple experiments but is not shown). Final conversion of the partially frozen mixture of water and ice was then completed by the ascending crystallization front. For all experimental conditions, the formation of either a distinct pointy tip or a crater of MWCNTs at the top of the droplet signaled the end of the freezing process. The cusp phenomenon is well-documented in the literature and is attributed to the expansion of water during solidification (Sanz et al., 1987; Walford et al., 1991; Anderson et al., 1996). In this study, the duration of the solidification process includes the first two stages of crystallization. The solid-state adjustments are not considered but are expected to occur over longer time scales.

In the context of this study, the use of the term “dendrites” connotes the initial, limited amount of crystal formed rapidly (< 1 s) upon nucleation as the first part of a two-stage growth process (Figure 3.2). These structures seemingly formed as a thin hemisphere of ice along the external water-air interface (at the -10 °C and -20 °C temperature settings, and not at -5 °C). It should be noted that the term “dendrite” typically denotes the morphology of the solid interface during crystallization, in this case, the slower (tens to hundreds of seconds) ascending freezing front that comprised the general conversion of the remaining bulk liquid to solid. Dendritic growth occurs when the heat of crystallization is removed by the liquid. Situations where the heat is removed through

the solid phase (ice) yield planar interface structures. A schematic of the temperature profiles across the system and the corresponding growth mechanism is provided in Appendix A as Figure A1. Both planar and dendritic growth profiles apply to a unidirectional solidification process, such as the one observed in these experiments. This study does not attempt to characterize which type of growth mechanism is occurring at the interface during the second stage of the two-step growth process. It is also not clear if this rapid initial structure itself is effectively showing dendritic growth or a fine planar growth from a very large number of initial nuclei. However, the heat removal geometry in the present system likely favors a planar structure at all conditions tested, and not a dendritic morphology. Microstructural analyses would be required to confirm the type of growth in both stages, these are however beyond the scope of this study.

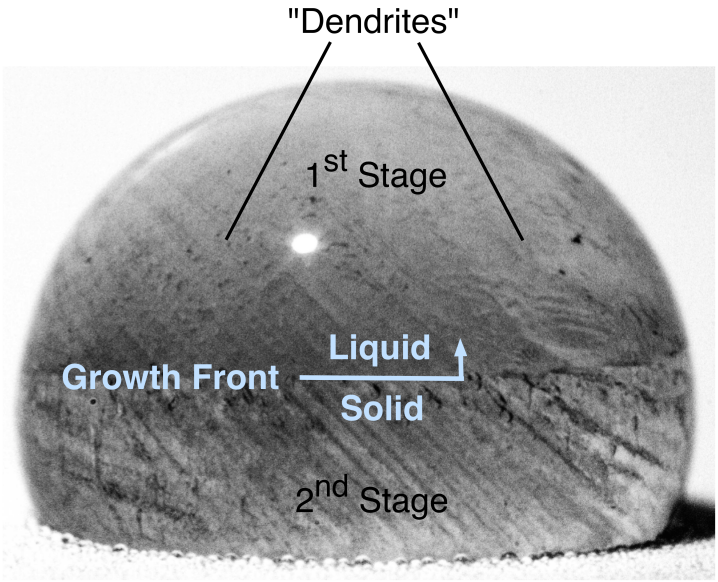

Figure 3.2: Meaning of the term “dendrite” in this study.

At each cold plate setting, the time required for nucleation (t_N), the velocity of the crystallization front (v_F), the droplet temperature at nucleation (T_N), and the crystal morphology throughout the solidification process were examined. In order to relate the morphology of the freezing systems to the level of supercooling, a careful characterization of the droplet temperature at nucleation is necessary. Unfortunately,

these analyses must be decoupled, as insertion of the thermocouple during image capture affects droplet morphology. These properties can be reconnected, however, through the speed of crystallization, as all three phenomena are closely linked (Carte, 1961). A separate set of experiments was thus conducted to specifically correlate crystallization velocity to nucleation temperature. This relationship was then used to back-calculate T_N for the morphological experiments by inputting the measured v_F. For the purpose of comparison, these speeds are calculated as an average over the height of the droplet. The calculation does not take into account the acceleration and deceleration of the phase boundary as a result of changes in height and surface area of the interface for heat transfer (Chaudhary and Li, 2014). The data set acquired through the thermocouple experiments for velocity as a function of the degree of supercooling is presented in Figure 3.3. Experiments were performed with a minimum number of 10 replicates for each temperature-concentration combination, for a total of 101 data points. Figure 3.3 shows that the speed of crystallization increases with the degree of supercooling. This trend is consistent with the literature on crystallization processes, which states that the greater the departure from equilibrium, the faster the rate of solidification, due to enhanced heat transfer (Walton and Judd, 1913; Hillig and Turnbull, 1956; Hallett, 1964; Pruppacher, 1967a). At a given supercooling, no discernible difference was observed among the three MWCNT concentrations (0, 20, and 100 ppm). Consequently, the results of the three conditions are shown in the same color (gray) in Figure 3.3. An in-depth analysis of whether MWCNT concentration statistically has an effect on nucleation temperature and crystallization speed would require a significantly larger data set and is beyond the scope of the current study (Heneghan et al., 2001). The relationship between temperature and crystallization velocity has been previously described using a modified Noyes and Whitney growth mechanism (Cahn et al., 1964; Edie et al., 1983; Pasieka et al., 2014). For a heat transfer-limited process, the model expresses velocity as an exponential function of the degree of supercooling, as shown in Equation 3.3.

$$V = A(T_{EQM} - T_N)^B = A(\mathrm{DF})^B \qquad \text{Eq. 3.2}$$

where V is the velocity of the solid front (in μm/s), and A (μm/s°C^B) and B (dimensionless) are fitted parameters. The curve for the model is shown in solid black in Figure 3.3, and the corresponding empirical constants are listed in Table 3.1 with their 95% confidence intervals. For the data set acquired, these values were determined to be A = 4.71 μm/s°C^B and B = 1.08. Note that these values are unique to this system. A 95% confidence region was also calculated on the model and is represented by the dashed lines on either side of the trendline. Most of the experimental data lie well within these limits. The small amount of scatter is common to any crystallization process and is largely attributed to the influence of uncontrollable crystallographic factors such as imperfections, grain boundaries, trapped particles, and so forth (Mullin, 2001). It can also be seen that the spread of the data increases with the degree of supercooling and that the temperatures at nucleation are higher than the cold plate setting. Nucleation is an intrinsically stochastic event, although the probability of its occurrence is related to the departure of the system from equilibrium (Mullin, 2001). At low driving forces, the small impetus for crystallization allows the system to reach the steady-state temperature, which is slightly warmer than the cold plate set point due to exposure to ambient air. At high driving forces, the increased probability of nucleation makes crystal formation more likely to occur over a range of supercooling levels and most often before the droplet attains the coldest temperature possible.

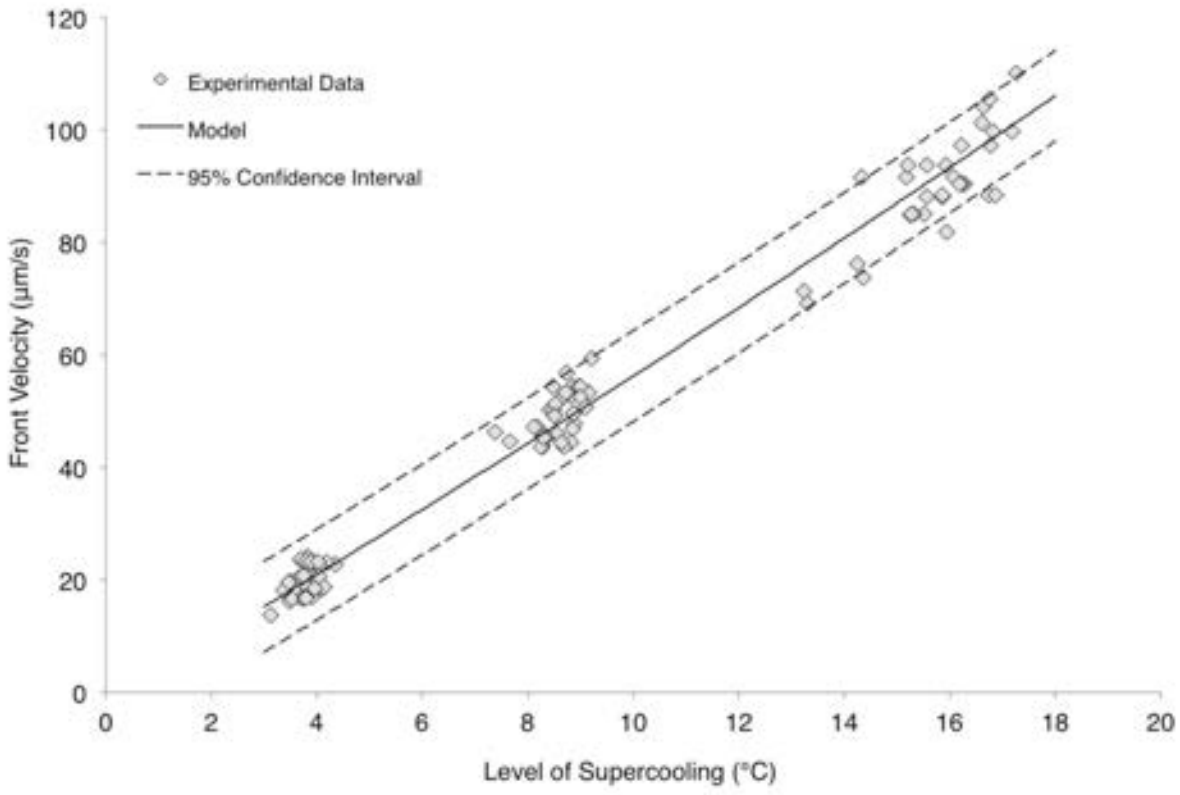

Figure 3.3. Correlation of front velocity to droplet temperature at nucleation.

Table 3.1. Empirical constants for crystallization velocity as a function of supercooling[a], with 95% confidence intervals.

parameter	value	95% CI
A (μm/s°C^B)	4.71	1.07
B (dimensionless)	1.08	0.03
[a]See Eq. 3.2		

The nucleation temperatures (T_N) for each experimental temperature-MWCNT concentration combination were calculated from the correlation in Figure 3.3 and are presented in Table 3.2. Once again, the data show that the velocity of crystallization increases with increasing driving force. This dependence for freezing water systems has been described extensively in the past (Walton and Judd, 1913; Hillig and Turnbull, 1956; Lindenmeyer et al., 1957; Pruppacher, 1967a). For the -5 °C setting, the droplets typically froze in the range of 7 to 10 min, yielding nucleation temperatures between -

1.27 and -2.32 °C. The -10 °C setting experienced crystallization times of approximately 1 to 2 min, with nucleation temperatures between -3.33 and -7.42 °C. Finally, the -20 °C setting saw freezing on the order of 40 s, giving nucleation temperatures between -10.3 and -10.9 °C. Note that the solidification speeds of the morphological experiments were much slower than those from the thermocouple experiments. Consequently, the nucleation temperatures extrapolated for the morphological experiments are higher (warmer) than those from the temperature data set. This is possibly due to a combined effect of lighting, stochasticity, and ambient conditions. The power and position of the light source were fine-tuned on an experiment-by-experiment basis, and an increased proximity to the samples could lead to a small increase in temperature, thus reducing speed. Regardless of the cause, this possible shift in temperature elicits a corresponding morphological behavior from the droplet due to the strong correlation between nucleation temperature, front speed, and droplet morphology established above.

Table 3.2. Temperatures at nucleation (T_N) calculated from crystallization velocities of droplets at three driving force temperatures for morphological experiments

	-5 °C setting		-10 °C setting		-20 °C setting	
	Velocity (μm/s)	T_N (°C)	Velocity (μm/s)	T_N (°C)	Velocity (μm/s)	T_N (°C)
Water	11.7	-2.32	40.8	-7.42	60.3	-10.7
20 ppm MWCNT	6.78	-1.40	36.3	-6.65	61.7	-10.9
100 ppm MWCNT	6.08	-1.27	17.2	-3.33	58.2	-10.3

3.5.2 Effect of Driving Force on MWCNT Dispersion in the Crystal Phase

The effect of temperature on droplet morphology during crystallization was evaluated at three driving forces and three MWCNT concentrations (0, 20, and 100 ppm). The results are presented in terms of the cold plate setting, as the supercooling temperature at nucleation varies for each droplet (Table 3.2). The morphologies of droplets at the -5

°C setting are shown in Figures 3.4-3.6, those for the -10 °C setting are shown in Figures 3.7-3.9, and those for the -20 °C case are shown in Figures 3.10-3.12. In all image sequences, image (a) presents the liquid droplets prior to freezing, along with the time required for nucleation (t_N) and the droplet temperature at nucleation (T_N) correlated from the data in Figure 3.3; image (b) illustrates the droplets shortly after nucleation; images (c-e) track the progression of droplet solidification; and image (f) shows the droplet at the completion of freezing. The time elapsed since nucleation is indicated in the upper left-hand corner of images (b-f). Each condition was repeated at least 10 times in order to ensure the reproducibility of the results in terms of the morphological behaviors observed.

As evidenced by Figures 3.4-3.12, the tendency of MWCNTs to be incorporated into the ice matrix was a strong function of temperature. Prior to nucleation, the droplets containing MWCNTs exhibit a uniform darkness, the opacity of which is relative to their concentration. This homogeneity is characteristic of a well-dispersed, stable nanofluid. The presence of a few small clusters is typical of any suspension. The pure water droplets are transparent, although the top portion may appear to be a cloudy white as a result of the lighting from above and the reflective PTFE surface beneath. Under all conditions, the formation of ice reduces the transparency of the droplet. At the -5 °C setting, the ice appears quite clear, exhibiting very few imperfections (at this magnification). In systems containing MWCNTs (Figures 3.5 and 3.6), the appearance of black clumps and filaments along the liquid/solid interface (Figures 3.5d and 3.6d) suggests clustering of the nanotubes along the solid surface. The sizes of these bundles range from tens to hundreds of micrometers (Figure 3.13a). From the onset of crystallization, the MWCNTs are continuously driven into the liquid phase and carried by the solid front until eventually forming a large crater at the top of the droplet (Figures 3.5f and 3.6f). The crystal beneath is virtually free of MWCNTs owing to its remarkable clarity. It is thus clear that at very low driving forces and crystallization speeds the MWCNTs are completely expelled from the developing crystal.

At the -10 °C setting, the morphology of the solidifying nanofluids changes significantly. The two stages of crystallization become more distinguishable as nucleation triggers

dendrite formation (Figures 3.7b and 3.8b), which is then followed by the slower ascending front. Dendrite growth was relatively horizontal with curved branches. The entrapment of air pockets within the crystal is also observed (Figure 3.7e). The bubbles are relatively dispersed with large volumes (approximately 30 μm) and elliptical shapes. Bubble formation during freezing is a result of the solubility of air in ice being approximately 3 orders of magnitude less than in liquid water (Scholander et al., 1953). In this case, a peculiar zoning pattern occurs where the base of the droplet encloses a high number of bubbles, above which a zone of clear ice ensues, with the reappearance of air volumes in the upper section (Figures 3.7f, 3.8f, 3.9f). In static systems such as sessile droplets, the speed of crystallization is the largest determinant in the extent and morphology of the trapped volumes of air (Carte, 1961). The rejection of dissolved air from the solid into the liquid phase increases the local concentration of air at the moving interface, and if supersaturation is reached, air molecules nucleate into a separate phase, creating pockets (Carte, 1961). At low degrees of supercooling, such as the -5 °C case, slower growth rates allow diffusion and possibly buoyancy of the nucleated air bubbles away from the interface and into the bulk liquid, whereas the faster velocities at higher degrees of supercooling overcome diffusion and lead to entrapment. Therefore, this wave-like or oscillating phenomenon of bubble formation arises in a unique ratio of ice growth rate and air precipitation, similar to reaction-diffusion patterning (Carte, 1961). An explanation of this eutectic transformation is offered in Appendix A. MWCNT inclusion into the solid droplet also begins to take place at these moderate degrees of supercooling. Figures 3.8 and 3.9 show that while the MWCNTs are encapsulated to some degree in the ice, it is predominantly in the form of clusters on the order of tens of micrometers in size. Furthermore, the MWCNTs are grouped within bubble volumes and not within the ice matrix itself, which is best visualized in Figure 3.8d. This indicates that at these solidification speeds, individual particle dispersion is not achieved in the solid. Since the localization of the MWCNTs is similar to that of the bubbles, it follows that the speed of crystallization is not constant across all heights of the droplet. The lower and upper portions freeze quickly due to relatively higher heat transfer, engulfing MWCNTs and air, whereas the deceleration of the interface in the middle section allows for migration of air and MWCNT molecules within the liquid. Furthermore, while air molecules can diffuse into the atmosphere outside of the droplet,

solid particles, such as MWCNTs, are confined to the droplet's surface. The extent of particle rejection was more severe in the 100 ppm case (Figure 3.9), which may be due to the slower velocity and thus to the lower degree of supercooling compared to that for the 20 ppm loading (Figure 3.8).

The highest driving force setting of -20 °C gave rise to the most extensive degree of dendrite formation and bubble entrapment as well as MWCNT inclusion within the solid matrix. The dendrites extend further throughout the droplet with sharper, finer branching (tens of micrometers) and more vertical orientations (Figures 3.10b, 3.11b, and 3.12b) (Hallett, 1964). Bubbles were also smaller in size, less than tens of micrometers, and distributed evenly throughout the droplet. Across all driving forces and MWCNT concentrations examined, the presence of nanotubes was not observed to have an effect on the surface morphology of the ice matrix itself. At these cold temperatures, for both concentrations, most of the MWCNTs were confined within the solid droplet. Similar to the -10 °C driving force, Figures 3.11 and 3.12 show that the nanotubes are embedded in clusters, and the localization of the clumped masses follows the bubble and dendrite patterning (Figure 3.13c). An important distinction between the mechanism of nanotube clustering and bubble formation is that, as a colloidal suspension, the nanotubes do not nucleate into a distinct phase due to supersaturation, as they are not dissolved in the liquid phase like air; rather, they are stably dispersed. Their grouping together is a consequence of their exclusion from the solid water phase. While the clusters are distributed uniformly within the droplet, their formation indicates that dispersion within the solid crystal is still not achieved at these high crystallization speeds.

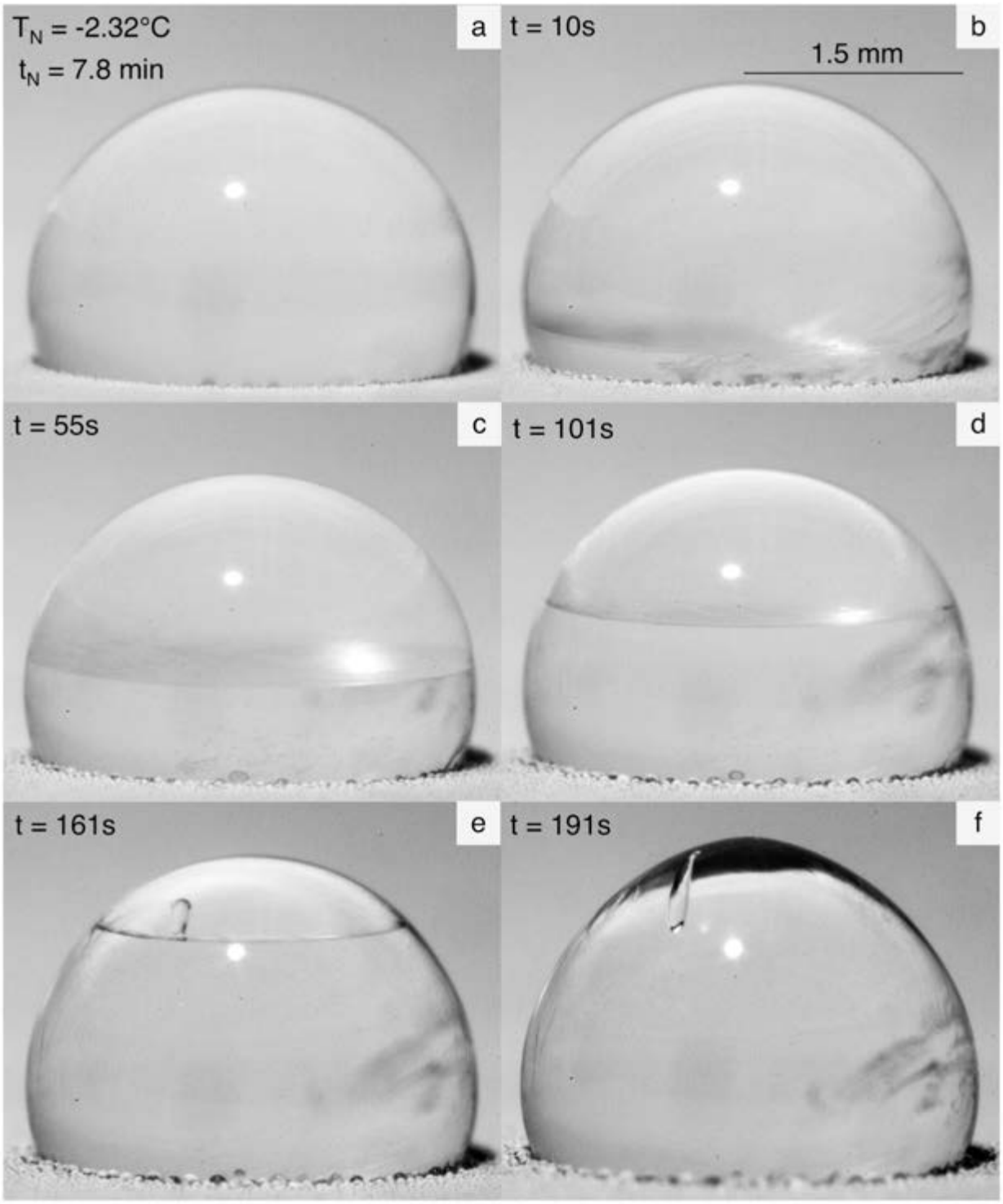

Figure 3.4. Crystallization of a pure water droplet at a cold plate setting of -5 °C.

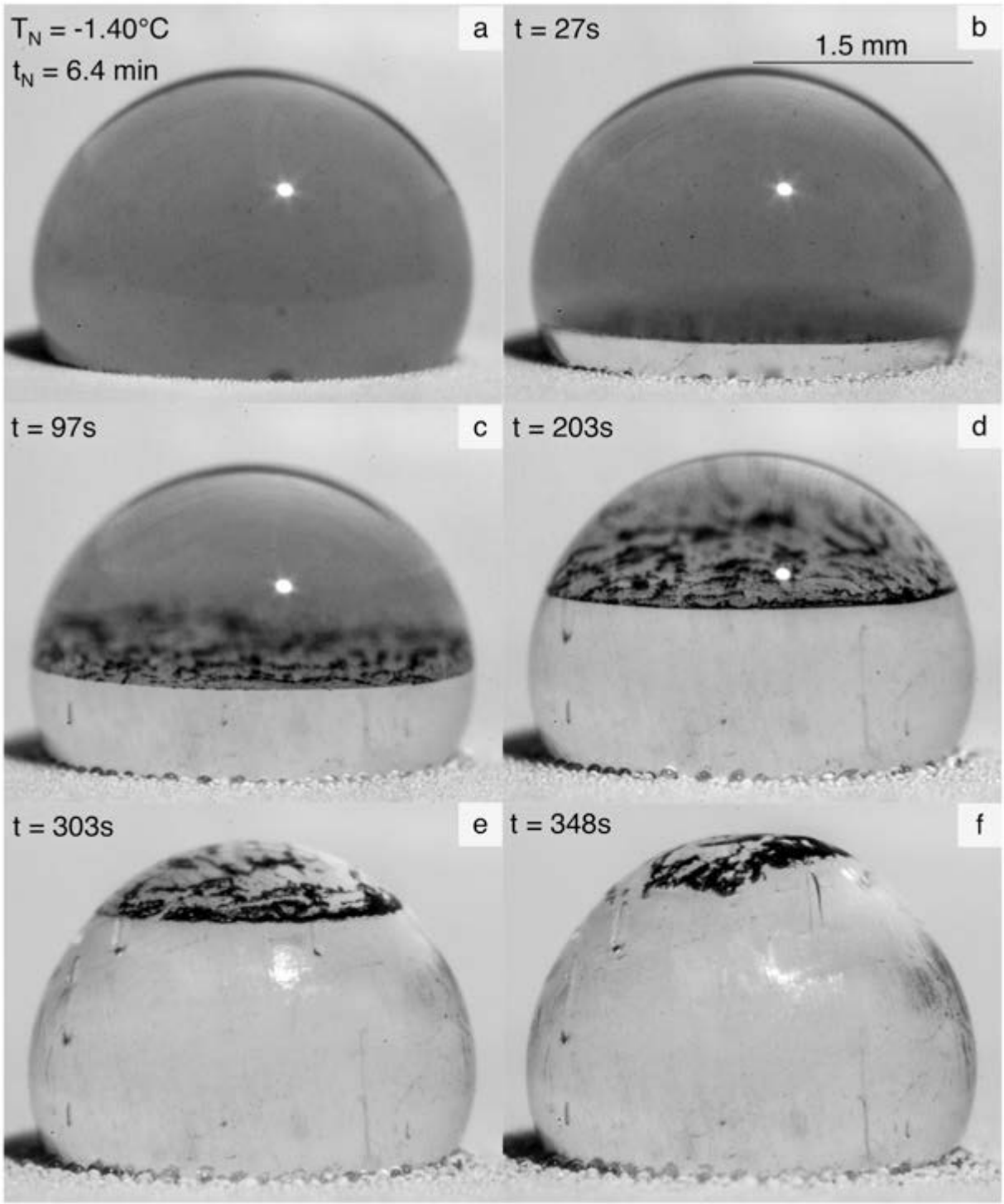

Figure 3.5. Crystallization of a 20 ppm MWCNT-water nanofluid droplet at a cold plate setting of -5 °C.

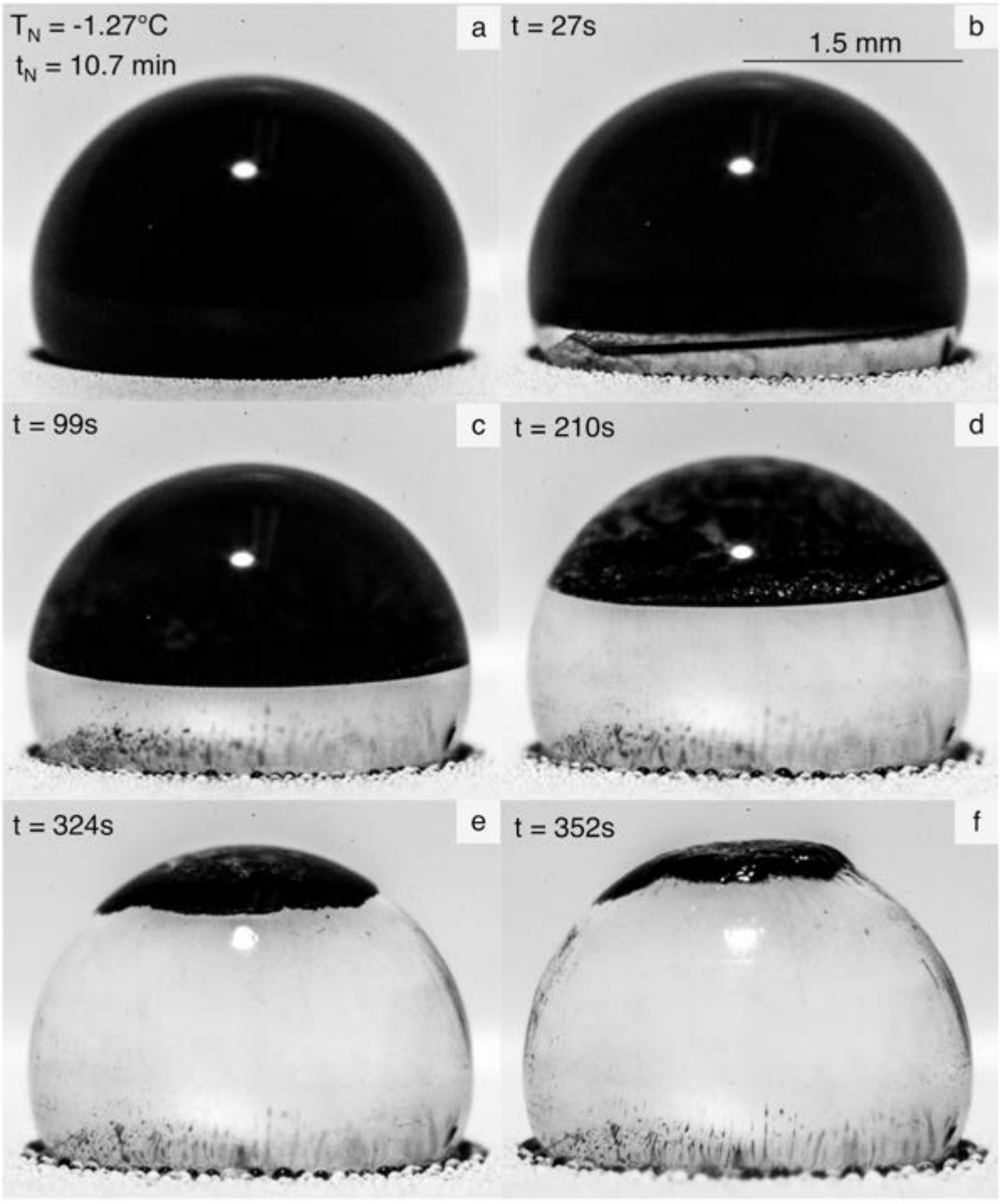

Figure 3.6. Crystallization of a 100 ppm MWCNT-water nanofluid droplet at a cold plate setting of -5 °C.

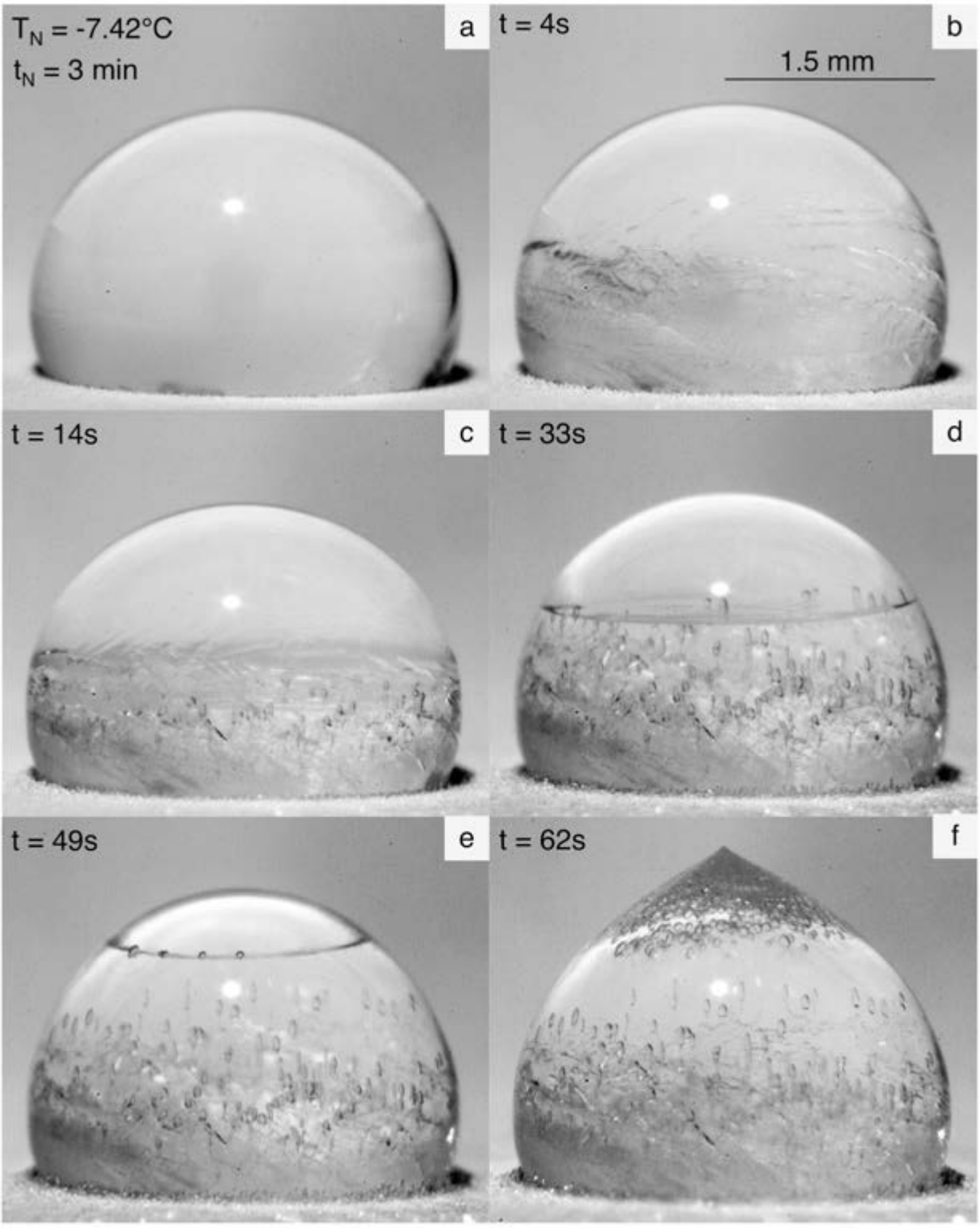

Figure 3.7. Crystallization of a pure water droplet at a cold plate setting of -10 °C.

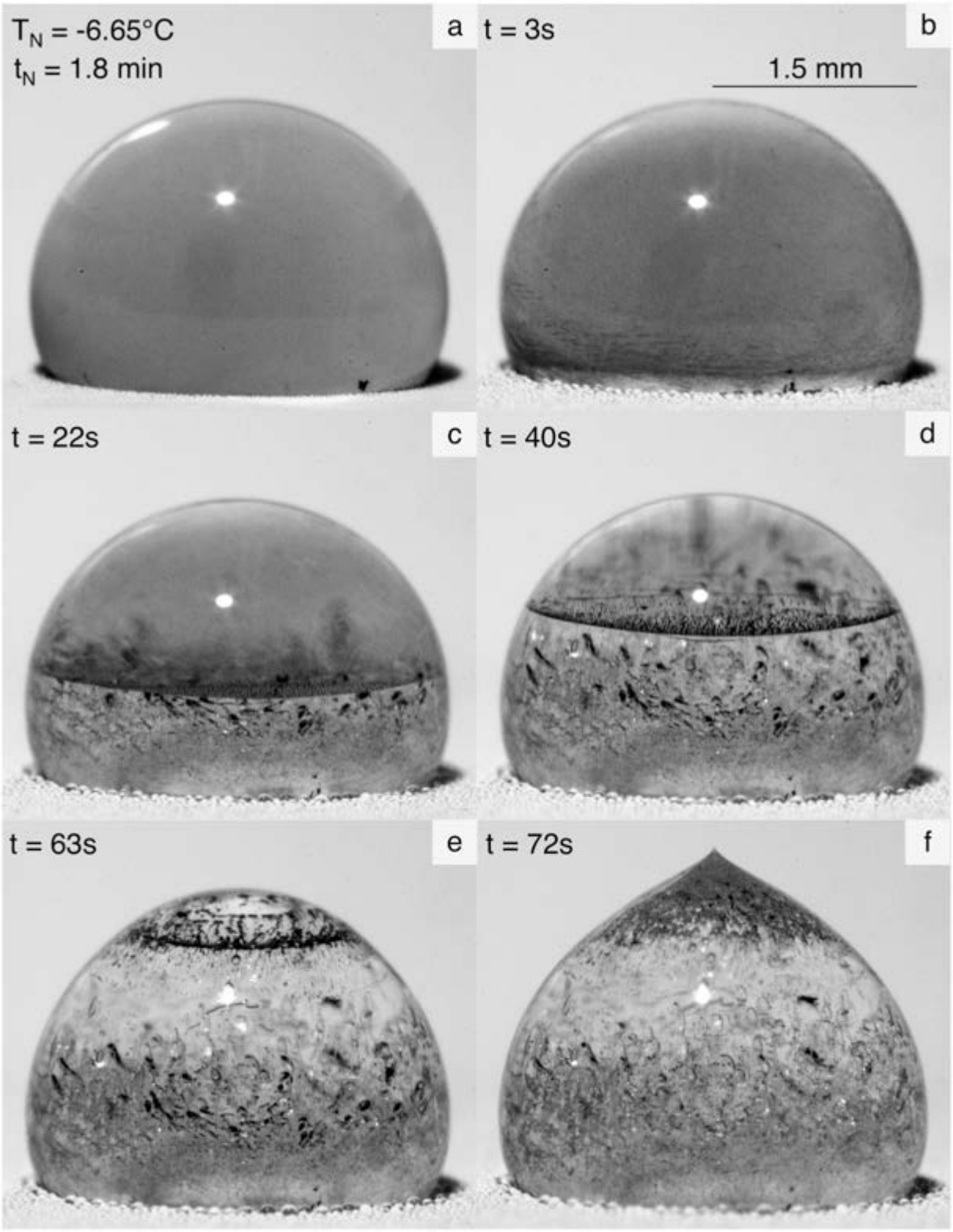

Figure 3.8. Crystallization of a 20 ppm MWCNT-water nanofluid droplet at a cold plate setting of -10 °C.

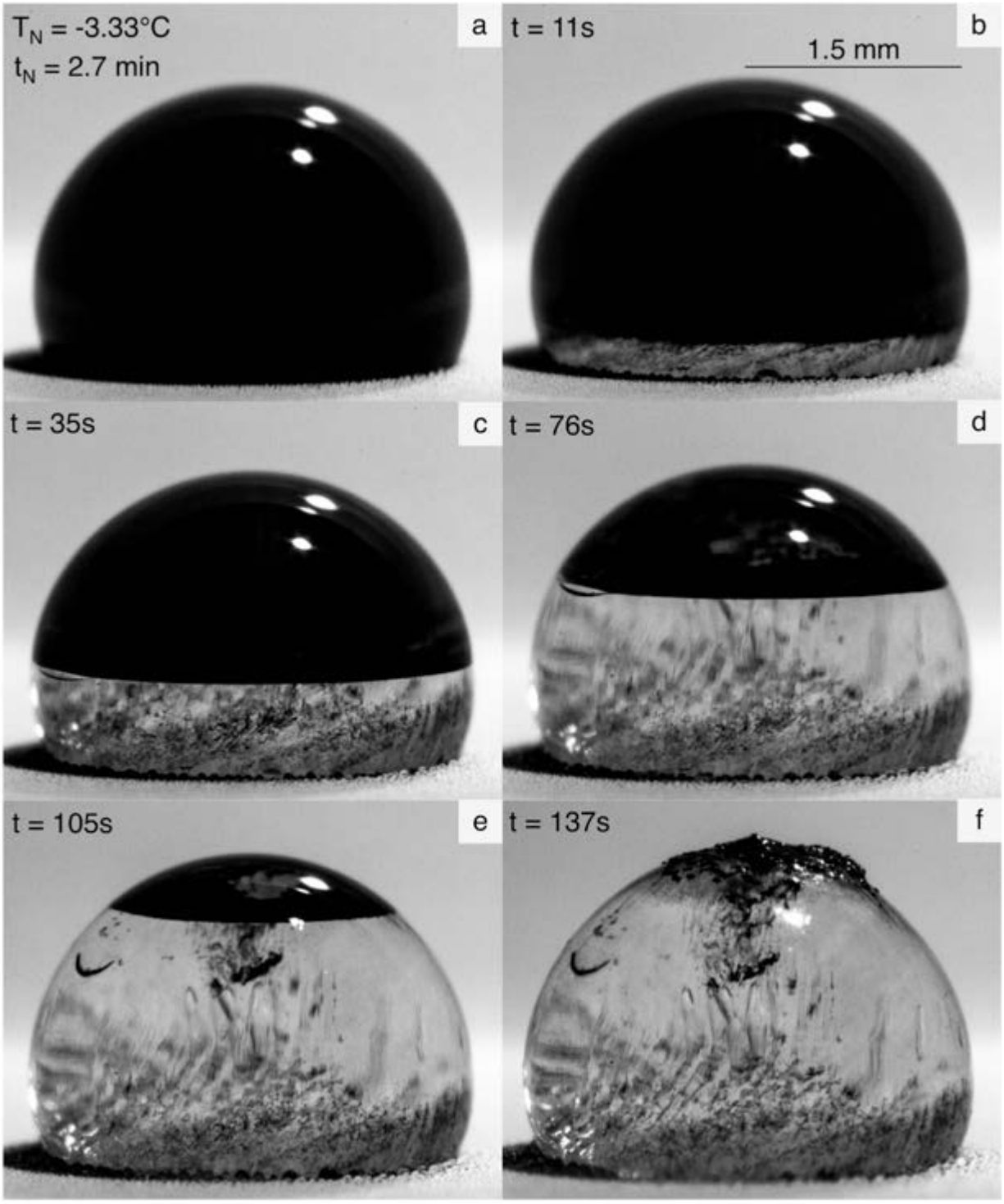

Figure 3.9. Crystallization of a 100 ppm MWCNT-water nanofluid droplet at a cold plate setting of -10 °C.

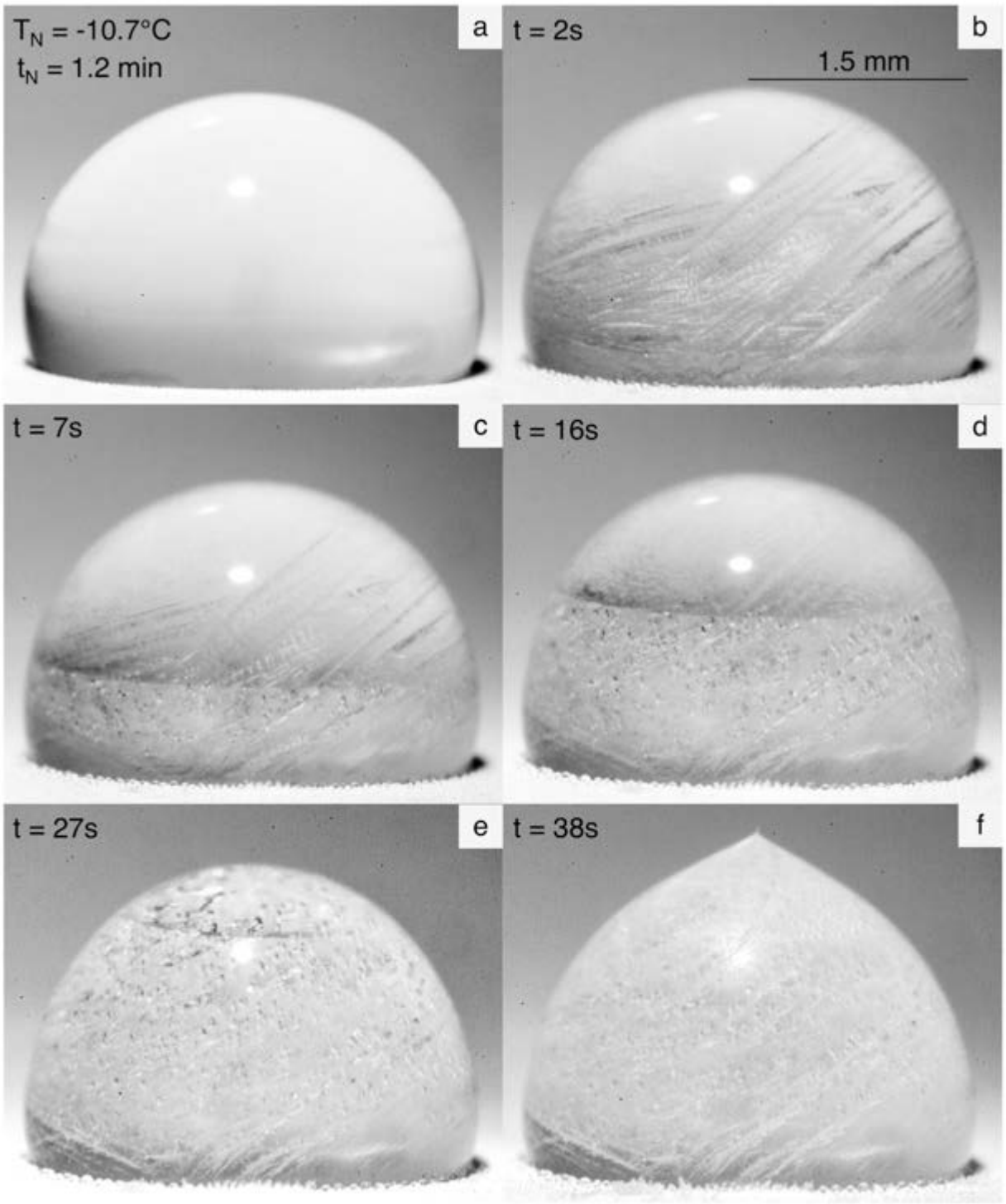

Figure 3.10. Crystallization of a pure water droplet at a cold plate setting of -20 °C.

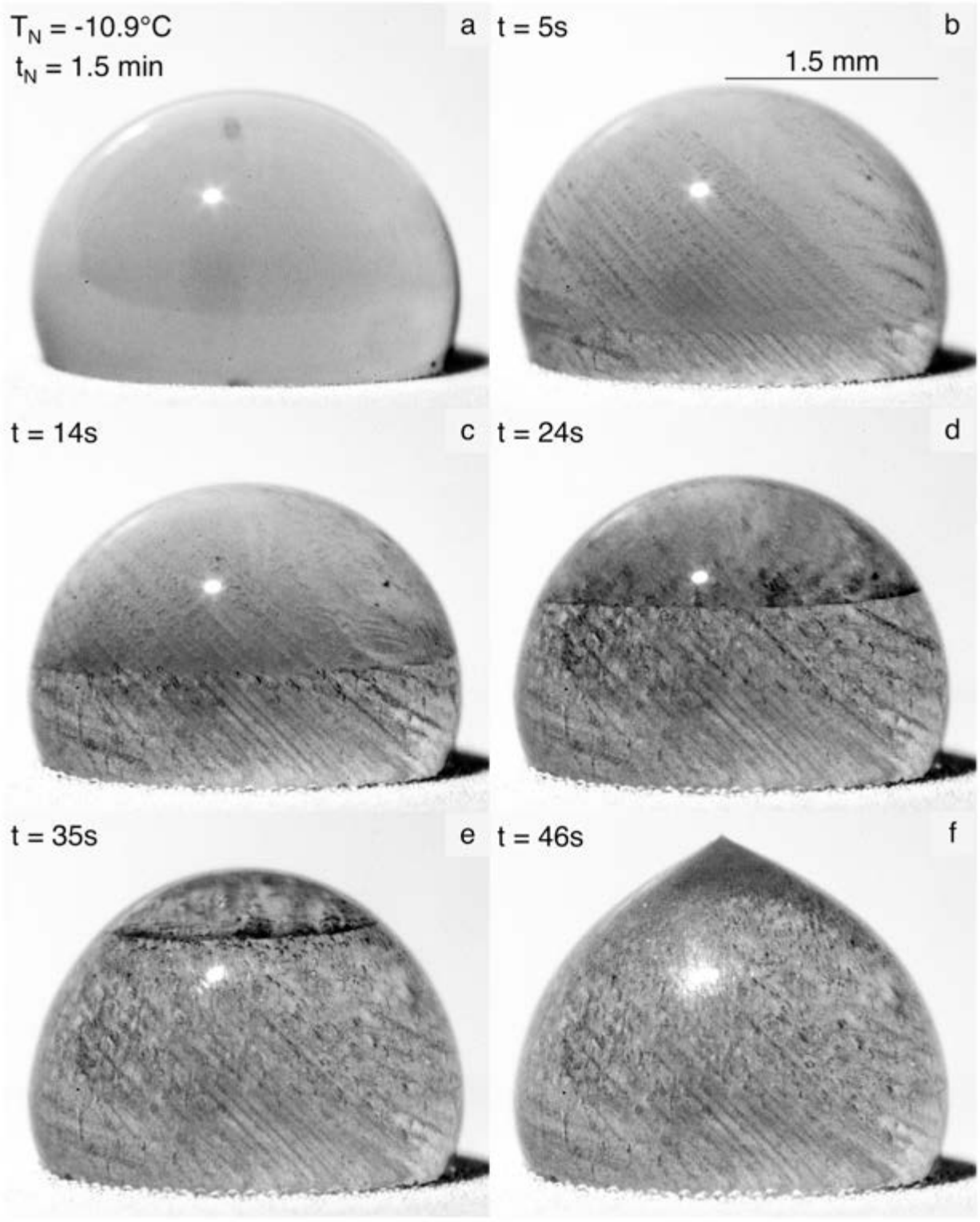

Figure 3.11. Crystallization of a 20 ppm MWCNT-water nanofluid droplet at a cold plate setting of -20 °C.

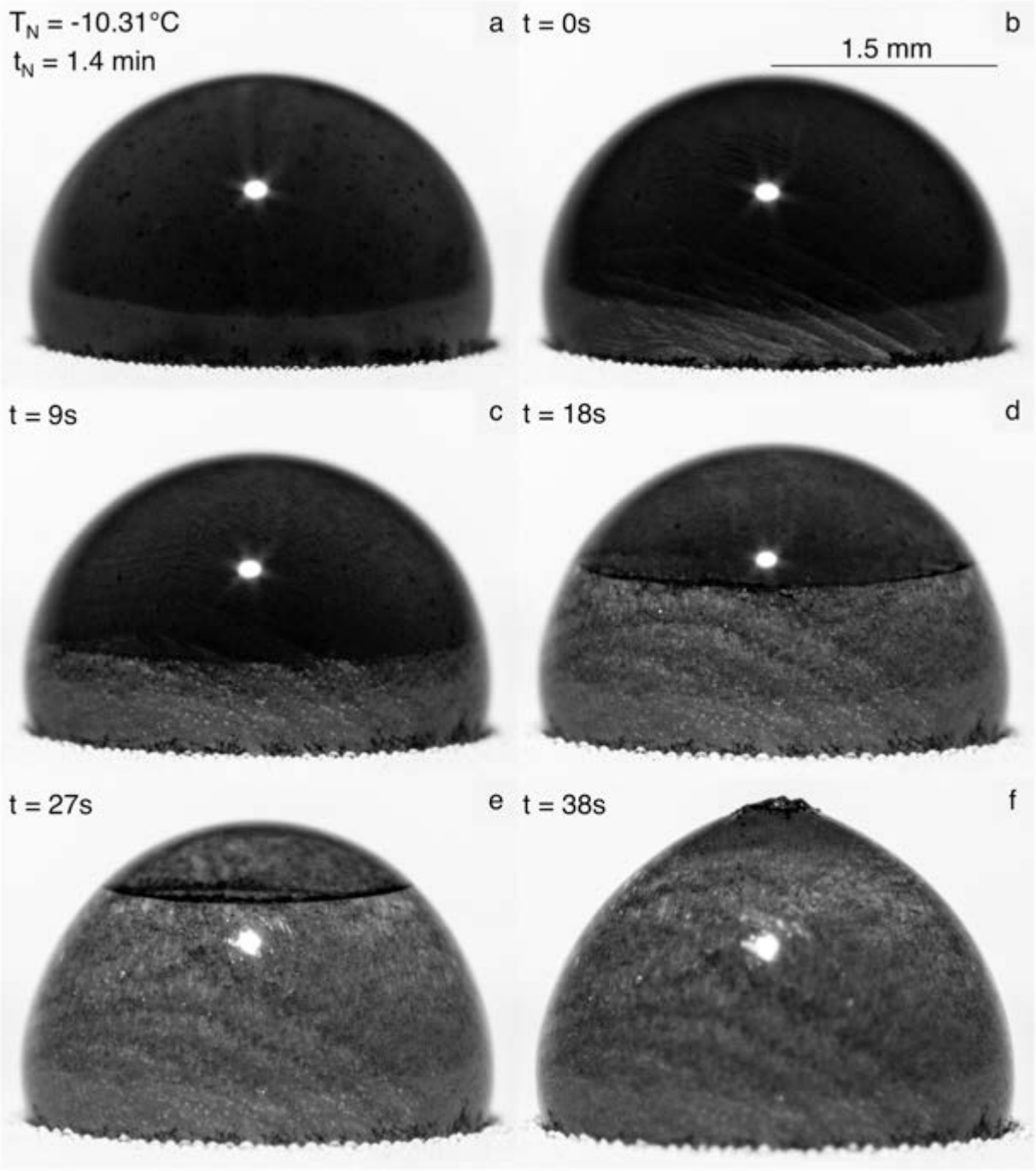

Figure 3.12. Crystallization of a 100 ppm MWCNT-water nanofluid droplet at a cold plate setting of -20 °C.

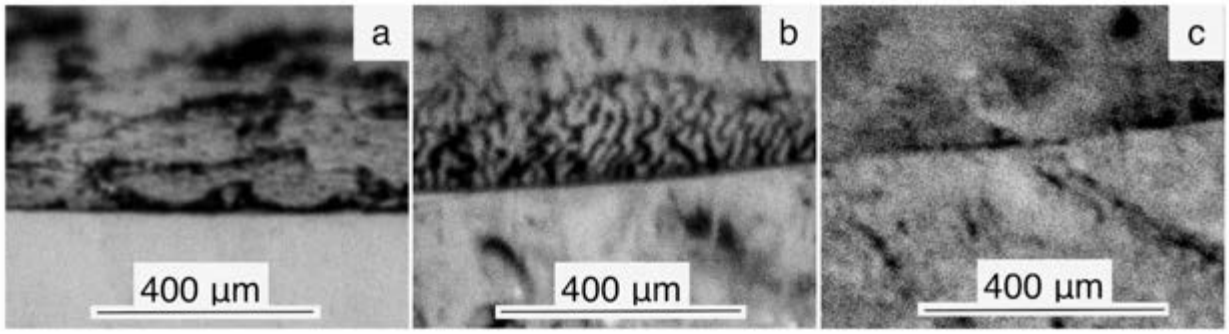

Figure 3.13. Close-up images of the solid/liquid interface for 20 ppm MWCNT-water nanofluid droplets. Left, -5 °C (Figure 3.5d); middle, -10 °C (Figure 3.8d); right, -20 °C (Figure 3.11d).

The rejection of colloids from a solidifying host material has been reported in the literature with the common principle that the degree of particle exclusion is inversely related to the degree of supercooling of the system (Bolling and Cissé, 1971; Cissé and Bolling, 1971; Siegel, 1977; Potschke and Rogge, 1989; Wilde and Perepezko, 2000; Peppin et al., 2008). The tendency of a system to exclude solid impurities is an interplay between the thermodynamics and kinetics of crystallization. From a thermodynamic standpoint, the solubility of most foreign particles (dissolved or colloidal) in ice is quite low, and the crystal system nearly exclusively favors lattice homogeneity (Petrenko and Whitworth, 2002). However, the influence of crystallization kinetics is significant in particle dispersion as well. The slow growth rates at lesser driving forces enable the developing crystal to assemble into the preferred homogeneous array. The faster rates at higher driving forces cause the congruity of the solidifying matrix to be conceded in favor of the propensity to fully crystallize. Note that, even while frozen, it is always energetically desirable for the system to exclude impurities, and over extended time frames, the lattice would undergo solid-state adjustments to removed MWCNTs (and air volumes) and to correct irregularities (Mullin, 2001).

The speed at which particles become trapped within the solid matrix is known as the critical velocity, and many experimental and theoretical investigations have attempted to determine this value for dispersions of various materials in water and ice (Cahn et al., 1964; Bolling and Cissé, 1971; Cissé and Bolling, 1971; Korber et al., 1985; Potschke and

Rogge, 1989; Rempel and Worster, 1999; Okawa et al., 2001; Garvin and Udaykumar, 2004; Garvin et al., 2007b, a; Peppin et al., 2007; Peppin et al., 2008). These studies have demonstrated that the critical velocity is inversely related to particle size; however, beyond this point, categorizing the behavior of different particle systems becomes complex due to the multitude of parameters influencing particle inclusion. Typically, the encapsulation process is simplified as a balance between drag forces within the fluid and repulsive Lifshitz-van der Waals forces. Drag forces push particles toward the solid interface, whereas Lifshitz-van der Waals forces act in the opposite direction to propel particles into the liquid (Agaliotis et al., 2012). Spherical particle shapes are assumed, with particle diameters on the order of 10-50 μm, where buoyancy or Brownian effects are thus neglected. For the current nanofluid system, the cylindrical shape of MWCNTs, as well as their increased thermal conductivity relative to pure water that leads to a concave interface structure, increases the drag force on the MWCNTs and thus their tendency to be incorporated into the solid. However, their nanoscale sizes, at least an order of magnitude lower than the particles investigated in the previous studies, and hydrophilic surface treatments, which combined allow for Brownian dispersion, favor retention in the liquid phase. Considering that the MWCNT nanofluids frozen under these temperature conditions exhibit very little particle dispersion within the solid ice matrix itself, it is anticipated that the latter effects dominate. As temperature decreases, crystal imperfections such as air volumes and fault lines (mostly through dendrites) are introduced (Hallett, 1964). The MWCNTs appear to be preferentially confined in clusters within these pockets and interdendritic spaces (which is best visualized in Figure 3.13). Under the coldest condition, dendrites and air bubbles become finer, which leads to smaller MWCNT masses; however, individual particle dispersion was still not perceived in the ice matrix. Perhaps more severe freezing rates are required to achieve this. The crystallization velocities obtained in this study, albeit approximate, range between 6 and 60 μm/s. These values lie anywhere from well below to on par with the critical values observed with much larger particles in other systems (Agaliotis et al., 2012). Therefore, it appears that the critical velocity for the current MWCNTs was not reached in these experiments. However, the presence of air bubbles within both the

solid and liquid likely has a significant impact on crystallization kinetics that may mask certain nanotube effects.

A further consequence of driving force and MWCNT exclusion can be observed regarding the vertical expansion of the solidifying droplets. For each condition, the height of the solidified droplet relative to the height of the liquid droplet was calculated, and the data are presented in Table 3.3. The largest increase in height was observed for the -10 °C condition, which is likely due to the presence of large bubbles, which are nonexistent at the -5 °C setting and are present but to a smaller extent at the -20 °C setting. At a given driving force, it can be seen that the percent change was much less in systems containing nanotubes at the -5 and -10 °C settings, whereas they were relatively similar at the -20 °C setting. The blanket of nanotubes formed under these conditions along the interface could reduce the vertical expansion of the droplets and promote horizontal growth. This would lead to wider droplets, and while no meaningful changes were measured for lateral enlargement, even minor variations yield considerable volume effects. Furthermore, since the speed of crystallization is apparently lowest for MWCNT-containing systems under the same conditions, the settling of agglomerates at the interface (Figure 3.13) likely has an effect on crystallization kinetics. The presence of a compact and thickening MWCNT layer could have a significant impact on the heat and mass transfer fields at the interface (Potschke and Rogge, 1989). The temperature gradient could be perturbed, and the supply of water molecules to the developing solid could be severely impeded. Gravity effects may also play a role, as the weight of the particles may hinder front propagation (Sanz et al., 1987). Therefore, it is possible that the nucleation temperatures for the morphological experiments, calculated from the crystallization velocities, are artificially reduced. However, these results clearly demonstrate that the morphology of crystallizing nanofluids is strongly dependent on crystallization velocity and, in turn, driving force.

Table 3.3. Relative change in droplet height due to freezing

	Percent Change		
Sample	-5 °C setting	-10 °C setting	-20 °C setting
Water	14.4	22.8	17.7
20 ppm MWCNT	10.3	22.0	20.4
100 ppm MWCNT	3.88	14.6	17.8

3.5.3 Melting of Frozen Droplets

In order to assess the stability of the MWCNTs after undergoing a complete liquid-to-solid conversion process, the frozen droplets were melted at room temperature, and the visual characteristics of the resulting nanofluid were examined. Figure 3.14 demonstrates the behavior of a 100 ppm MWCNT nanofluid thawed from cold plate settings of (a) -5 °C and (b) -20 °C. The time required to melt is indicated as t_M. These images show that the solidification process results in a significant loss of MWCNT dispersion. This effect is observed at both concentrations tested. As opposed to the homogeneous dark appearance of the nanofluid prior to freezing, the liquid is a contrast of numerous clusters scattered throughout an otherwise transparent fluid. The sizes of the clusters were once again related to the degree of supercooling. Through image analysis, it can be seen that lower levels of supercooling yielded larger (tens to hundreds of micrometers), more fiber-like clusters, likely due to the crater formation atop the droplet. Higher levels of supercooling produced finer (tens of micrometers) clusters, as a result of rapid local entrapment within the matrix. In closed systems (to limit evaporation of water) with larger volumes (data not shown), these clusters settled to the bottom of the liquid after a few hours, leaving a very clear liquid solution above. Particle sedimentation indicates that the sizes of MWCNT clusters created during freezing are too large for Brownian agitation to outweigh gravity effects (Taylor et al., 2013). Ultrasonication was then used in an attempt to separate the MWCNTs and recover individual suspension. After 1 h of intense sonication, no meaningful change was

observed. This difficulty in recovering a uniform dispersion suggests a strong association between the MWCNTs and ultimately a destabilized colloidal system.

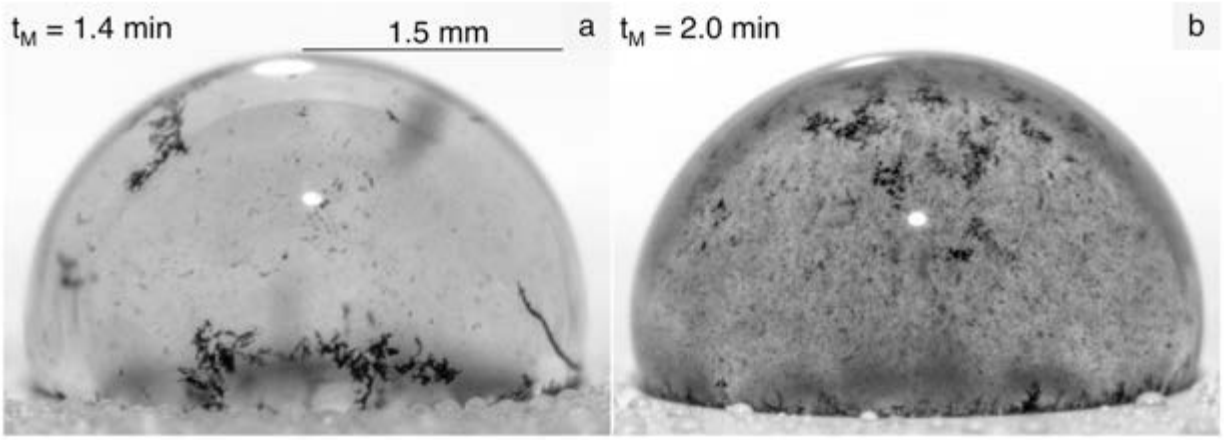

Figure 3.14. Melted droplets containing 100 ppm MWCNT frozen at -5 °C (left) and -20 °C (right).

At this point, the mechanism behind this interaction is thought to be due to a combination of two factors. The incorporation of water into the solid phase during crystallization effectively increases the mass fraction of nanotubes in the remaining aqueous phase, similar to a drying process. Since the probability of collision is proportional to concentration, the increased concentration of MWCNTs in the liquid, and especially at the interface, could lead to physical entanglement between particles. Considering their high aspect ratio (~32) and string-like structure, it is possible that the intertwining of just a few nanotubes would generate knots or bundles capable of sedimentation. Second, the increased proximity of nanotubes due to the drying effect, as well as the high pressures experienced within ice as a result of the expansion of water during phase change (Visagie, 1969) could push the repulsive interaction potentials between particles into an attractive regime (Amrollahi et al., 2008). Furthermore, the existence of an electrostatic double layer between particles requires a liquid solution for charged ions to dissolve (Hordy et al., 2014). The removal of the base fluid and the creation of a crystal matrix could alter both the concentration and distribution of charges in both phases in a manner that is no longer favorable for interparticle repulsion, leading to colloidal destabilization due to van der Waals attraction. This is especially significant since, despite surface treatment, MWCNTs are inherently

hydrophobic. It is thus expected that the destabilization of MWCNTs is due to a combination of physical entanglement and attractive forces between particles. Since this interaction is at a deep energetic minimum at these close distances, separation of MWCNTs is not spontaneous and hence requires aggressive resuspension techniques in order to overcome these strong association energies (Chang, 2000). Ryglowski et al. (2010) also reported destabilization of CNT + surfactant systems after freezing cycles at -13 °C using electrical resistance tests. Interestingly, this group was able to recover dispersion through ultrasonication, which could be related to differences in nanotube characteristics. Since the successful operation of nanofluid technologies hinges on maximizing individual particle dispersion in every phase, the loss of MWCNT stability due to freezing raises some important considerations. First, the varying magnitude of particle dispersion and stability within the solid and liquid phases as a function of supercooling could give rise to inconsistent properties in both phases throughout crystallization. Moreover, since the stability of the MWCNTs is lost after a single freezing event, multi-cycle and full conversion analyses are important for establishing both the benefits and challenges surrounding colloidal technologies. Finally, during cooling applications as well as storage and transport, the integrity of the nanofluid could be compromised if freezing environments are encountered; therefore, care should be taken to avoid exposure to such conditions.

3.6 Conclusions

The crystallization behavior of sessile droplets composed of two concentrations of surface-functionalized MWCNTs in water was evaluated at three driving force temperatures. The dispersion of the MWCNTs within the solid droplet was highly dependent on the degree of supercooling at both concentrations tested. The slow rate of crystallization at low driving forces resulted in the complete expulsion of MWCNTs from the crystal into the liquid. As the speed of solidification increased at higher driving forces, the MWCNTs became embedded within the solid droplet; however at no supercooling was individual particle dispersion achieved within the ice matrix itself, as the nanotubes were driven into sites of crystal imperfections. The formation of clusters

during freezing and upon melting indicates that the crystallization of the base fluid ultimately destabilizes the nanoparticles due to nanotube entanglement and attraction. To the best of our knowledge, this is the first study to investigate the crystallization morphology of aqueous MWCNT nanofluids and to characterize nanofluid behavior at varying levels of supercooling. As the success of any nanofluid is highly contingent on the degree to which the nanoparticles remain dispersed in the base medium, these results bring important considerations for transport and storage of nanofluids as well as emerging applications targeting their use in phase change enhancement.

3.7 Acknowledgements

The authors are grateful for the financial assistance provided by the Natural Sciences and Engineering Council of Canada (NSERC), the Fonds de recherche du Québec – Nature et technologies (FRQNT), the Faculty of Engineering (MEDA scholarship – Hydro-Québec and Vadasz fellowships). The authors would also like to thank Larissa Jorge for synthesis of the MWCNT nanofluids.

Chapter 4

Ice-Dependent Liquid-Phase Convective Cells during the Melting of Frozen Sessile Droplets Containing Water and Multiwall Carbon Nanotubes[1]

4.1 Preface

This study examines the melting side of the liquid-solid phase change process as a sequel to the freezing study in Chapter 3. The literature surrounding the melting process of MWCNT-ice systems is relatively scarce, as is the literature pertaining to the transport processes occurring in the melting of ice droplets. The objective of this study was to investigate both of these aspects through visual characterization of bottom-melted ice droplets containing MWCNTs. Once again a droplet geometry was chosen as it is an easy system to visualize and the mechanisms governing transport can be extended to other geometries.

[1]Reproduced with permission from "Ivall, J., Renault-Crispo, J. -S., Coulombe, S., Servio, P. Ice-dependent liquid-phase convective cells during the melting of frozen sessile droplets containing water and multiwall carbon nanotubes. *Int. J. Heat Mass Transfer*. 2016, 101, 27-37." Copyright 2016 Elsevier. DOI: 10.1016/j.ijheatmasstransfer.2016.05.053

4.2 Abstract

The melting of frozen water droplets is a fundamental and ubiquitous process and the study of the transport processes occurring within the system during phase change is essential to understanding the forces that govern it. Multiwall carbon nanotubes (MWCNTs) can be added to liquid systems prior to crystallization in order to modify the properties of the phase change process and of the liquid or solid systems themselves. In this study, the melting behavior of frozen sessile droplets composed of water and 50 ppm of either pristine or functionalized aqueous MWCNTs is investigated. Droplets are thawed from their based on a hydrophobic substrate set to temperatures between 1 and 30 °C. Tracking of MWCNT clusters during melting shows convective fluid motion occurring within the liquid melt at temperatures above 5 °C. This circulation is contingent on the presence of the ice phase above. The internal fluid dynamics are attributed predominantly to thermocapillary effects as a result of temperature-induced surface tension gradients along the air/liquid interface in the melt. Further, the melting times of MWCNT-containing systems were longer than pure water samples. These results highlight new and important mechanisms driving the melting processes within water droplet systems.

4.3 Introduction

The existence of stationary water droplets on surfaces is a universal phenomenon in nature and industry, and it plays a significant role in countless physical processes. Tiny beads may linger on a surface after contact with a liquid, yet the widespread and continuous transition of water between its three phases is also a steady source of droplet creation. Liquid drops may arise from the condensation of water vapor or through the melting of ice, and solid drops result from the deposition of water vapor or the crystallization of water. While natural systems exhibit a certain resiliency to these processes, droplet formation in industrial or man-made settings is generally problematic with regard to equipment and machinery. For example, continuous droplet impingement on steam turbine blades causes erosion and wear (Engel, 1978), while

impact freezing of supercooled droplets on wind turbines and aircraft components leads to measurement errors, power losses and mechanical failures (Thomas et al., 1996; Parent and Ilinca, 2011). In these contexts, droplets usually evolve from a phase change on a cold substrate, and significant research is directed toward understanding the vapor condensation, deposition or liquid freezing processes in order to mitigate formation on the material surface. Most substrates tested exhibit varying degrees of hydrophobicity since anti-wetting or ice-shedding characteristics are desirable for a wide variety of applications, especially those wishing to prevent water or ice accumulation (Menini and Farzaneh, 2011; Ling et al., 2016). Interestingly, relatively less attention has been focused on the melting of a frozen droplet on such surfaces, which is especially relevant considering that active heating is a common anti-icing technique.

The general melting behavior of water is studied for a multitude of purposes that range from common scenarios such as an ice mass immersed in water (Schenk and Schenkels, 1968), to phase change materials (PCM) for latent heat thermal energy storage systems, to geophysical processes occurring in river, lake and ocean systems (Fukusako and Yamada, 1993). Under certain conditions within melting systems, convective motion develops in the liquid melt, which significantly augments fluid transport. These instabilities were first documented in detail by Bénard (1900b) in thin liquid layers and were linked to the presence of thermal gradients within the system. The non-uniform temperature fields were then mathematically proven by later researchers to generate surface tension forces (Pearson, 1958) and/or buoyancy forces (Rayleigh, 1916) that set the fluid into motion. Surface tension-driven convection, also known as thermocapillary convection, arises from the stronger cohesive forces between colder molecules along an interface exerting a contractile force on warmer molecules. Momentum is then transmitted to the bulk interior by viscous forces, establishing circulatory fluid motion (Hegseth et al., 1996). Density-driven convection, also known as thermogravitational convection, results from the expansion and rise of heated fluid, and the sinking of colder fluid. Whether a system is under surface tension or density control – or a combination of the two – is greatly dependent on the geometry of the system, the applied heat flux, the properties of the material substrate, and the thermophysical properties of the fluid (Chandrasekhar, 1961; Nield, 1964). In the past century, a large number of experimental

and numerical analyses have been conducted that examine several combinations of the above-mentioned parameters in order to characterize these instabilities. The unidirectional melting of water has been predominantly studied in horizontal layers, such as rectangular and cylindrical containers (Yen, 1968; Yen and Galea, 1969; Sparrow et al., 1976), or in spheres melted radially from the exterior (Dumore et al., 1953; Merk, 1954; Schenk and Schenkels, 1968; Vanier and Tien, 1970). To the best of our knowledge, the case of a bottom-heated frozen water droplet has not been investigated.

Many technologies are also exploring the benefits of introducing nano-sized solid-phase additives to the process fluids in order to enhance or introduce new properties to the system. If no agglomeration takes place, the nanoparticles (at least one dimension < 100 nm) can remain in suspension indefinitely since Brownian agitation predominates over a settling force such as gravity (Choi and Eastman, 1995; Yu and Xie, 2012). One type of dispersed nanoparticle-host system that garners significant attention is the multiwall carbon nanotube (MWCNT) nanofluid (Iijima, 1991; Qian et al., 2002). The hydrophobic nature of MWCNTs makes them predisposed to agglomeration in a polar solvent. Two main approaches are employed to preserve particle separation in the liquid. A simple method is the use of surfactants that coat the nanotubes and stabilize them in water. Alternatively, the outer surfaces of the MWCNTs can be functionalized with covalently-bound polar groups to intrinsically promote interaction with water (Tasis et al., 2006; Vandsburger et al., 2009; Jorge et al., 2015). This second approach is more robust and reduces the chemical complexity of the system, as well as any undesirable secondary effects due to the additives (Taylor et al., 2013). MWCNTs offer tremendous strength-to-weight ratios and exceptional thermal and chemical resistance, but they are probably most renown for enhancements in broadband light absorption and thermal and electrical conductivity (Yu and Xie, 2012; Taylor et al., 2013). MWCNT nanofluids are thus regularly evaluated for improved energy collection and heat transport properties in liquid media. Recently, testing has begun to assess the behavior of MWCNT nanofluids for phase change applications. Regarding enhanced boiling scenarios, there is a wide disagreement surrounding improvements in heat transfer characteristics, however MWCNT nanofluids consistently increase the critical heat fluxes (Park et al., 2011; Taylor et al., 2013). Hordy et al. (2014) also demonstrated that

surface-treated MWCNTs remained stable in solutions undergoing boiling conditions. In solidification processes, MWCNTs have been reported to enhance the rate of nucleation, the speed of solidification and the total conversion of the base fluid, each of which increases the efficiency of the phase change process (Wang et al., 2008; Mo et al., 2011; Kumaresan et al., 2012; Kumaresan et al., 2013; Chandrasekaran et al., 2014; Jia et al., 2014). MWCNT nanofluids have thus shown great potential to modify the freezing and boiling processes of the base fluid, however their effects on the melting process have been relatively less described.

This study sets out to examine the morphological behavior of a bottom-heated melting sessile ice droplet composed of water, 50 ppm pristine or 50 ppm functionalized MWCNT nanofluid across a range of warm plate temperatures on a hydrophobic substrate. As an essential constituent of the phase transformation scheme, the melting process merits equal study in order to understand the fundamental transport processes governing the interconversion of water between liquid and solid states.

4.4 Experimental Method

4.4.1 Experimental Setup and Materials

The experimental setup is analogous to the one used in a previous report (Chapter 3) and can be seen in Figure 4.1 (Ivall et al., 2015a). The sample plate consists of a thin strip of polytetrafluoroethylene (PTFE, 0.064-0.089 mm thickness) set on top of a copper plate (1.5 mm thickness). Droplet samples are frozen on an Aavid Thermalloy aluminum Hi-Contact liquid cold plate connected to a Thermo Scientific Neslab RTE 740 refrigerated bath/circulator. The process fluid is composed of a 50/50 by volume mixture of ethylene glycol and water. The temperature of the coolant within the bath can be programmed between -40 and 200 °C, and the temperature of the externally coupled cold plate surface is monitored by a 0.25 mm fine-diameter thermocouple probe (Omega, operating range -210 to 2100 °C, accuracy ± 1.1 °C). Droplet samples are melted on a thermoelectric (TE) or Peltier plate with a maximum temperature rating of

70 °C. The temperature of the warm surface is controlled by a National Instruments LabVIEW VI and measured by a general-purpose thermistor (operating range -20 to 100 °C, sensor tolerance ± 1.0 °C between 0 and 70 °C). The droplet sample is visualized by a Canon EOS 60D DSLR camera (18.0 Megapixel CMOS sensor) fitted with a Canon MP-E 65 mm f/2.8 1-5x macro lens. The camera is placed at an angle parallel to the warm plate surface and the focal plane is adjusted with an *x,y,z* multi-axis manual positioner stage in order to capture particle motion midway within the droplet. Videos are recorded at 30 fps. Diffuse illumination is provided by a fiber optic LED light source that is set to a low setting (10% of maximum brightness) along with a white reflective sheet placed behind the sample. In order to minimize air circulation onto the sample and to maximize heating from below, the sample plate and warm plate surface are enclosed in a polystyrene insulation chamber, and together with the remaining components are surrounded by a clear poly(vinyl chloride) cover. The entire apparatus rests on an optical table. Room temperature is read by a Fisher Traceable Jumbo thermo-humidity meter with a -5 to 50 °C measurement range to an accuracy of ± 1.0 °C.

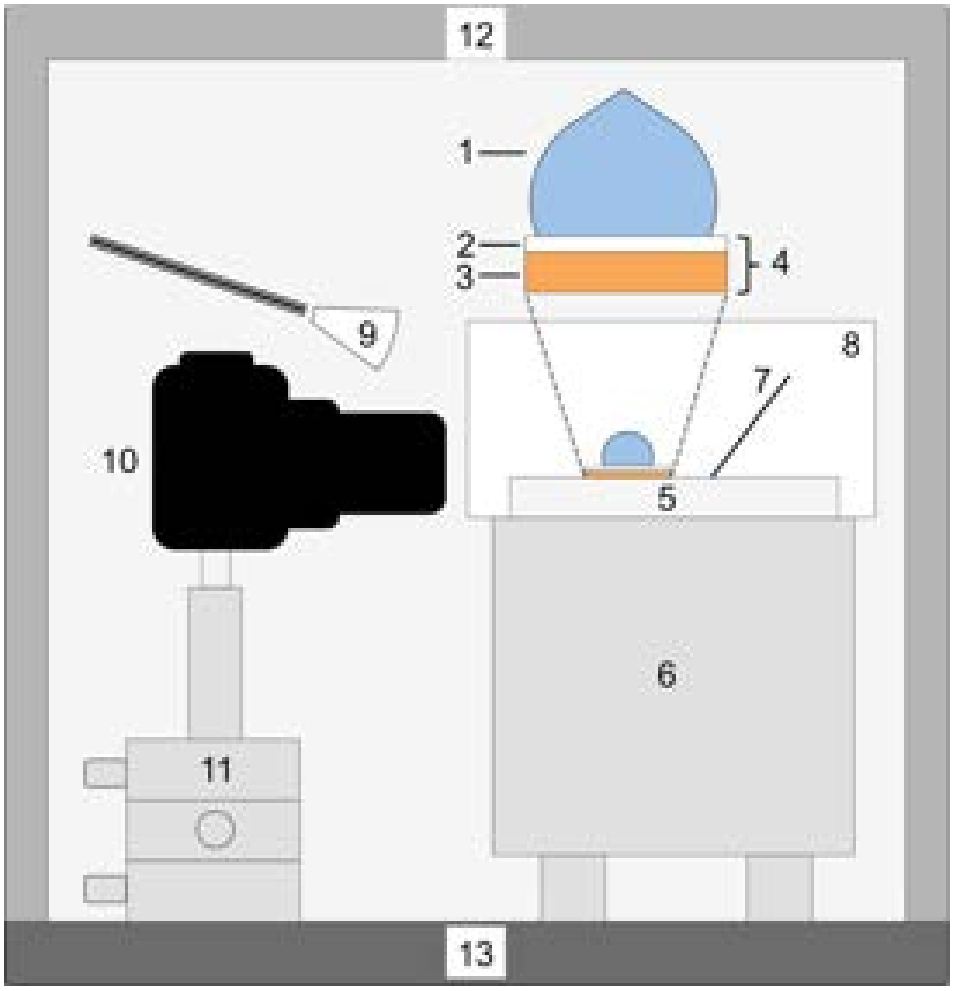

Figure 4.1: Schematic of experimental setup. (1) Sample droplet; (2) PTFE strip; (3) copper plate; (4) sample plate; (5) TE warm plate surface; (6) TE warm plate body; (7) reflective sheet; (8) insulated enclosure; (9) light source; (10) camera and lens; (11) *x,y,z* multi-axis positioner; (12) plastic barrier; (13) optical table.

Multiwall carbon nanotubes (MWCNTs) are produced in-house using a well-documented procedure (Hordy et al., 2013a). MWCNTs are grown on a stainless steel mesh substrate by thermal chemical vapor deposition using acetylene (C_2H_2) gas as the source of carbon, and the iron from the steel as the catalyst for base growth. The produced MWCNTs are hydrophobic, and secondary exposure to a capacitively coupled radio-frequency glow discharge process in an $Ar/C_2H_6/O_2$ gas mixture renders the nanotubes superhydrophilic by grafting polar oxygen groups (CO, COOH, OH) to the outermost wall of individual MWCNTs. To produce the nanofluids, the meshes

containing either pristine or functionalized MWCNT forests are submerged in water treated by reverse osmosis (RO, 0.22 μm filter, conductivity of 10 μS, total organic content < 10 ppb). The sample vial is placed in an ultrasonic bath where intense agitation breaks off the MWCNTs from the mesh and disperses them into the surrounding liquid (no metal substrate is transferred to the fluid). The individual suspended MWCNTs measure on average 1 μm in length and 31.4 nm in diameter, which constitutes an aspect ratio L/D of about 32. The plasma-functionalized MWCNT suspensions are homogeneous and stable for extended periods of time. For more information regarding MWCNT synthesis, characterization and nanofluid preparation, the reader is referred to Baddour et al. (2009), Vandsburger et al. (2009), Hordy et al. (2013a) and references therein.

4.4.2 Experimental Protocol

The temperature of the refrigerated bath/circulator is set to -10 °C while the temperature of the TE warm plate is set to 1, 2.5, 5, 7.5, 10, 20 or 30 °C. When the temperature of the cold plate surface reaches its lowest value (-9.0 ± 0.1 °C) and the temperature of the warm plate equilibrates to the target value, a 10 μL droplet (height 1.85 mm, maximum diameter 2.86 mm) is deposited by micropipette onto the PTFE strip on the sample plate. The sample consists of either pure water, one of two different 50 ppm dispersions of pristine MWCNT nanofluid, or one of two different 50 ppm dispersions of functionalized MWCNT nanofluid. Two independent samples of each type of nanofluid are used to account for possible slight variations between batches. The sample plate is first moved to the cold plate to freeze the liquid droplet. While the droplet is freezing, the camera and light source are turned on. Once the droplet has fully frozen, which is determined visually by a change in opacity and the formation of a pointy tip (Walford et al., 1991), the sample plate is then transferred to the warm plate. The timer is started the moment the sample plate makes contact with the warm plate, after which video capture is initiated. This marks the initial time state $t = 0$ for a melting experiment. The melting process within the droplet is visualized by use of the camera. The timer is stopped upon the disappearance of the solid ice phase. Video recording may

continue in order to assess liquid-phase fluid motion post-thaw. After the experiment is complete, the camera and light source are switched off, and the liquid sample and PTFE strip are discarded. The copper plate is wiped dry and a new strip of PTFE is laid on top. The PTFE strip is replaced every trial as the sedimentation of clustered nanotubes along the surface may alter the properties at the droplet-PTFE interface during a subsequent experiment.

4.4.3 Particle Speed Determination

The streamlines and velocities of the fluid motions are determined using an open-source MATLAB® script adapted from the predictive three-frame best-estimate algorithm developed by Kelley and Ouellette (2011). The velocity fields within the droplet are obtained by focusing the image to the middle plane of the droplet and tracking the black MWCNT clusters. A five-second segment is selected from a video file and decomposed into individual picture frames. The particle tracking software then creates a pixel-values averaged background image of all the frames, thereby eliminating motion. The software is set to recognize a black-on-white contrast and tracks darker particles on a greyed background. After being optimized for this system, the program tracks particles that are about 4% darker than the background and larger than 27 μm^2 (the average cluster size is approximately 20 μm^2, based on visual determination). A velocity arrow represents the motion of a particle during a one-frame time segment (1/30 s). These vector segments are then compiled on a two-dimensional plot where streamlines are visualized over time. Relating the dimensions of the droplet to the number of pixels in the image, the magnitude of the particle velocity is calculated using the scalar dot product of the velocity vector over time. An upper limit to particle speed is set at 5 mm/s because above this value the tracking software may skip to other particles in a different streamline. The speed of individual particle vectors can then be selected. The maximum measured speeds are reported for the four best MWCNT runs (two pristine and two functionalized). These are chosen mostly based on the clarity and the quality of the run, since the contrast and focus are critical in speed determination. For a given experimental run, three five-second segments are selected throughout the melting

process. For each time point, the speeds are measured at a minimum of seven locations within the velocity field to obtain a gradient in speeds at varying distances from the center of the vortex. The maximum speed observed across all three time points in a given trial is taken. The maximum speeds of the four trials are then averaged and reported for a specific temperature condition.

4.5 Results and Discussion

4.5.1 Convective Currents within the Liquid Melt Region

Droplets composed of pure water and 50 ppm of either functionalized (f-MWCNT) or non-functionalized (MWCNT) nanofluid were frozen on a PTFE substrate and subsequently melted from below at warm plate temperatures between 1 and 30 °C. Images of the droplet samples throughout the phase change process are presented in Figure 4.2. In a liquid state prior to solidification, the droplets exhibit a uniform black appearance, which is the signature of a well-dispersed and stable nanofluid. Upon freezing at this level of supercooling, the nanotubes are excluded from the growing crystal lattice and are localized to regions of grain imperfections and nucleated air volumes. The phase change process causes clustering of the MWCNTs that results in a destabilized nanofluid upon melting (Ryglowski et al., 2010; Ivall et al., 2015a), as Figure 4.2b demonstrates a relatively transparent liquid speckled with visible black clusters (average diameter of ~5 μm). The onset of melting is marked by the formation of a liquid layer at the base of the droplet between the ice and the PTFE substrate. A very thin shell of liquid also forms along the outside of the droplet at the droplet/air interface. The thickness of this layer remains relatively constant through the melting process, measuring approximately < 0.05 mm. All remaining water converted from solid to liquid accumulates below the floating ice block, and as the ice crystal shrinks it releases contained air volumes and MWCNT clusters into the liquid beneath (Jin et al., 2013). The air bubbles either accumulate along the bottom edge of the ice or rise to the top of the droplet through the thin liquid shell. The droplet also contracts in volume over the course of melting due to the density difference between solid and liquid water

phases (the frozen droplets in Figure 4.2 are actually slightly larger than in their liquid states).

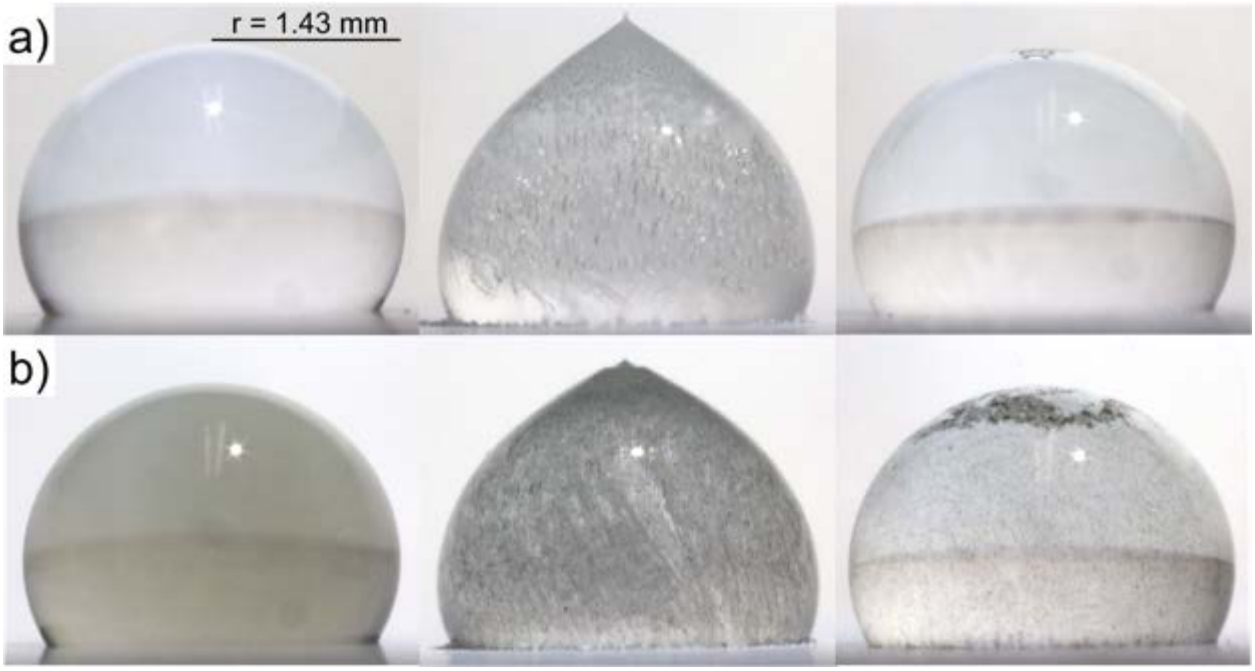

Figure 4.2: Morphology of (a) water and (b) MWCNT nanofluid samples. Left: liquid pre-freeze; middle: frozen; right: melted.

At the 1 and 2.5 °C conditions, the liquid melt region beneath the ice crystal was static in the nanofluid samples. No motion of the MWCNT clusters was observed during melting. This condition is shown in Figure 4.3a and suggests that the melting process within the droplet was primarily under a conductive heat transfer regime. At temperatures of 5 °C and above, convective cells developed within the fluid system along the liquid water/air interface beneath the solid crystal. These regions are highlighted in yellow in Figures 4.3b-e and exhibit a relatively more blurred appearance than the fluid in the center of the droplet. A video of the melting process is provided in Appendix B. A minimum of 20 experimental replicates was conducted each for water and MWCNT nanofluid samples in order to establish whether flow occurred repeatedly at a given temperature. For MWCNT-containing samples, circulation was observed at the 5 °C condition, albeit weakly and transiently. Only about one quarter of these trials formed cells, which endured for a mere few seconds or cycles before breaking down. Above this

temperature, at 7.5 °C and beyond, circulation developed consistently between runs, with velocity increasing visibly with temperature. A schematic of this process is shown in Figure 4.4. In all cases, motion seemed to originate from the edge of the droplet at the air/water interface. The fluid rose rapidly within a very narrow and compressed layer along this edge, and descended slowly over a broad area within the center of the droplet. The vortex was localized to the bottom corner of the droplet. The geometry of the flow patterns was for the most part axisymmetric and toroidal, however sometimes the floating ice was tilted when certain regions contained more entrapped air that altered the center of gravity. This could lead to deviations in temperature fields and in turn the flow fields that might be unfavorable to the development of convective flow in certain regions at certain time points. The sizes of these convective cells were related to the driving force applied. At lower warm plate temperatures, the elliptical currents were small in size and ceased when the ice reached a certain vertical distance (Figure 4.3b). Table 4.1 relates the point at which fluid motion in the liquid stopped to the fractional height of the ice/water interface compared to the total height of the droplet. At more elevated warm plate temperatures, the cells were more extensive, penetrating further into the center of the droplet, and motion persisted for longer periods (Figure 4.3c). At 20 °C and above, the convective cells eventually had widths equal to the radius of the droplet and motion was sustained up until the disappearance of the ice phase (Figure 4.3d). In all cases, the presence of the crystal phase was necessary to both the development and continuation of convective flow. Once the system had fully melted and no ice remained, convective flow was no longer observed in the liquid droplet. Some motion was carried through due to momentum transfer, but this lasted only for a few seconds, and the system appeared quite static (judging by the motion of nanotube clusters).

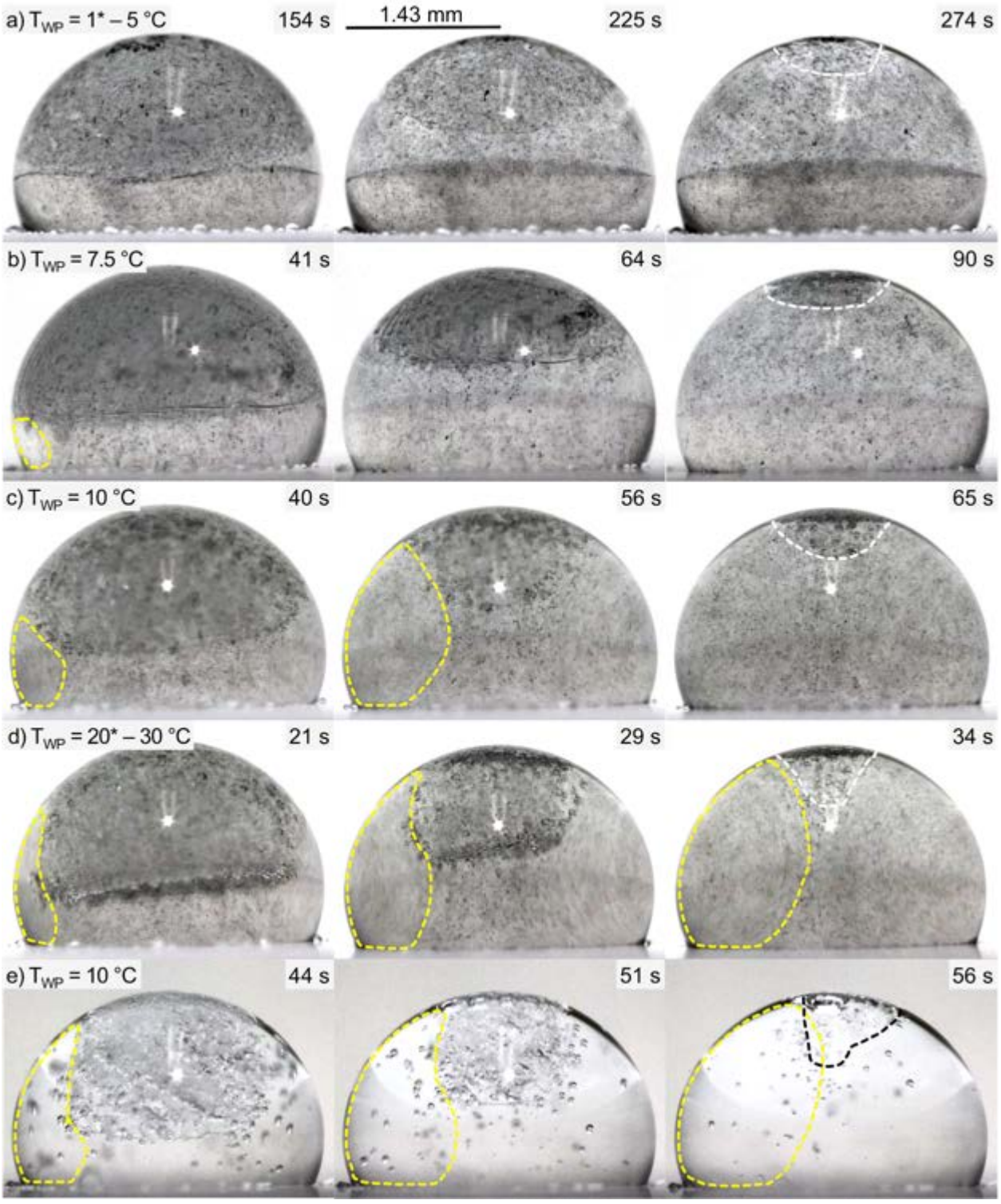

Figure 4.3: Melting morphology of (a-d) frozen aqueous MWCNT-nanofluid droplets and (e) a frozen water droplet at different warm plate temperatures (T_{WP}) and three time points. Regions highlighted in yellow indicate where convective flow currents are occurring in the left hand side of the droplet (motion is toroidal and axisymmetric).

Regions bounded by either white or black dashed lines represent the contours of the floating ice phase. Temperatures marked with an asterisk in a) and d) indicate which specific temperature condition this image sequence corresponds to.

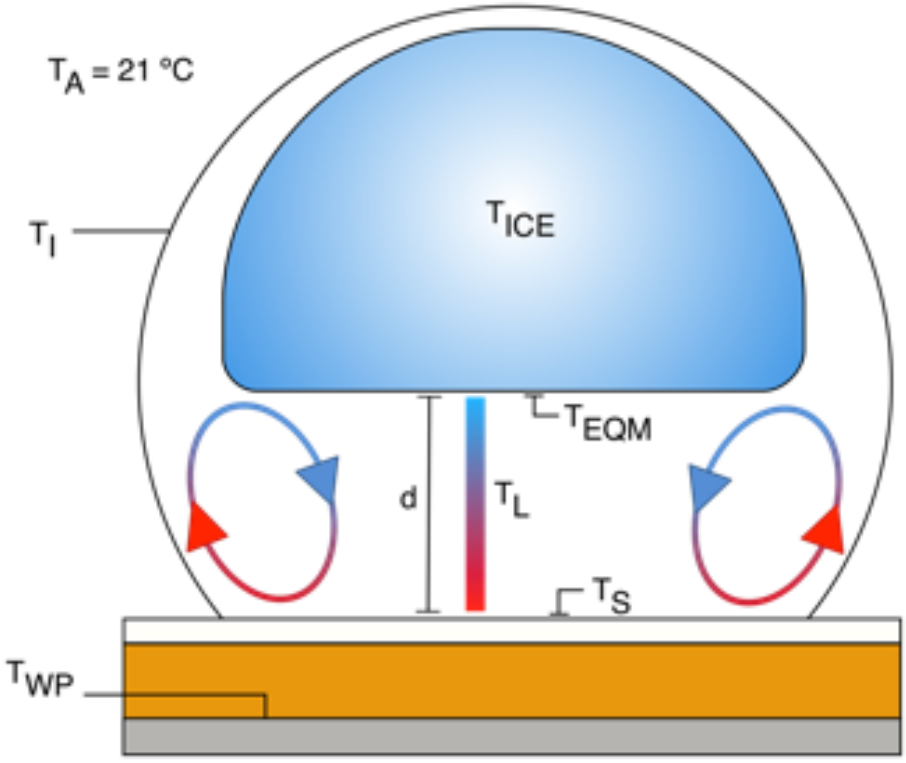

Figure 4.4: Schematic of convective cell patterns and temperature profiles in the experimental droplet system. T_A is the ambient temperature, T_I is the temperature of the fluid at the air/liquid interface, T_{EQM} is the temperature of the fluid at the ice/liquid interface, T_S is the temperature of the fluid at the liquid/PTFE interface, T_{WP} is the temperature of the warm plate surface, T_{ICE} is the temperature of the ice, T_L is the temperature of the liquid melt region and d is the distance between the ice/liquid and the liquid/PTFE boundaries.

Table 4.1: Fractional height of the ice/water interface compared to the total height of the droplet at which point convective fluid motion in the liquid stopped.

Temperature (°C)	System	Fractional Distance
1 – 5	p-MWCNT and f-MWCNT	~ 0
7.5	f-MWCNT	0.61 ± 0.02
	p-MWCNT	0.62 ± 0.02
10	f-MWCNT	0.76 ± 0.02
	p-MWCNT	0.83 ± 0.04
20 – 30	f-MWCNT	1
	p-MWCNT	1

It was difficult to ascertain the occurrence and the extent of convective cells in pure water samples without the presence of tracer particles such as the MWCNT clusters. In some instances the air bubbles released from the bottom of the ice would temporarily become entrained in the liquid streamlines for a few cycles before eventually rising to the top of the droplet. The image sequence in Figure 4.3e shows an example of such an occurrence. This motion provided evidence of convective rolls but it was an infrequent, transient and uncontrollable effect. A secondary indicator of convective flow was the shape of the ice block throughout the melting process. The ice exhibited a hemispherical profile for static conductive regimes at lower warm plate temperatures, and became more square-shaped as convection became more prominent at higher warm plate temperatures. Since motion was always fastest along the air/liquid interface, the melting of the sides of the ice is a result of enhanced heat and momentum transport along this edge. From these indications, it is possible to conclude that motion inside pure water samples sometimes developed at 2.5 °C in the same irregular and faint manner as for the MWCNT samples at 5 °C. Unfortunately, the direction of this motion was unclear in this case. At temperatures of 5 °C and above, pure water samples exhibited motion in the same direction as the MWCNT samples, however the speed of these currents and the point at which flow stopped is unknown.

The velocities of the convective rolls were estimated using a particle image velocimetry (PIV) software package by tracking the movement of the black MWCNT clusters. While MWCNT clustering during solidification of the base fluid may not be ideal from a dispersion standpoint, the size and contrast of the clusters constitute decent characteristics as particle tracers. The sizes of the agglomerates in these experiments are visually estimated to be in the range of 5 μm in diameter. The tracking software is set to detect particles larger than 5.2 μm in order to reduce noise. Longer arrows represent a greater speed, and the streamlines within the fluid generated by the software are shown in yellow in Figure 4.5, where an elliptical pattern of flow can be seen. Unfortunately, mostly only the downward motion of the particles is captured along the circulating roll, as upward motion at the air/liquid interface is difficult for the program to detect due to two limitations. The curvature of the droplet distorts light and reduces resolution at the edges, and the velocity of the particles is so great that it is likely beyond the detection limit of the software (5 mm/s). Despite these challenges, Figure 4.5 shows that the downward motion constitutes a significant portion of the width of the droplet, and the ascending currents are quite thin and constrained to the edge of the droplet. The maximum speeds observed in MWCNT-containing systems were calculated at different temperatures. The maximum speed is selected from a given run since a mean speed depends on the number of vectors chosen, as well as the position and time in the frame. The average maximum speed attained across four runs at a given temperature is reported in Table 4.2 along with a 95% confidence interval based on a Student's *t*-distribution. The highest speeds were observed nearest to the center of the vortex. Table 4.2 suggests that speed increases with driving force, however the values between 10 and 30 °C are within error. Speed corrections for optical distortion were not performed due to software limitations but could provide more accurate estimates (Dash et al., 2014). Literature values for maximum velocities attained within evaporating sessile water droplet systems on hydrophobic surfaces with the same temperature difference are on the order of 1 – 20 mm/s (Tam et al., 2009; Wang and Zhao, 2012), which are comparable to the speeds obtained in the current system. Once again it is difficult to quantify flow in the pure water system. The movement of air bubbles trapped within the streamlines was brief and skewed by drag and buoyancy forces, and the contrast of the

bubbles on the water background was insufficient for tracking. However, it is anticipated that the speed of individual water molecules is greater than that demonstrated by the MWCNT clusters in Table 4.2. As colloidal suspensions, drag forces act on the dispersed MWCNTs that impede motion and reduce speed, an effect that increases with particle size. Larger particles were indeed perceived to move much slower than smaller particles, and to settle more rapidly. While the reported velocities provide only a general benchmark of the actual speeds occurring within the system, the visualization and profiling of the convective flow fields within a melting water droplet is a novel aspect of this study that is made possible by the nanotube clusters.

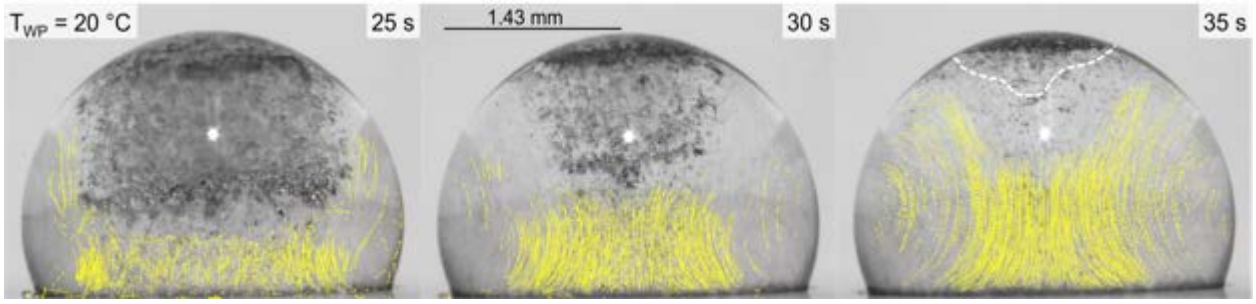

Figure 4.5: Fluid streamlines in a melting water droplet. Yellow vectors: tracked particle streamlines. White dashed line: contour of floating ice phase. Arrow lengths are proportional to velocity.

Table 4.2: Maximum speeds of tracked particles at a given temperature, with 95% confidence intervals based on a Student's *t*-distribution.

Sample	Speed (mm/s)				
	1 – 5 °C	7.5 °C	10 °C	20 °C	30 °C
50 ppm MWCNT	-	1.5 ± 0.6	2.9 ± 0.7	3.9 ± 0.6	3.0 ± 0.3

Convective motion within a fluid of homogeneous composition arises from a non-uniform temperature distribution. In the current system, unidirectional heating from below imposes a vertical temperature gradient in the liquid between the warm plate and the cold ice (as outlined in Figure 4.4). The presence of ice fixes the temperature of the liquid at the ice/water boundary (T_{EQM}) at 0 °C since this is the fusion temperature of water at atmospheric pressure. Therefore, as long as the ice phase exists within the

droplet, there must be water at 0 °C, regardless of the temperature of the warm surface. The temperature of the PTFE/droplet interface T_S is assumed to be constant throughout the melting process and equal to the warm plate temperature T_{WP}. This scenario of a very thin but poorly conducting layer resting on top of an excellent thermal conductor is common in the literature and the above assumption has been consistently validated (Pearson, 1958). It can be verified by a comparison of the characteristic time scales for transient heat conduction in the vertical direction $\tau = d^2/\alpha$ for each layer (Schatz et al., 1995; Tam et al., 2009). At a droplet height of 1.85 mm, these yield τ_{COPPER} = 0.02 s, τ_{PTFE} = 0.07 s, τ_{ICE} = 2.8 s, and τ_{WATER} = 24.0 s. Clearly, the time scale for the temperature response of the sample plate is orders of magnitude less than that for the droplet system in either phase. The air surrounding the droplet is assumed to be stagnant and the ambient room temperature T_A is constant at 21 °C. The warming effect of air on ice is considered negligible compared to the heating provided by the warm surface. Using the Biot number $Bi = hL_C/k$, which weighs heat transport from convection at the interface to heat conduction across the bulk fluid, if h = 20 W/m^{2}K (stagnant air), L_C (critical length) ≈ $r/3$ (sphere) ≈ 5 x 10^{-4} m, and k_{ICE} = 2.22 W/m-K, then Bi = 4.5 x 10^{-3}. Typically values below Bi = 0.1 denote relatively poor convective heat transfer at the air/droplet interface. The parameters T_I, T_L, and d, which correspond to the air/liquid interfacial temperature, the temperature of the liquid, and the distance between the base of the ice and the substrate (or the characteristic length), respectively, are all dependent on position and time. While three interfaces exist in the system, only the air/liquid interface should have a significant temperature gradient across its surface area.

With the framework established, an evaluation of the mechanisms responsible for convection during the melting of a water droplet can begin. The temperature differences created in the system due to heat input generate surface tension gradients along the air/liquid interface and a density gradient within the bulk fluid volume. When imbalances in either of these forces become sufficient, the fluid becomes unstable and convection sets in. These forces are capable of generating instability independently but in systems where both exist, they may act either synergistically or antagonistically,

depending on system geometry (Nield, 1964). The contractile forces arising from surface tension gradients are a monotonically decreasing function of temperature whereby molecules at colder temperatures exert a pulling force on molecules at warmer temperatures. Thermocapillary motion thus proceeds from hot regions to cool regions. Density is also a monotonically decreasing function of temperature and buoyancy-driven convection develops from the rise of warm, light fluid elements and the sinking of cold, dense fluid elements. Typically, thermogravitational flow requires the heat source to be placed below in order to produce gradients opposite to gravity, whereas surface tension gradients may exist in any orientation. Water is anomalous in that its greatest density is not at its melting temperature 0 °C, but at 4 °C, therefore a density inversion occurs in this range and motion proceeds from colder regions to warmer regions.

The direction of the convective rolls observed in the current system are consistent with surface tension-driven mechanisms reported for evaporating droplets in the literature. With the heated lower boundary and the cold ice phase as the upper boundary, the interfacial traction between vertical fluid elements would result in an ascending motion along the liquid/air interface and a descending motion in the center of the droplet (Hu and Larson, 2005; Girard et al., 2006; Tam et al., 2009; Bartashevich et al., 2012; Wang and Zhao, 2012). Buoyancy-driven flow within droplets, as a volume process, has typically been reported to manifest in a pattern opposite to this (Dash et al., 2014). The surface-tension driven mechanism is further supported by the notion that the impetus for circulation visibly originates at the edge. The upward fluid streamline is concentrated, fast-moving, and dominant, while the downward streamlines from particles disseminated into the bulk are wide, slow, and clearly a consequence of the interfacial process (Hegseth et al., 1996). When considering the magnitude of the temperature driving force for both effects, once again the argument points to thermocapillary forces as the principal agent. Any warm plate temperature T_{WP} above 0 °C would induce gradients in both surface tension and density, however the driving force for the former is based on a 0 °C reference point while for the latter is based on a 4 °C reference point. At T_{WP} between 0 and 4 °C, water at the top of the melt along the ice/liquid boundary would be less dense than water at the base of the melt along the heated substrate. The density gradient would be in line with gravity and convection

would not transpire, and thus only temperatures above 4 °C would be conducive to instability. Since flow in pure water samples seemed to initiate at 2.5 °C, this must be attributable to surface tension forces. Furthermore, flow was well established at 5 °C for water and 7.5 °C for MWCNT samples. In these cases, while the temperature gradient is sufficient for both types of instability to form, the driving force for surface tension is much larger than that for density, and thus likely to be the prevailing mode of convection. In some studies, this surface tension mechanism is classified by whether the applied temperature gradient is perpendicular or parallel to the surface that is generating convection (Schatz and Neitzel, 2001). A perpendicular situation is termed Marangoni convection and a parallel situation is termed thermocapillary convection. The current system would fall under the thermocapillary category.

4.5.2 Non-Dimensional Analysis of Flow Regimes

A more quantitative tool that can be used to measure the relative strengths of the thermocapillary to the thermogravitational forces in a convective process makes use of dimensionless parameters. The Marangoni number (*Ma*) weighs surface tension forces to viscous forces and is shown in Equation 4.1. The Rayleigh number (*Ra*) compares heat transfer from natural convection to heat transfer from conduction in a fluid and is shown in Equation 4.2. The Rayleigh number is a product of the Prandtl number (*Pr*) and the Grashof number (*Gr*) and thus multiplies the ratio of momentum to thermal diffusivity by the ratio of buoyancy to viscosity forces. In this form of *Ra* the change in density is embodied through the change in temperature. In the expressions for both *Ma* and *Ra*, temperature and distance are the only changing variables. The dominant mechanism can then be evaluated by dividing *Ra* by *Ma*, yielding what is known as the dynamic Bond (Bo_D) or the Eötvös (Eo) number shown in Equation 4.3, which represents the ratio of the buoyancy force to the surface tension force. Note that $\mu = \nu\rho$ and $\kappa = \alpha\rho C_P$.

$$Ma = \left|\frac{d\sigma}{dT}\right| \frac{\Delta T d}{\mu \alpha} \quad \text{Equation 4.1}$$

$$Ra = \frac{\beta \Delta T g d^3}{\upsilon \alpha} \quad \text{Equation 4.2}$$

$$Bo_D = Eo = \frac{Ra}{Ma} = \frac{\beta \rho g d^2}{\left|\frac{d\sigma}{dT}\right|} \quad \text{Equation 4.3}$$

Table 4.3 lists the symbols used in Equations 4.1 – 4.3. The values of the dimensionless parameters were calculated at each temperature condition and are presented in Table 4.4. The temperature driving force (ΔT) is equal to the warm plate setting since ΔT = $T_{WP} - T_{EQM}$ and T_{EQM} = 0 °C. Due to the difficulties in obtaining interfacial temperature measurements, the interfacial ΔT used for *Ma* is assumed to be equal to ΔT in the bulk fluid used for *Ra*. The material properties of pure water were used for the fluid and are taken from Perry and Green (1997). The influence of the nanotubes on the properties of the system is assumed to be minimal at these low loadings, especially considering that the vast majority of the nanotubes are clustered, which negates any enhancements to bulk properties offered by stable nanofluid dispersions (Taylor et al., 2013). Since most material properties have some degree of temperature dependence, an average value about the midpoint of a given ΔT was used. The negative values for *Ra* at 1 and 2.5 °C are due to the density inversion of water reflected in the thermal expansion coefficient β term. Over the temperature range tested (0 – 30 °C), the decrease in surface tension of water (in contact with air) with temperature is linear ($d\sigma/dT < 0$). The dimensionless parameters were calculated at two distances, d = 1.0 mm and 1.85 mm, which correspond to roughly half of the height of the droplet and the average total height of the droplet, respectively. These characteristic lengths are more related to the geometry of a horizontal fluid layer of thickness *d*, but can also apply to a sphere of radius *d*. ΔT is a fixed term and distance d is the dynamic variable. This scenario constitutes a continuously transient state and a moving boundary layer with phase change, and accounting for the complex geometry coupled with position and time for the convective processes would require numerical analysis, which is beyond the scope of this study.

Table 4.3: List of physical parameters used in Equations 4.1 – 4.3.

Parameter	Symbol	Unit	Value
Temperature difference between warm plate and ice	ΔT	K	See Table 4
Distance between ice boundary and PTFE surface	d	m	1.00 & 1.85 x 10^{-3}
Thermal conductivity of water	κ	W m^{-1} K^{-1}	Perry and Green
Thermal diffusivity of water	α	m^2 s^{-1}	Perry and Green
Dynamic viscosity of water	μ	kg m^{-1} s^{-1}	Perry and Green
Kinematic viscosity of water	ν	m^2 s^{-1}	Perry and Green
Coefficient of thermal expansion	β	K^{-1}	Perry and Green
Density of liquid water	ρ	kg m^{-3}	Perry and Green
Specific heat of water	C_P	J K^{-1} kg^{-1}	Perry and Green
Change in surface tension due to temperature	$d\sigma/dT$	kg s^{-2} K^{-1}	-1.54 x 10^{-4}
Acceleration due to gravity	g	m s^{-2}	9.81

Table 4.4: Dimensionless parameters as a function of temperature and distance in droplet.

ΔT (°C)	d = 1 mm			d = 1.85 mm		
	Ma	*Ra*	Bo_D (= *Ra/Ma*) x 10^{-3}	*Ma*	*Ra*	Bo_D (= *Ra/Ma*) x 10^{-3}
1	647	-1	-1.6	1200	-7	-5.4
2.5	1650	-1	-0.8	3060	-8	-2.6
5	3420	2	0.5	6320	11	1.8
7.5	5280	9	1.7	9770	57	5.8
10	7202	20	2.8	13400	129	9.6
20	15800	105	6.6	29300	662	22.6
30	25300	189	7.5	46700	1198	25.6

Table 4.4 shows that at these distances and temperature ranges, surface tension effects far outweigh buoyancy effects, which are almost nonexistent. The Marangoni values exceed the Rayleigh values by at least two orders of magnitude, reflected by a very small Bond number (e.g. -1.6 x 10^{-3}). Both *Ma* and *Ra* increase linearly with temperature (not accounting for the temperature dependence of other terms in the equations), however the Rayleigh number is much more sensitive to changes in distance due to a third order dependence on *d* compared to the single order dependence of *Ma*. The buoyancy effect

therefore becomes more prominent at larger distances, roughly around the 1 cm mark for the temperature range tested in the current system. The Marangoni and Rayleigh numbers are calculated in the absence of the other's effect, but in the case of coupling the contribution from the Rayleigh term is negligible. At all time points and conditions within the current system, surface tension forces control the convective process. Additionally, this convective motion is wholly dependent on the presence of the ice phase, as the driving force is significantly enhanced by the imposed 0 °C boundary condition. In the absence of ice, the new boundary temperature becomes the atmospheric temperature T_A = 21 °C, the new gradient becomes $\Delta T = T_{WP} - T_A$, and the system transitions to an evaporation process. Convection in the liquid post-thaw was not observed at any temperature in this study.

With regards to the specific condition at which instability might be triggered, critical values for both *Ma* and *Ra* exist in the literature. Note that these values are geometry-dependent and were developed mostly for either an infinite fluid between two horizontal plates or for a perfect sphere, both at steady state. The current problem is a bit more complex in that it comprises a transient, moving-boundary phase change process with a density inversion in a droplet with a shape between that of a hemisphere and a sphere. Many studies have examined convection within melting ice/water systems, but to the best of our knowledge, never before within a droplet geometry heated vertically from below. Convection studies on spherical water droplets typically focus on evaporation. In this case, the horizontal ice and substrate boundaries can be considered rigid and thermally conducting, while the vertical air/liquid boundary in the melt can be considered free and thermally insulating due to the relatively poor heat transfer to the vapor phase. For this scenario, the critical Marangoni number Ma_C that designates the onset of thermocapillary-driven convection usually ranges between 79 and 100, and 80 is the commonly cited value (Pearson, 1958; Nield, 1964; Schatz et al., 1995). The typical critical Rayleigh number Ra_C that designates the threshold for thermogravitational-driven convection is ~3000 for a spherical system and ~1100 for a planar geometry, and tends to be on the order of $10^3 - 10^5$ depending on the system (Chandrasekhar, 1961; Nield, 1964; Sun et al., 1969; Yen and Galea, 1969). Whether the current system is viewed as a horizontal or spherical geometry, the values shown in Table 4.4 illustrate

that these temperature/distance conditions are insufficient for buoyancy-driven convection, while surface tension-driven convection should firmly set in at all conditions, at least theoretically. Experimentally, convection was only observed to begin at 2.5 °C for pure water and 5 °C for MWCNT samples. It is possible that convection in pure water samples occurred at the 1 °C condition but was either too slow or too transient to be detected. The critical numbers only dictate whether convection can occur, not the speed at which particles will travel. Any possible antagonistic effect of buoyancy on surface tension below 4 °C is likely negligible due to a virtually absent gravitational force. The interfacial temperature gradient might also be overstated as being equal to the gradient in the bulk (ΔT). Moreover, both gradients evolve over time and distance, which may play a role in the diminishment of the convective cells throughout the melting process at the 7.5 and 10 °C cases (see Table 4.1).

Pearson (1958) and Scriven and Sternling (1964) proved that thermocapillary-based circulation can take place in very thin films (< 1 cm) and at small temperature differences (1 °C). Small droplet systems such as the current system are typically under surface-tension control due to the relatively large surface area-to-volume ratios inherent to spherical geometries and thus the more substantial contribution of edge effects (Schatz and Neitzel, 2001; Clift et al., 2005). A good visualization of the regime of convection to droplet size is offered by Tam et al. (2009) who performed a scaling analysis of the characteristic time scale for surface tension (τ_{ST}) and buoyancy effects (τ_B) to take place in an evaporating sessile droplet system situated on a superhydrophobic surface. As it happens the ratio between these time scales is proportional to the ratio between *Ma* and *Ra* and thus to Bo_D or *Eo* (see Equation 4.4). Their analysis reveals that the time scale for the onset of buoyant convection equals that for surface tension convection at 1 cm, below which the time scales for surface tension effects to develop are much smaller than those associated with buoyancy effects. Situating the current system on their figure, using the dimensions in Table 4.4, it is well within the Marangoni region and under surface tension control.

$$\frac{\tau_B}{\tau_{ST}} \approx \frac{Ma}{Ra} \approx -\left(\frac{d\sigma}{dT}\right)\frac{1}{\beta\rho g d^2} \qquad \text{Eq. 4.4}$$

The MWCNT-containing samples exhibited a clear difference compared to the pure water samples in that the condition required for observable convection shifted from 2.5 to 5 °C. This indicates that it was more difficult for convective cells to develop when MWCNTs were present. In other phase change systems, the presence of stable MWCNTs has been reported to accelerate conductive melting and to suppress convection (Fukai et al., 2000). Any increase in thermal diffusivity due to the presence of MWCNTs, which would decrease both *Ra* and *Ma*, is likely negligible due to low concentration and clustering. Viscosity and surface tension measurements of stable dispersions (not reported) showed no measurable difference compared to pure water. Destabilized samples were not tested due to the risk of instrument contamination. The three-phase contact angle for all three sample types was measured using a goniometer and found to be 107 – 109°, which is comparable to literature values of approximately 110° (Dash et al., 2014). One explanation for the increased driving force needed for convection to occur surrounds the MWCNT clusters acting as impurities. Other groups have noted the sensitivity of the convective rolls to the presence of impurities at the interface producing motion (air/liquid) as well as along the substrate upon which the droplet rests (liquid/PTFE). In static systems, clusters MWCNTs that do not sediment typically accumulate at an air/liquid interface, and it is possible that in these well-mixed systems, trace amounts of MWCNTs along the interface could reduce surface tension and diminish circulation (Block, 1956; Clift et al., 2005; Hu and Larson, 2005). While the PTFE substrate was changed between runs, the deposition of clusters MWCNTs during a given run was beyond control and could have led to a decrease in stability of the vortices (Tam et al., 2009). An example of this accumulation can be seen from the melted sample in Figure 4.2b. The drag forces experienced by both dispersed and clustered MWCNTs could also reduce the observed speed of the cells.

4.5.3 Effect of MWCNTs on Melting Times

This study initially set out to explore the melting behavior of frozen MWCNT systems as the counterpart to a previous study (Ivall et al., 2015a) on their crystallization behavior. In addition to examining the flow characteristics, for every experiment conducted, the melting times (t_M) of the samples were recorded. The melting times were calculated between when the sample plate was placed on the warm plate and when the ice disappeared at the top of the droplet. A 50 ppm concentration was chosen to increase the chance of discerning an effect after thawing, and varying the concentration became outside of the scope of this report after the observation of the convective cells. The data are presented in Table 4.5 along with a 95% confidence interval. Each result consists of between six to ten experimental replicates. The standard uncertainties (u) correspond to 95% confidence intervals based on a Student's t-distribution. The data are also presented in terms of percent difference with respect to water at every warm plate temperature in Table 4.6 and Figure 4.6. The errors are computed based on the Student's t-distribution. A negative change represents a shorter melting time relative to water.

Table 4.5: Melting times (t_M) of sample droplets at different warm plate temperatures, with 95% confidence intervals based on a Student's t-distribution.

Sample	Melting Time (t_M, seconds)						
	1 °C	2.5 °C	5 °C	7.5 °C	10 °C	20 °C	30 °C
Water	355.1 ± 8.7	221.6 ± 4.7	126.9 ± 2.7	86.5 ± 2.1	62.0 ± 1.5	32.1 ± 0.5	27.3 ± 0.8
50 ppm f-MWCNT	341.2 ± 7.5	216.9 ± 4.6	133.3 ± 2.0	99.6 ± 1.3	70.1 ± 1.6	37.3 ± 1.1	30.6 ± 1.0
50 ppm p-MWCNT	349.2 ± 7.0	215.8 ± 3.3	133.2 ± 1.8	98.3 ± 2.1	68.6 ± 1.5	36.8 ± 0.6	30.6 ± 1.0

Table 4.6: Percent differences in melting times of sample droplets with respect to pure water at different warm plate temperatures, with 95% confidence intervals based on a Student's *t*-distribution.

Sample	Percent Change in Melting Time Relative to Pure Water (%)						
	1 °C	2.5 °C	5 °C	7.5 °C	10 °C	20 °C	30 °C
50 ppm f-MWCNT	-3.9 ± 2.1	-2.1 ± 1.9	5.0 ± 1.4	15.1 ± 2.2	13.2 ± 2.4	16.0 ± 2.6	12.2 ± 3.2
50 ppm p-MWCNT	-1.6 ± 2.0	-2.6 ± 1.7	4.9 ± 1.3	13.6 ± 2.4	10.8 ± 2.3	14.5 ± 1.7	12.1 ± 3.1

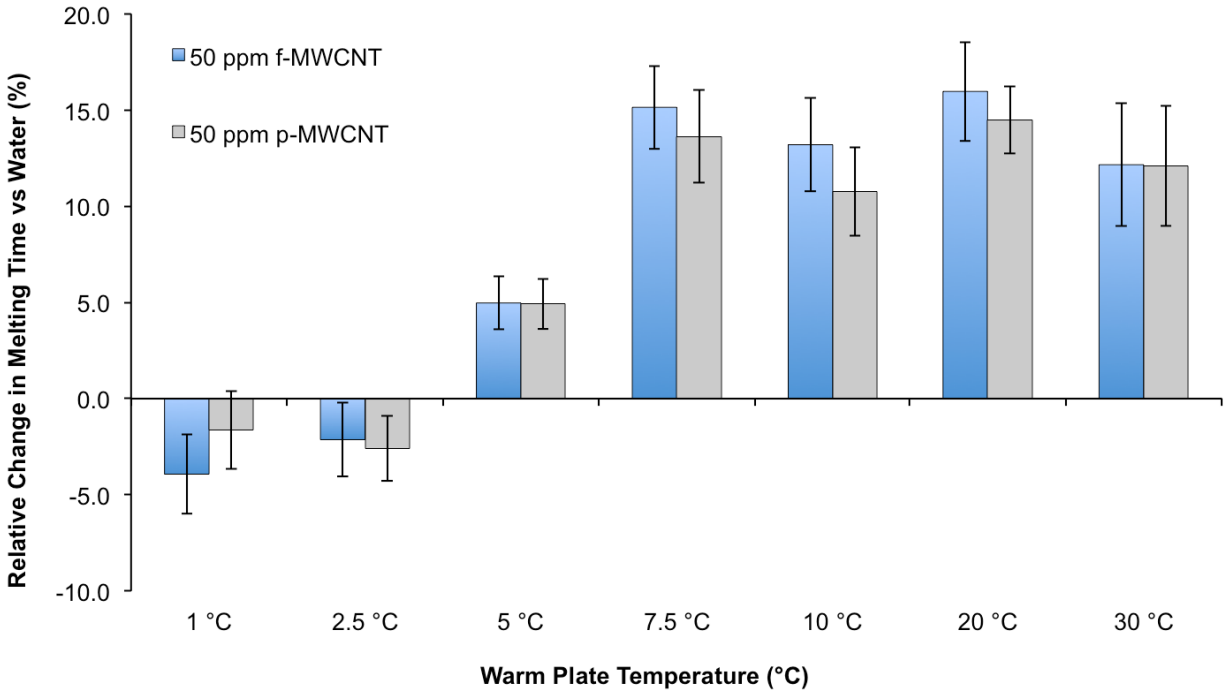

Figure 4.6: Relative change (%) in melting times of nanofluid droplets compared to pure water at different warm plate temperatures. Vertical error bars correspond to a 95% confidence interval based on a Student's *t*-distribution.

Table 4.5 shows that melting time decreases with an increase in temperature. Experiments were not conducted past 30 °C because the difference in melting times became marginal. The data suggest that at warm plate temperatures of 1 and 2.5 °C,

nanofluid droplet systems melted perhaps slightly more rapidly than the pure water systems, however the results lie nearly within experimental error of the baseline values. At 5 °C and above it is obvious that nanofluid droplets were slower to melt than pure water by about 10 – 15%, a seemingly consistent relative effect. The slight reduction at 1 and 2.5 °C could be due to enhanced conductive heat transfer in the liquid melt provided by the nanotubes. While the majority of the nanotubes are clustered, it is possible that their presence, along with the slight fraction remaining dispersed, could assist in heat transfer across the stagnant liquid layer that would marginally accelerate melting. Under convective regimes at 5 °C and above, the slower melting time of nanofluid droplets relative to pure water could be a function of the multitude of factors discussed in Section 4.5.2: the presence of clusters along the substrate and air/liquid interface could reduce the quality of the circulation rolls; their movement within the bulk fluid is likely opposed by drag forces; and possibly a slight improvement in thermal conductivity would oppose convection. Finally, no measureable difference was observed between pristine and functionalized MWCNT samples. This is likely a result of the freezing process and suggests that the effect of crystallization on clustering is the same for both MWCNT types and produces clusters of similar size (Ivall et al., 2015a). It is worth noting that the functionalized nanofluid systems melted faster at the 1 °C condition than their pristine counterparts, and slower in three of the five temperatures where convection occurred. While well within error, this could possibly be due to the functionalized nanofluids remaining slightly more dispersed during crystallization and after melting. Having more numerous and smaller clusters in the functionalized case could elicit a different behavior from the system.

While the degree and mechanism by which the MWCNT clusters may influence the convective regimes demand more characterization, these materials offer unique insight into the small scale fluid mechanics occurring within melting ice droplets exposed to thermal gradients. The use of surface-functionalized MWCNT nanofluid systems is also advantageous in that no surfactants are required that would undoubtedly suppress the surface tension gradients. In these droplet systems, the rapid microscale flows induce strong recirculation that significantly enhances the heat and momentum transport properties within the liquid system. Not only does this shed new light on the

fundamentals of droplet interactions with the natural and industrial environment, but the occurrence of autonomous and highly efficient mixing could also see technological uses in micro-fabrication applications.

4.6 Conclusions

Sessile frozen droplets composed of water or 50 ppm aqueous multiwall carbon nanotube (MWCNT) nanofluids were melted on a hydrophobic surface at temperatures between 1 and 30 °C. Convective cells developed in the liquid melt region contained between the ice and substrate at temperatures above 5 °C and convection was dependent on the presence of ice. Empirical and analytical results comparing surface tension to buoyancy forces support a thermocapillary-driven convection mechanism within the liquid at the specific temperatures and dimensions tested. Additionally, systems containing MWCNTs exhibited shorter melting times in conductive regimes yet longer melting times under convective regimes compared to pure water. New insights are gained into the melting characteristics of MWCNT nanofluid systems as well as into the transient and significant microscale fluid behaviors occurring within melting water droplets.

4.7 Acknowledgements

The authors are grateful to the Natural Sciences and Engineering Research Council of Canada (NSERC), the Fonds de recherche du Québec – Nature et Technologies (FRQNT), the McGill Faculty of Engineering (MEDA scholarship) and the McGill Department of Chemical Engineering (EUL) for financial support. The authors would also like to thank Adya Karthikeyan for surface tension and viscosity measurements of MWCNT samples.

Chapter 5

Quantitative Stability Analyses of Multiwall Carbon Nanotube Nanofluids Following Water/Ice Phase Change Cycling

5.1 Preface

With the phase change process being shown to largely result in the clustering of MWCNTs, the focus now turns to whether the dispersions can be restored to initial levels of stability. This one of the most important questions of this thesis as it underlies the feasibility of MWCNT-enhanced water-based phase change technologies. This chapter assesses the recoverability of MWCNT nanofluids after repeated phase change cycling and also elucidates whether phase change has an impact on the functionalities on the MWCNT surface.

5.2 Abstract

Multiwall carbon nanotube nanofluids are regularly investigated for phase change enhancement between liquid and solid states owing to their improved heat transfer properties. The potential applications are numerous, the most notable being latent heat thermal energy storage, but the success of all nanofluid-assisted technologies hinges greatly on the ability of nanoparticles to remain stably dispersed after repeated phase change cycles. In this report, the stability of aqueous nanofluids made from oxygen-functionalized multiwall carbon nanotubes (f-MWCNTs) was profiled over the course of 20 freeze/thaw cycles. Sonication was used after each cycle to re-disperse clusters formed from the crystallization process. This study offers a quantitative evaluation of f-MWCNT-nanofluid stability as a result of phase change through optical characterization of concentration and particle size. It also provides insight into the integrity of the surface functionalities through zeta potential and XPS analyses. Concentration and particle size measurements showed moderate and consistent recoverability of f-MWCNT dispersion following ultrasonication. XPS measurements of solid-state MWCNTs exposed to freeze/thaw cycling in water and zeta potential analyses of the nanofluids indicate that the surface oxygen content is preserved throughout phase change and over repeated cycles. These results suggest a resilience of oxygen-functionalized MWCNTs to the freezing and thawing of water, which is ideal for their utilization as phase change enhancers.

5.3 Introduction

The term “nano” is typically applied to materials measuring between 1–100 nm in at least one dimension. At these sub-micron scales, nanomaterial properties can deviate considerably from those observed at bulk proportions, giving rise to unique features such as enhancements in mechanical, thermal, catalytic and electronic properties (Cao, 2004). This phenomenon has opened up new avenues of research seeking to exploit these attributes to improve existing applications or to develop altogether novel technologies. Multiwall carbon nanotubes (MWCNTs) are a popular class of

nanomaterials owing to their exceptional properties and the unique architectures they can form (Dresselhaus et al., 2001). These tubular structures consist of concentrically rolled graphitic sheets, and the honeycombed binding of hybridized carbon atoms affords incredible mechanical strength to the materials (Iijima, 1991; Ajayan and Ebbesen, 1997). A common application of MWCNTs is the fabrication of composite materials whereby embedding MWCNTs into a base medium (solid or liquid) enhances the overall performance of the system in many respects (Ajayan et al., 2003). When dispersed in liquid media, MWCNT nanofluids exhibit broad-spectrum light absorption that is ideal for solar thermal energy collection (He et al., 2011; Hordy et al., 2014). MWCNT nanofluids are also widely recognized for augmented heat properties (Xie and Chen, 2011; Murshed and de Castro, 2014).

The performance of nanofluids relies heavily on maintaining a stable dispersion of individual nanoparticles (Choi and Eastman, 1995). While the extraordinarily high surface area of the nanoparticles often underlies the perceived enhancements, a caveat is that the accompanying high surface energies can lead to agglomeration and settling of the nanoparticles. Pristine (p-) MWCNTs are hydrophobic and the attractive van der Waals forces between them are quite strong. In polar solvents such as water and glycols, which are common working fluids, p-MWCNTs must be made compatible with such environments to be effective. In order to prevent agglomeration, chemical adjuvants – namely surfactants – can be added to the liquid that coat the p-MWCNTs and stabilize them in the solvent by electrostatic repulsion (Vaisman et al., 2006). Alternatively, the outer surfaces of the p-MWCNTs can be chemically functionalized with oxygen or nitrogen moieties (CO, COOH, OH, NH_X) that intrinsically promote interaction with the solvents (Taylor et al., 2013). In water, deprotonation of the carboxylic acid groups leads to the creation of an electrostatic double layer around the f-MWCNTS and the formation of a negatively charged surface (Hordy et al., 2013a). This stabilization mechanism is known as DLVO theory (Derjaguin and Landau, 1941; Verwey and Overbeek, 1948). Both dispersion techniques can deliver suspensions that are stable on the long-term (months to years), but some of the more significant advantages intrinsic to the use of surface-functionalized MWCNTs are that any secondary effects associated with the

additives are waived and the nanofluid system can typically withstand more rigorous operating conditions (Ghadimi et al., 2011).

The ability of MWCNTs to modify the properties of liquid and solid phases has been well established, and researchers are now evaluating their capacity to modify the conversion of systems between phases. Prime candidates for this feature are phase change materials (PCMs) used for latent heat thermal energy storage (LHTES). These systems take advantage of the high heat capacities of the base materials to absorb and release large amounts of energy with minimal changes in temperature (Hasnain, 1998). This helps shift energy consumption to off-peak hours and also improves energy efficiency due to the small temperature differences required. One of the inherent limitations of PCMs is that they tend to suffer from poor thermal conductivities. Since phase change is usually a heat transfer-limited process, the addition of nanomaterials accelerates the transition by increasing the overall heat transfer, and thus improves the efficiency of the process (Siegel, 1977). Water-based MWCNT nanofluids exhibit accelerated nucleation, enhanced rates of sensible cooling and crystallization, as well as increased conversion of liquid to solid in the freezing of liquid water to ice (Mo et al., 2011; Kumaresan et al., 2013; Chandrasekaran et al., 2014; Jia et al., 2014) and to gas hydrates (Pasieka et al., 2013b). These studies have clearly demonstrated the benefits of MWCNT addition on the freezing process, however very little focus has been placed on the stability of f-MWCNT nanofluids as a result of the phase change process. Most research chronicles the proceedings of a single phase change event, and few attempts have been made to assess the performance of a given f-MWCNT sample over multiple freeze/thaw cycles. In a previous study, the crystallization process was shown to result in clustering of f-MWCNTs, producing a destabilized nanofluid upon melting (Ivall et al., 2015a). This limitation of phase separation is often only generally commented on in the literature (Zeng et al., 2008; Wang et al., 2009). If water-based f-MWCNT nanofluids are to be considered for enhancing the conversion between liquid and solid phases for applications such as LHTES, or if the nanofluids encounter freezing environments, it is necessary to examine the effects of repeated freeze/thaw cycling on the characteristics of f-MWCNTs. These analyses will determine the degree to which nanofluid dispersions can be recovered and will help establish whether any associated clusters of f-MWCNTs

are reversible (agglomeration) or irreversible (aggregation) (Sokolov et al., 2015). This study sets out to profile the behaviors of aqueous nanofluids made from oxygen-functionalized MWCNTs over the course of twenty freeze/thaw cycles (with ultrasonication in between) using a combination of spectroscopic techniques. Together, these measurements provide deeper insight into the effects of a freeze/thaw cycle on the stability of f-MWCNTs, and contribute to a more holistic understanding regarding the feasibility of f-MWCNT nanofluids for phase change applications.

5.4 Experimental Method

5.4.1 MWCNT Synthesis and Nanofluid Preparation

Multiwall carbon nanotubes were grown by thermal chemical vapor deposition using an Ar/C_2H_2 gas mixture in a furnace at 700 °C, where argon is the carrier gas and acetylene is the carbon source. A stainless steel 316 mesh provides the catalytic support site for nanotube growth whereby the MWCNTs grow out of the substrate to form a forest. A portion of these pristine MWCNT meshes was subsequently treated with a low-pressure capacitively coupled radio-frequency (13.56 MHz) glow discharge plasma process using an $Ar/C_2H_6/O_2$ mixture. This treatment covalently grafts oxygen functionalities onto the exterior surface and renders the MWCNTs dispersible in polar solvents. To produce aqueous nanofluids, individual meshes containing either pristine (p-) or functionalized (f-) MWCNTs were placed into 6-dram borosilicate glass vials (Kimble-Chase) and covered with water (Fisher, Optima LC/MS, UHPLC-UV). The vials were agitated in an ultrasonication bath (Branson 2510R-MT, 42 kHz frequency) for 10 minutes to fracture the MWCNTs off the mesh and release them into solution (no material from the mesh is transferred to the fluid). The dispersed MWCNTs measure on average 1 μm in length and 31.4 nm in diameter. The full procedures and details for MWCNT synthesis and nanofluid preparation can be found in Baddour et al. (2009), Vandsburger et al. (2009), Hordy et al. (2013a) and references therein. For the current study, individual aqueous nanofluid samples were prepared from four meshes covered with p-MWCNTs and six meshes covered with f-MWCNTs to normalize batch effects (such as fluctuating oxygen

concentration on the f-MWCNT surface). Each nanofluid sample was then divided into two experimental replicates with volumes of approximately 7 mL.

5.4.2 Freeze/Thaw Cycling of MWCNT-Nanofluids and Meshes

The experimental schedule is provided in Table 5.1. The vials containing nanofluid samples were frozen overnight in a freezer set to -23°C. The samples were removed the following morning and left to thaw at room temperature. Once fully melted, the samples were sonicated for one hour. A 1 mL aliquot was taken from each sample for average particle size, zeta potential and concentration measurements. After these measurements, the aliquot was returned to the vial and the samples were placed in the freezer for a subsequent freeze/thaw cycle. The samples underwent the same procedure for 20 freeze/thaw cycles spanning a period of four weeks. Measurements were taken after every phase change cycle for the first 10 cycles, and then for cycles 15 and 20. At the end of the experimental period, four f-MWCNT sample vials were dried to atmosphere and the f-MWCNT powders were recovered for XPS analysis. Additionally, strips of individual meshes containing pristine and functionalized MWCNTs were placed in water and subjected to the same freeze/thaw cycling procedure, with the exception of sonicating, as this would remove the MWCNTs from the meshes. After 1 or 10 freeze/thaw cycles, the meshes were removed from the liquid and placed in a vacuum desiccator to remove all moisture. The composition of the meshes as a result of the freeze/thaw process was then analyzed through XPS.

5.4.3 Characterization

Concentration data were obtained using a dual-beam UV-Vis spectrophotometer (Thermo Scientific Evolution 300 PC, 190-1100 nm wavelength range). The samples were analyzed in poly(methyl methacrylate) (PMMA) cuvettes (300–750nm wavelength range, 10 mm path length). All UV-Vis measurements were performed at room temperature and pressure. Transmission readings were taken over a broad wavelength scan between 400 and 700 nm (1.0 nm step size) using pure water as a baseline. The transmission data were converted into concentration values using the Beer-Lambert law and the calibration curve developed by Hordy et al. (2014). Particle size (PS) and zeta potential (ZP) measurements were acquired using a Malvern Zetasizer (Nano ZS, 633 nm wavelength). Particle sizes were measured in the PMMA cuvettes described above (instrumental particle size range is 0.3 nm to 10 μm). Zeta potentials were measured using DTS1070 folded capillary cells with metal contact plates for temperature stabilization. Particle size was determined through dynamic light scattering and the Stokes-Einstein equation, and zeta potential was determined through laser Doppler velocimetry and the Henry equation (with the Smoluchowski approximation). The ZetaSizer software performed the calculations for both PS and ZP using the properties of water as the dispersant (refractive index = 1.33, dynamic viscosity = 0.8872 cP, dielectric constant = 78.5) and the refractive index of graphene for MWCNTs (assumed to be 2.5) (Weber et al., 2010; Cheon et al., 2014). Measurements were performed at 25 °C at the natural pH (~5.8) and ionic strength of the samples. For particle size and zeta potential measurements, the instrument uses an autocorrelation function to formulate a reading, and an average of three readings is used. Compositional analyses of MWCNT surfaces were performed using a Thermo Scientific K-Alpha X-ray Photoelectron Spectrometer (XPS) system. Samples were irradiated with a monochromated Al-Kα photon source (hν = 1486.6 eV) in conjunction with an electron flood gun for charge compensation. Three analysis areas were selected per sample (200 μm spot size). Survey spectra (200 eV pass energy, 1 eV step size, 10 ms dwell time) and high-resolution carbon and oxygen spectra (50 eV pass energy, 0.5 eV step size, 50 ms dwell time) were acquired over 5 to 10 passes. The survey spectra were processed with the Thermo

Scientific Avantage software using the automatic survey ID function that provides the surface composition to within 0.1 at %.

5.5 Results and Discussion

5.5.1 Stability of MWCNT Nanofluids over Freeze/Thaw Cycling

The stability of aqueous nanofluids containing f-MWCNTs was profiled over the course of 20 freeze/thaw cycles, corresponding to a period of one month. The schedule was designed to roughly mimic a typical daily freeze/thaw cycle for LHTES applications (as well as allowing for the various measurements to be performed – the melting process would likely take longer) and is presented in Table 5.1. Six samples were tested with concentrations between 15 and 91 ppm, at two replicates per sample. p-MWCNT samples were not tested as they immediately agglomerated upon dispersion in water and were incapable of forming a stable nanofluid. The initial stock nanofluids exhibited the uniformly black appearance of homogeneous suspensions. The freezing process results in clustering of the f-MWCNTs due to the rejection of particles from the solidifying ice lattice (Ivall et al., 2015a). Upon melting, the liquid samples contained visible clusters and the liquids were comparatively lighter in colour than their initial stock concentrations (Ivall et al., 2016b). Sonication was then used in an attempt to break apart the clusters and recover dispersion of individual nanotubes. Examples of an initial, frozen and sonicated sample containing f-MWCNTs, as well a nanofluid samples containing p-MWCNTs, are shown in Figure 5.1. Since the amount of f-MWCNTs remaining in solution is correlated to light absorption, concentration analyses through UV-Vis spectroscopy provide a measure of this recovery and of the overall stability of the nanofluids. The recovery can be best gauged by the concentration of the solutions relative to their initial stock concentration, calculated using Equation 5.1. Table 5.2 and Figure 5.2 show the average degree of recovery of all samples in terms of concentration relative to their initial stock concentration, along with 95% confidence intervals using a t-distribution, over the course of phase change cycling. These measurements were taken

approximately 3 hours after sonication, at which point most of the larger clusters had settled. Care was taken to extract aliquots of the supernatant containing only the fraction of nanotubes remaining in suspension.

Table 5.1: Experimental schedule.

Time	Procedure
9:00 – 10:30	Samples removed from freezer and thawed
10:30 – 11:30	Samples sonicated
11:30 – 14:00	Particle size measurements
14:30 – 15:30	Zeta potential and UV-Vis measurements
16:00	Samples placed in freezer and left overnight

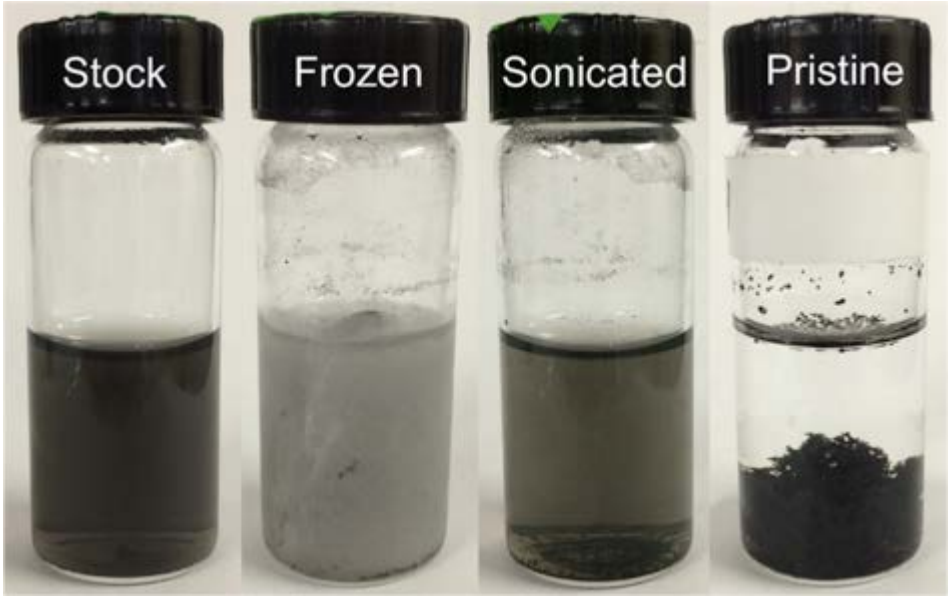

Figure 5.1: Visual appearance of (a) as-produced, (b) frozen, and (c) sonicated f-MWCNT nanofluid samples, as well as (d) a sample containing p-MWCNTs.

$$\text{Relative Concentration} = \frac{C_{\text{cycle "n"}}}{C_{\text{stock}}} \qquad \text{Equation 5.1}$$

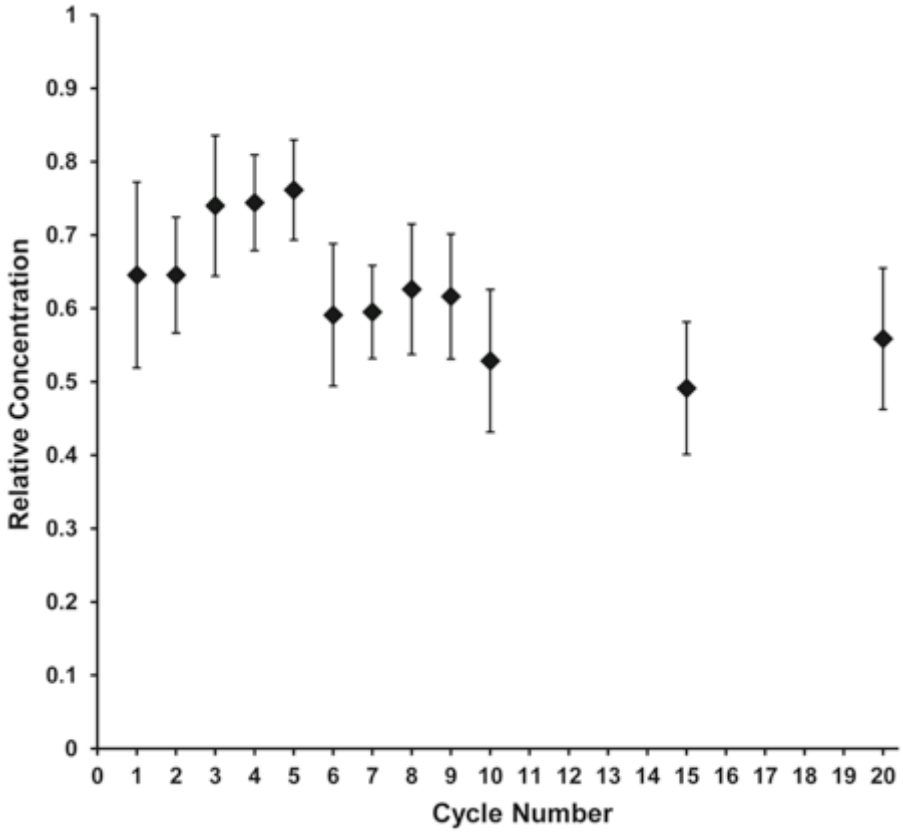

Figure 5.2: Average relative concentrations of f-MWCNT nanofluids (compared to initial stock concentration) over phase change cycling. Vertical error bars correspond to 95% confidence intervals.

The average recovery of the nanofluids varied widely but typically ranged between 50 to 75%. Note that these fractions are relative to the initial stock concentration, and not to the concentration of previous samples. The variable degree of recovery within a given cycle is likely due to different networks of clusters formed through different freezing patterns, the varying success of sonication, differences in nanotube characteristics, or contaminants affecting f-MWCNT stability. There may be a slight trend that suggests an overall decrease in recovery with time, however the large variability in the data makes a regression analysis difficult. Perhaps the most notable aspect of Figure 5.2 is the sharp initial drop in relative concentration following the first phase change cycle (15-35%), after which the degree of recovery seems to level off over the long run between 50 and 60%. This occurrence may point to a purification step whereby the general clustering of nanotubes during phase change removes a certain portion of f-MWCNTs that are less

compatible with the liquid solvent, possibly from acquiring less oxygen during the functionalization process (Section 5.5.2 explores this concept in further detail). The strong attractive forces between more hydrophobic nanotubes could oppose redispersion in the solvent during sonication. Accounting for the initial reduction in concentration, these results show that the nanotubes can be continuously redispersed after phase change cycling, albeit at a lower concentration (~ 55%). A gradual reduction in concentration would not be surprising, however, as the accumulation of unseparated clusters would decrease the fraction of individual nanotubes in the liquid. Hordy et al. (2014) reported a 5% decrease per month in concentration for undisturbed samples of the current aqueous f-MWCNT nanofluid system, and the issue of long-term nanofluid stability is the subject of myriad studies (Lamas et al., 2012; Teng et al., 2014). Ryglowski et al. (2010) also reported the breakdown of surfactant-treated carbon nanotube nanofluids (CNT) during phase change cycling using electrical resistance testing as a metric for stability and carbon nanotube loadings 1 to 2 orders of magnitude greater than those in the current study. The onset of agglomeration was detected at cycle 3, and complete destabilization was observed by cycle 12. Ultrasonication was used at cycle 12 and was similarly shown to be effective in restoring resistance values to initial levels.

Concentration analyses paint a temporary and global snapshot of nanofluid suspensions, but particle size provides a more specific insight into the overall prognosis of colloidal stability. In conjunction with the concentration data, particle size and polydispersity indices (PDI) of the nanofluid samples are also reported. Table 5.3 and Figure 5.3 show the average particle sizes and PDI of the nanofluids after sonication, along with a 95% confidence interval based on a t-distribution. The particle size corresponds to the intensity-averaged (Z-average) diameter of a particle in suspension moving through Brownian motion. These measurements were performed on the same samples taken for concentration measurements and also correspond to aliquots of the supernatant containing only the fraction of nanotubes remaining in suspension.

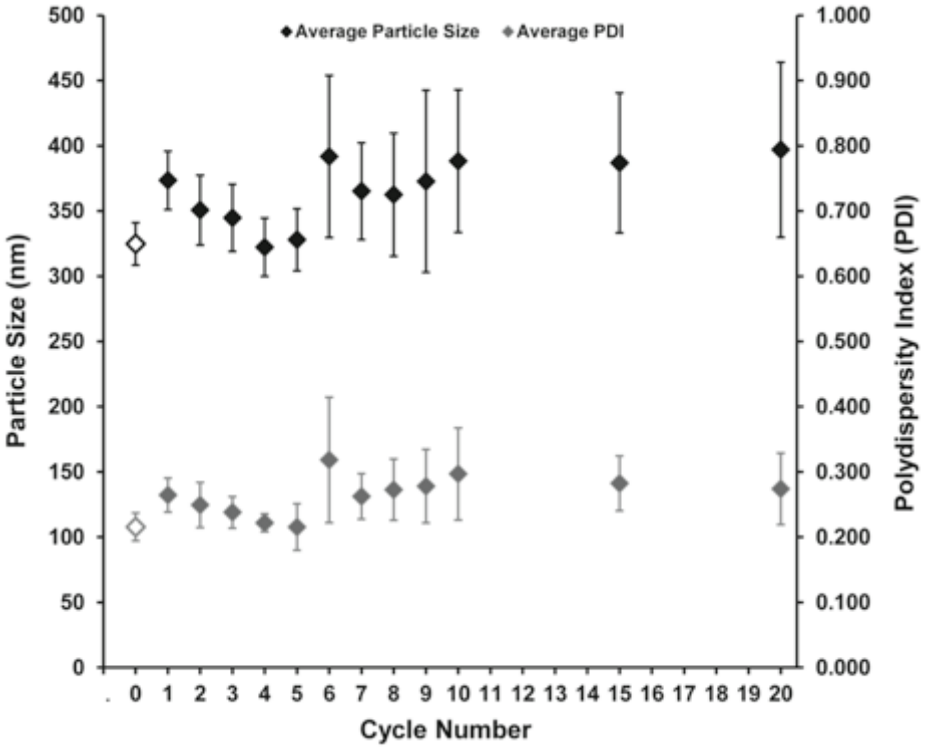

Figure 5.3: Average particle sizes (black) and polydispersity indices (grey) of f-MWCNT nanofluids over phase change cycling. Vertical error bars correspond to 95 % confidence intervals. Hollow diamonds correspond to values of initial stock samples.

The average particle size of the stock nanofluid samples made from f-MWCNTs was 325 nm with a PDI of 0.22. DLS calculates an effective hydrodynamic diameter for a particle assuming the motion of a sphere. Owing to the high aspect ratio of carbon nanotubes, the value interpreted by the software will range between the diameter (~ 30 nm) and length (~1 μm) of the produced nanotubes. Smith et al. (2009a) and Cheng et al. (2011) obtained particle sizes on the order of 150–200 nm with MWCNTs measuring approximately 25 nm in diameter and 0.5 μm in length. A value of 325 nm for the current nanotubes is thus a reasonable value considering the larger diameter and length. A PDI of 0.22 indicates a fair homogeneity in particle size (where 0 is perfectly uniform and 1 is entirely non-uniform), and this value is consistent with results obtained from manufacturer-supplied MWCNTs (Bouchard et al., 2015). Figure 5.3 shows that the average particle size remained relatively similar to the initial value for the first 5 cycles, at which point it began to diverge somewhat substantially. Similar to the concentration

data presented in Figure 5.2, the particle size seemed to plateau around 380 nm after cycle 5, which corresponds to an approximate 17% increase compared to the stock value. The larger size was accompanied by a wider spread in particle size and a slight increase in PDI. The particle size analyzer also showed a more weighted contribution of peaks in the micron scale at these cycles. These findings all point to the presence of clustering in the supernatant. This underscores why concentration is only a broad diagnostic of nanofluid stability, since the smaller the cluster, the slower the settling velocity, and a nanofluid may not actually be stable despite what its apparent concentration suggests (Stokes, 1851). A mapping of the correlation between relative particle size and relative concentration can be seen in Figure 5.4, which presents all of the data points acquired over all cycles. As expected, a correlation exists between the two variables. The clustering of nanotubes decreases the surface area of absorbing components, leading to a reduced observed concentration. Relative particle sizes below unity are likely a result of sampling aliquots of the supernatant that contain a higher fraction of relatively smaller particles than the bulk average. Particle size analyses thus serve as a rapid and more effective assessment of the quality of dispersions. It helps to resolve the question as to whether this absorption is a result of a large amount of clusters or a smaller amount of well-dispersed nanotubes. In the current case, the concentration and particle size data suggest that nanofluids made from f-MWCNTs experienced an initial reduction in number of dispersible components, but the remaining fraction was resilient to phase change cycling after undergoing sonication to disentangle agglomerates and restore nanofluid dispersion. In order to probe deeper into the nature of the clustering processes taking place, zeta potential and XPS measurements were conducted to inspect the condition of the surface functionalities.

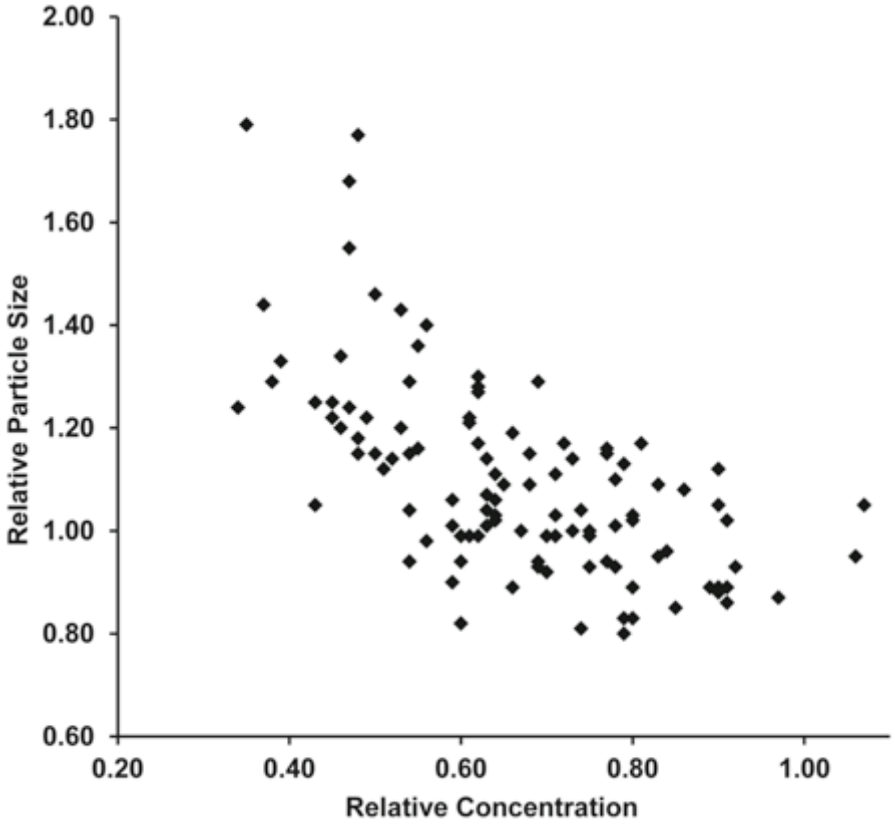

Figure 5.4: Mapping of the correlation between relative concentration and relative particle size of f-MWCNT nanofluids after sonication following phase change cycling. Both terms are relative to initial stock values.

Table 5.2: Average relative concentrations of f-MWCNT nanofluids (compared to initial stock concentrations) over phase change cycling, with 95% confidence intervals.

Cycle	1	2	3	4	5	6	7	8	9	10	15	20
Rel. Conc.	0.65 ± 0.13	0.65 ± 0.08	0.74 ± 0.10	0.74 ± 0.07	0.76 ± 0.07	0.59 ± 0.10	0.59 ± 0.06	0.63 ± 0.09	0.62 ± 0.09	0.53 ± 0.10	0.49 ± 0.09	0.56 ± 0.10

Table 5.3: Average particle sizes (PS) and polydispersity indices (PDI) of f-MWCNT nanofluids over phase change cycling, with 95% confidence intervals.

Cycle	Stock	1	2	3	4	5	6	7	8	9	10	15	20
PS	325 ± 16	374 ± 22	351 ± 27	345 ± 26	322 ± 22	328 ± 24	392 ± 62	365 ± 37	363 ± 47	373 ± 70	388 ± 55	387 ± 54	397 ± 67
PDI	0.22 ± 0.02	0.26 ± 0.03	0.25 ± 0.03	0.24 ± 0.02	0.22 ± 0.01	0.22 ± 0.04	0.32 ± 0.10	0.26 ± 0.03	0.27 ± 0.05	0.28 ± 0.06	0.30 ± 0.07	0.28 ± 0.04	0.27 ± 0.05

Table 5.4: Average zeta potential (ZP) of f-MWCNT nanofluids over phase change cycling, with 95 % confidence intervals.

Cycle	Stock	1	2	3	4	5	6	7	8	9	10	15	20
ZP	-48.8 ± 1.2	-46.7 ± 1.6	-47.3 ± 0.9	-46.4 ± 2.8	-45.8 ± 2.8	-45.7 ± 2.9	-43.7 ± 2.5	-43.9 ± 3.0	-43.3 ± 3.1	-42.1 ± 3.5	-41.4 ± 3.5	-40.3 ± 2.9	-38.1 ± 2.7

5.5.2 Characterization of Surface Oxygen Content

The surface oxygen content of MWCNTs over the course of repeated freeze/thaw cycling was examined through XPS and zeta potential analyses. XPS provides a direct measure of the chemical composition of the nanotube surfaces while zeta potential serves as a general indication of colloidal stability. For XPS analysis, meshes containing pristine or functionalized MWCNTs were placed in water and subjected to 1 or 10 phase change cycles to assess the short and long-term stability of the oxygen-containing groups. Sonication was not applied at any point in this test, as the nanotubes would be removed from the mesh. Three different meshes were assayed per type of nanotube and phase change cycles. The oxygen content of the meshes prior to and after 1 or 10 phase change cycles are reported in Table 5.5 and represent the average of three different spots on a given mesh (with a 95% confidence level based on a z-distribution). These compositions are calculated from survey spectra data (example spectra shown in Figure C1). Note that the balance of the surface content is attributed to carbon, as the spectra exhibited only trace amounts of impurities (< 0.5 at.%).

Table 5.5: Oxygen content of meshes containing either pristine (p-) or oxygen-functionalized (f-) MWCNTs prior to and after phase change cycling in water.

1 cycle			10 cycles		
Sample	As-produced at.% O	Post-thaw at.% O	Sample	As-produced at.% O	Post-thaw at.% O
f-1	5.5 ± 0.4	5.8 ± 0.2	f-4	6.1 ± 0.2	6.0 ± 0.3
f-2	11.7 ± 0.4	11.5 ± 1.0	f-5	6.7 ± 0.7	5.5 ± 0.2
f-3	7.0 ± 0.6	6.6 ± 0.4	f-6	7.0 ± 0.0	6.4 ± 1.0
p-1	3.3 ± 0.5	2.8 ± 0.5	p-4	1.7 ± 0.2	1.7 ± 0.3
p-2	1.8 ± 0.2	1.3 ± 1.6	p-5	4.1 ± 0.2	4.9 ± 0.3
p-3	1.2 ± 0.8	0.6 ± 0.8	p-6	2.1 ± 0.2	2.4 ± 0.8

The XPS data indicate that the phase change process has no effect on the composition of the nanotubes. All twelve samples exhibited changes that were mostly within the margin of error. The overall lower content of oxygen explains why pristine MWCNTs agglomerate rapidly in solution. This contrast in behaviors toward water was also observed for the meshes themselves. Meshes covered with pristine nanotubes would not submerge in water (Figures 5.5a and 5.5b), while meshes covered with functionalized nanotubes easily entered the liquid and remained submerged during freezing (Figures 5.5c and 5.5d). These hydrophobic or hydrophilic attributes were maintained over the course of the phase change cycling. The large confidence intervals associated with some composition values, especially the p-MWCNT-covered meshes, arise from a large variance between different regions on a given mesh (e.g. from 0 to 3.8 at.% on P-2). Half of the p-MWCNT-covered meshes contained at least one region with 0 at.% oxygen, and the small amount of oxygen found on other regions results from contamination during the production process. Typical values for p-MWCNTs are below 2 at.% (Smith et al., 2009b; Hordy et al., 2013a). The variability in oxygenation on a given mesh could account for the sharp concentration drop observed for the dispersed f-MWCNTs after the first phase change cycle. If certain regions of a mesh acquire less oxygen during processing (which could be due to different flow fields inside the chamber, for instance), then nanotubes formed on these sections would be comparatively less stable. Once dispersed as a nanofluid, the phase change process could then accelerate the association of the hydrophobic nanotube fraction due to the accumulation of nanotubes outside of the solid phase.

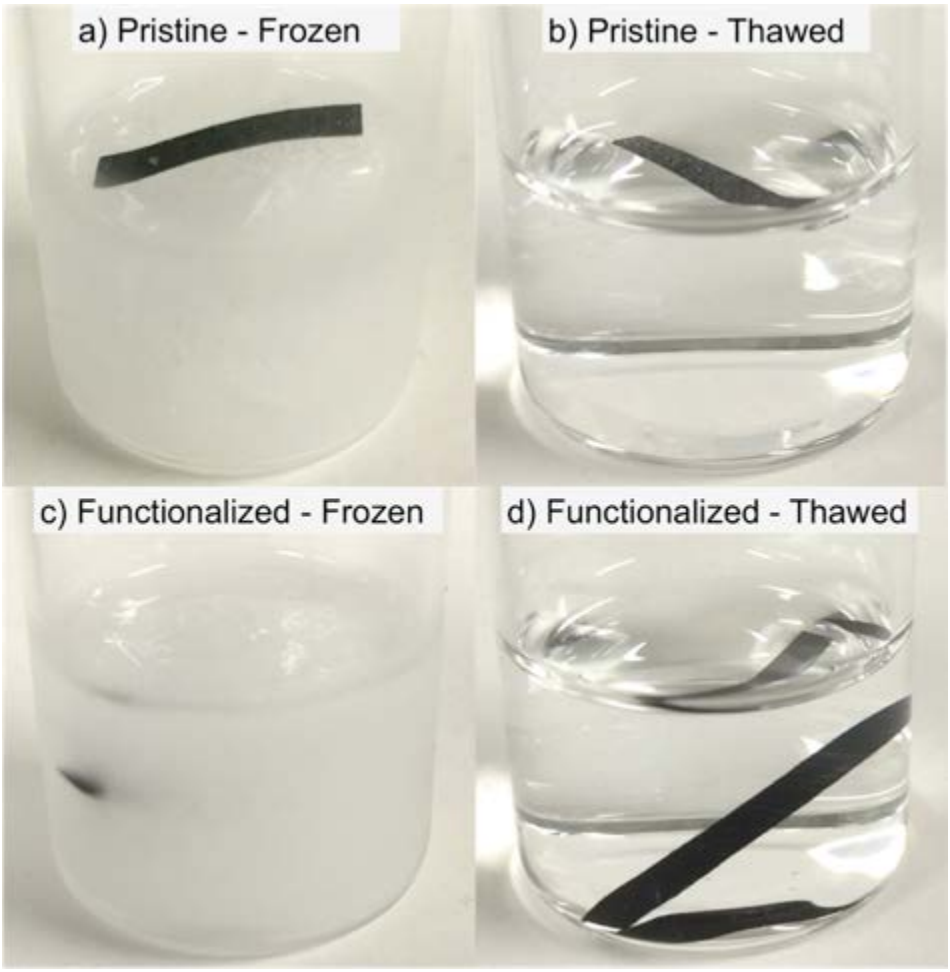

Figure 5.5: Behavior of meshes covered with pristine or oxygen-functionalized MWCNTs in water after 10 phase change cycles.

An indirect means to characterize the integrity of the oxygen functionalities while in suspension is the use of zeta potential. When dispersed in water at pH ~5.8, deprotonation of the carboxylic acid gives the f-MWCNTs a negative surface charge that leads to the formation of an electrostatic double layer within the liquid and stabilization through a DLVO mechanism (Shieh et al., 2007; Smith et al., 2009b; Hordy et al., 2013a). Zeta potential measurements denote the potential difference between this layer and a point in the bulk fluid. For two-phase systems such as nanofluids, the larger the magnitude of the potential difference (in absolute terms), the greater the colloid is electrically stabilized within the solvent. Literature values for the stability zones of colloids typically designate regions between 0 and 25 mV as unstable, 25 to 40 mV as

moderate stability, 40 to 60 mV as good or favorable, and over 60 as excellent (Yu and Xie, 2012; Teng et al., 2014). The zeta potentials of the f-MWCNT nanofluid samples are presented in Table 5.4 and Figure 5.6. p-MWCNT samples could not be tested due to complete agglomeration.

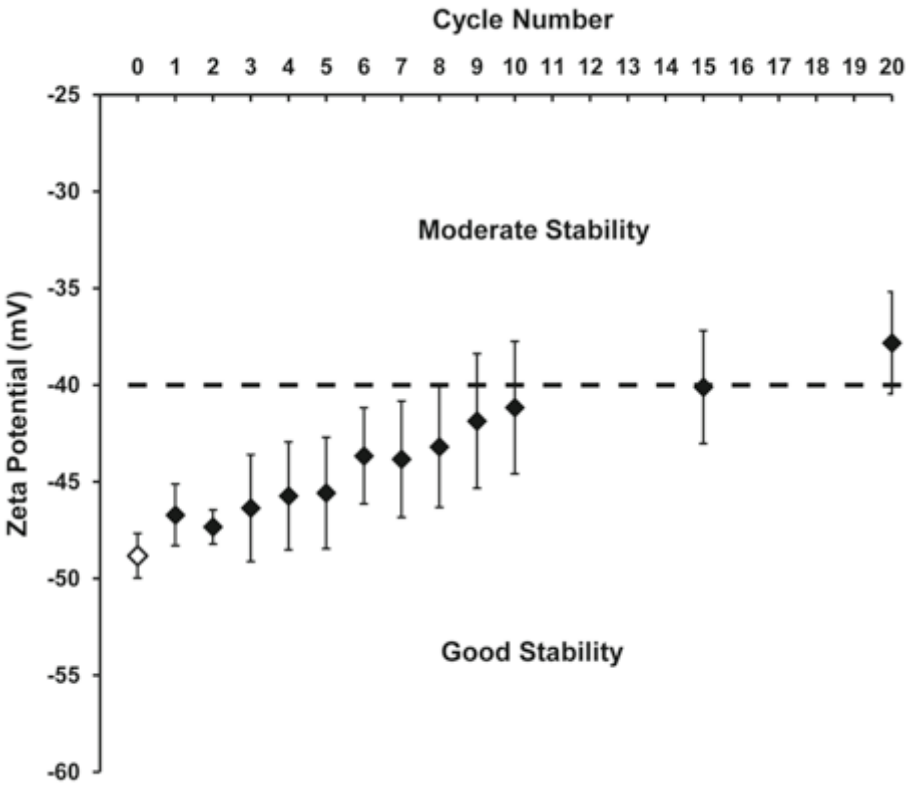

Figure 5.6: Average zeta potential of f-MWCNT nanofluids over phase change cycling. Vertical error bars correspond to 95% confidence intervals. Hollow diamond corresponds to initial stock samples. The dashed horizontal line at -40 mV is a common threshold that divides moderate and good stability.

The zeta potentials of the stock solutions prior to freezing ranged from -45.6 to -51.9 mV with an average of -48.8 mV at a pH of ~5.8. These values are consistent with those reported previously by Vandsburger et al. (2009) (-40.3 mV) and Hordy et al. (2013a) (-39.3 to -49.0 mV) and connote good stability. Zeta potentials reported by other groups for oxidized MWCNTs in water at this pH also fall within this range (Kim et al., 2003; Xie et al., 2003; Cheng et al., 2011). Over the course of freeze/thaw cycling, the average zeta potential slowly increased to a more positive value and the spread of the data

widened as well. Considering that the XPS results indicate that the surface functionalities remain intact, and the nanofluids appeared stable, this gradual drift is likely a result of steady contamination. Some minor contamination due to sample handling is possible, although the samples were not opened between cycles 10 and 15 and between cycles 15 and 20, yet they still demonstrated increases in zeta potential. The source of this increase can probably be explained by the results from XPS analyses on the f-MWCNT powders retrieved from dried nanofluid dispersions. Four of the twelve samples were chosen to analyze the powders by XPS. Figure 5.7 shows a typical survey spectra for one of the f-MWCNT meshes subjected to ten freeze/thaw cycles (f-5, in this case) and for one of the f-MWCNT nanofluids subjected to twenty freeze/thaw/sonication cycles. The survey spectra show similar peaks at carbon (C1s at 285.0 eV) and oxygen (O1s at 531.8 eV), and indicate a large content of silicon, sodium and calcium in the nanofluid samples. Silicon has peaks at 100.1 (Si2p), 103.0 (SiO_2), 103.5 (SiO_2-nH_2O $_2$) and 150.5 (Si2s) eV. Sodium has peaks at 63.3 (Na2s), 1072.0 (Na1s) and 1071.8 (Na_2O-SiO_2) eV, as well as an Auger peak at 497.4 eV. Calcium has peaks at 346.6 (Ca2p) and 347.1 (CaO) eV. Table 5.6 shows the average composition of the samples in terms of carbon, oxygen, silicon, sodium and calcium obtained from these survey spectra. Silicon is present in every case, while sodium and calcium are present in three of four cases. This alludes to the leaching of glass components into the liquid, as this type of borosilicate (Type 1, Class B) normally has a chemical makeup of 73% SiO_2, 10 % B_2O_3, 7% Al_2O_3, 6% Na_2O, 0-2% BaO, 1% CaO, and 1% K_2O (ASTM International, 2011). Comparison of Tables 5.5 and 5.6 shows that the presence of the impurities increases the oxygen fraction significantly. Owing to its stability, silicon would be found in water as silicon dioxide (SiO_2) (Bunker, 1994). Sodium and calcium would be found as free ions due to the ionic bonding they form as Na_2O and CaO. The leaching of soluble alkali and alkaline cations, most notably sodium, from borosilicate glass intro ultrapure water is known to be an issue with borosilicate glass (Griscom et al., 1994; Ledieu et al., 2004). In such cases, dissolved cations would migrate toward the anionic f-MWCNT surface. The ensuing neutralization of charges would translate into an increase in zeta potential values toward neutrality due to a reduced electrophoretic mobility of colloids under an applied electric field, consistent with DLVO theory. Despite this drift, the system remained in the realm of good stability until cycle 15.

Further, charge neutralization would also suppress the shielding necessary for electrostatic repulsion and lead to clustering, which may partly account for the expanded variability in the long-term concentration and particle size data described in Section 3.1. Smith et al. (2009a); Smith et al. (2009b) evaluated the impact of NaCl electrolyte addition on the stability of aqueous oxidized MWCNT nanofluids and equally found that increasing the concentration of sodium cations led to destabilized nanofluids. For these reasons, the ionic strength and pH of the solution in the present study were not adjusted since the presence of salts would interfere with the electrostatic double layer and the stability of the nanofluid. The presence of silicon, sodium and calcium were not observed on the meshes, likely because the samples did not undergo sonication, which enhances mixing and thus the leaching effect. Note that these relatively short sonication times should have no effect on oxygen content (Smith et al., 2009b). However, if the gradual degradation of zeta potential is attributable to the leaching of cations, this indirectly suggests the preservation of functional groups. Unfortunately, the contribution of oxygen from silicon and other contaminants makes an explicit determination of oxygen content on the recovered f-MWCNT powders impossible through XPS.

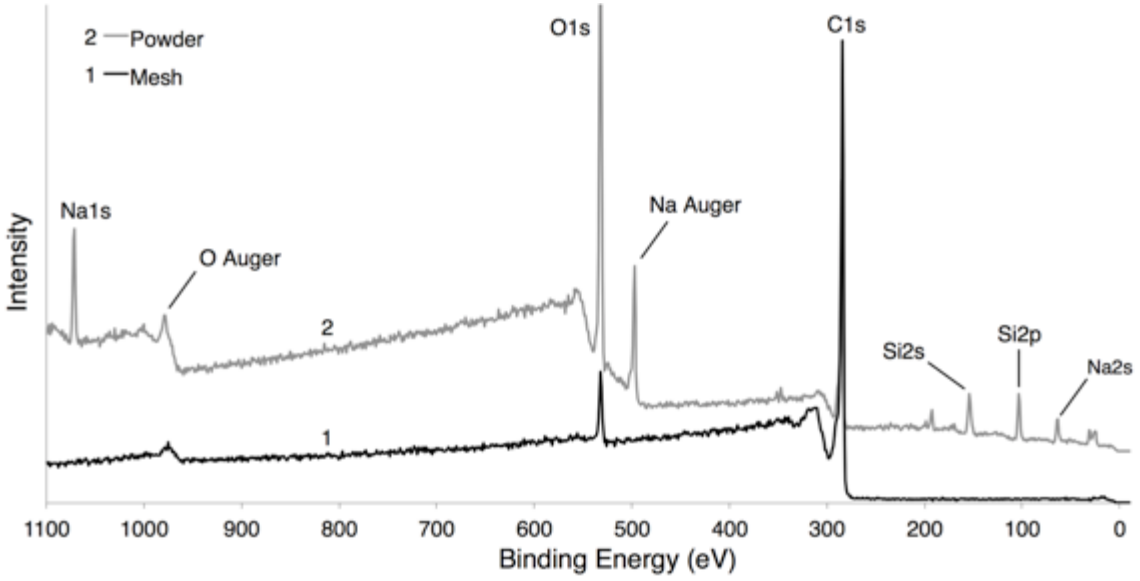

Figure 5.7: Sample XPS survey spectra for (1) f-MWCNT powders recovered from nanofluids after undergoing 20 freeze/thaw/sonication cycles and (2) f-MWCNT meshes after undergoing 10 freeze/thaw cycles.

Table 5.6: Composition of f-MWCNT powders retrieved from nanofluids subjected to twenty freeze/thaw/sonication cycles.

Sample	at.% C	at.% O	at.% Si	at.% Na	at.% Ca
1	70.9	21.1	8.0	0	0
2	44.5	39.2	10.6	4.2	1.6
3	46.5	37.8	10.2	4.3	1.1
4	55.9	34.4	3.7	4.6	1.4

The collective results in this study advocate that the phase change process likely has no effect on the surface functionalities of the f-MWCNTs. This is not unexpected, as temperature cycling between 25 and -18 °C would be unlikely to induce a chemical reaction. The compressive forces arising from the expansion of water during crystallization would also not compromise the integrity of the functional groups. Lastly, the ability to redisperse a relatively constant fraction of the nanotubes after each phase change cycle signifies that the clustering between f-MWCNTs is reversible to some extent, as particle sizes are slightly greater than initial values. This case of reversible association, i.e. agglomeration, would likely be caused by the accumulation of nanotubes excluded from the growing crystal lattice during solidification (Ivall et al., 2015a). Upon melting, the preservation of oxygen groups would permit re-establishment of electrostatic repulsion between f-MWCNTs, and would facilitate the disentanglement of intertwined nanotubes through ultrasonic vibration. The fraction of clusters that are not successfully broken apart could be a result of three causes. As mentioned, it is possible that a portion of nanotubes receiving less oxygen during plasma treatment could be removed by the freezing process. Their behavior would resemble pristine MWCNTs in character and be prone to van der Waals attraction that leads to agglomeration. It is also likely that severely intertwined clusters of suitably oxidized f-MWCNTs might require more powerful or direct sonication processes (such as a probe sonicator) to be disentangled (Amrollahi et al., 2008). Finally, the gradual neutralization of leached cations on the f-MWCNT surface could promote clustering of the strands. This leaching phenomenon is an issue for global and long-term f-MWCNT nanofluid stability if borosilicate glass is used as the storage vessel. However, the moderate recoverability of

f-MWCNT nanofluids after repeated cycling shows promise for their use as enhancers for freeze/thaw phase change cycling.

5.6 Conclusions

The effect of repeated freezing and thawing on the stability of water-based nanofluids containing plasma-functionalized multiwall carbon nanotubes was monitored quantitatively using several spectroscopic techniques. Nanofluids of various f-MWCNT loadings were subjected to 20 phase change cycles and sonication was employed after each cycle to redisperse the nanotube clusters formed during solidification. Concentration analyses showed that the phase change process removed a certain portion of nanotubes after the first cycle, but the retained fraction was recovered consistently across subsequent cycles. The surface oxygen content of both pristine and functionalized MWCNTs was verified directly through XPS measurements and was found to be unchanged after phase change cycling. The localized variance in oxygen content on meshes covered with f-MWCNTs results in a fraction of relatively more hydrophobic nanotubes that could agglomerate when dispersed in the liquid. This likely explains the initial concentration drop after the first phase change cycle, which may act as a purification step. Zeta potential measurements provided an indirect assessment of the presence of oxygen groups on the f-MWCNT surface and generally supported the XPS data. The moderately negative zeta potentials indicated the presence of negatively charged surface groups. We attribute the slow but steady neutralization of charge over the course of subsequent phase change cycles to the desorption of sodium cations from borosilicate glass. This theory should be tested using a different type of sample vial. Finally, particle size measurements showed slightly larger MWCNT sizes compared to initial levels, but this increase leveled off after the fifth cycle. This indicates that sonication is an effective means for reversing agglomeration of f-MWCNTs caused by freezing.

5.7 Acknowledgements

This work was financially supported by funding from the Natural Sciences and Engineering Research Council of Canada (NSERC), the Fonds de recherche du Québec – Nature et technologies (FRQNT), as well as the Faculty of Engineering and the Department of Chemical Engineering at McGill University. The authors would like to thank Maria Elena Corella Puertas and Jean-Sébastien Renault-Crispo for synthesis of the MWCNT samples, as well as Andrew Golsztajn, Ranjan Roy and Larissa Jorge for technical assistance.

Chapter 6

Thesis Conclusion and Future Work Recommendations

6.1 Comprehensive Conclusion

The current work investigates the liquid/solid phase change behavior of oxygen-functionalized multiwall carbon nanotube nanofluids. Chapter 3 demonstrated that dispersing f-MWCNTs into the ice phase would require very high freezing rates (at temperatures that are no longer industrially-relevant) and accordingly elevated levels of supercooling. If these conditions are not met, the exclusion of f-MWCNTs from the ice matrix causes severe clustering if the system is fully solidified. This reality is consistent with the precepts of the solidification of colloidal suspensions and is a fundamental consequence of the nano-scale features of f-MWCNTs. These results highlight important considerations for applications seeking to use nanomaterials to reduce the driving force required for solidification, as lower levels of supercooling lead to a higher extent of particle rejection. It follows then that the material properties of nanomaterial-enhanced solids are dependent on the freezing rate applied. Chapter 4 then examined the melting of the frozen sessile ice droplets containing MWCNTs. The presence of clustered MWCNTs revealed the occurrence of intense convective cells in the melt region between the substrate and floating ice. Through careful examination this convective motion was also observed in the melting of pure water droplets, and to the best of the author's knowledge, this is the first report of such a phenomenon. The mechanism driving convection was established to be thermocapillary in nature as temperature-derived surface tension gradients were created along the air/liquid interface between the ice and heated substrate. The presence of MWCNT clusters was found to increase both the

temperature required for the onset of convection and the melting time compared to pure water samples. This effect is ascribed to the suppression of surface tension forces due to the presence of foreign particles along the interface. On a broader level, the discovery of small-scale convection within water droplets is important for natural and industrial scenarios, as droplets are a ubiquitous occurrence. Chapter 5 probed into the nature of the clustering interactions caused by solidification and assessed the long-term viability of f-MWCNT nanofluids through phase change cycling. Results showed that the surface oxygen content of the f-MWCNTs was preserved after repeated freezing and thawing experiments, which suggests that the agglomeration of clusters during freezing is a reversible process. Sonication of nanofluids after melting was found to consistently restore concentrations to approximately 55 % compared to initial levels, with particle sizes on average 17 % greater than initial levels. This recoverability also suggests a reversible process, provided that sufficient energy can be supplied to break apart the agglomerates, and that no contamination is occurring that may destabilize the f-MWCNTs. In sum, the current work into the freeze/thaw cycling of aqueous f-MWCNT nanofluids provides a more holistic understanding of the relationship between phase change and nanofluid stability, and offers an encouraging prospective for f-MWCNT-enhanced phase change technologies.

6.2 Future Work Recommendations

The current work provides a foundation to understanding the impacts of liquid/solid phase change on MWCNT nanofluid stability. The following avenues could be pursued in order to probe deeper into the observed phenomena and provide a greater knowledge of the respective processes, which is important for the realization of MWCNT-assisted phase change applications:

- Parametric studies of MWCNT dispersion into the ice matrix examining the role of concentration, sample volume, other temperature driving forces, the addition of surfactants, and different nanotube characteristics.

- Characterizing the specific functional groups after phase change cycling using other spectroscopic tools such as FT-IR, Raman, AFM, and TGA.

- Studying the freezing and melting behavior of MWCNT nanofluids in gas hydrate systems (crystallized to full conversion), with a focus on MWCNT stability.

- Studying conductive/convective melting phenomena in gas hydrate systems.

- Modeling of the liquid-phase convection within the melting ice droplet and use of an infrared camera and more advanced particle tracking system.

- Further investigations into container leaching effects.

Other Significant Contributions

In addition to the work presented in this thesis, the following significant contributions were made during the research project:

- Ivall, J.; Pasieka, J.; Posteraro, D.; Servio, P. 2015. Profiling the concentration of the kinetic inhibitor polyvinylpyrrolidone throughout the methane hydrate formation process. *Energy Fuels*, 29 (4), 2329-2335, doi: 10.1021/acs.energyfuels.5b00145

- Posteraro, D.; Ivall, J.; Maric, M.; Servio, P. 2015. New insights into the effect of polyvinylpyrrolidone (PVP) concentration on methane hydrate growth. 2. Liquid phase methane mole fraction. *Chem. Eng. Sci.*, 126, 91-98, doi: 10.1016/j.ces.2014.12.008

- Verrett, J.; Posteraro, D.; Ivall, J.; Brennan, S.; Servio, P. Understanding the effects of kinetic additives on gas hydrate growth. *Proceedings of the 8th International Conference on Gas Hydrates (ICGH8-2014)*, Beijing, China, 28 July – 1 August, 2014, T1-38.

- Carbone, A.; Ivall, J.; Servio, P. 2012. H-Lw-V equilibrium measurements of pure methane gas in the presence of D-(+)-glucose. *J. Chem. Eng. Data*, 57 (3), 974-977, doi: 10.1021/je201219q

- Design and construction of a morphology setup

- Design and construction of a kinetic/equilibrium setup

Bibliography

Agaliotis, E. M.; Schvezov, C. E.; Rosenberger, M. R.; Ares, A. E. (2012) "A numerical model study of the effect of interface shape on particle pushing" *J. Cryst. Growth* 354 (1) pg. 49-56.

Ajayan, P. M.; Ebbesen, T. W. (1997) "Nanometre-size tubes of carbon" *Rep. Prog. Phys.* 60 (10) pg. 1025-1062.

Ajayan, P. M.; Schadler, L. S.; Braun, P. V. (2003) "Nanocomposite Science and Technology", Wiley-VCH Verlag GmbH & Co. KGaA, Weinheim, Germany.

Amrollahi, A.; Hamidi, A. A.; Rashidi, A. M. (2008) "The effects of temperature, volume fraction and vibration time on the thermo-physical properties of a carbon nanotube suspension (carbon nanofluid)" *Nanotechnology* 19 (31) pg. 315701-(1-8).

Anderson, D. M.; Worster, M. G.; Davis, S. H. (1996) "The case for a dynamic contact angle in containerless solidification" *J. Cryst. Growth* 163 (3) pg. 329-338.

Andrews, J.; Jelley, N. (2013) "Energy Science: Principles, Technologies and Impacts", 2nd Edition. Oxford University Press, Oxford, United Kingdom.

ASTM International (2011) "ASTM E438-92 - Standard Specification for Glasses in Laboratory Apparatus" West Conshohocken, PA, U.S.A.

Baddour, C. E.; Fadlallah, F.; Nasuhoglu, D.; Mitra, R.; Vandsburger, L.; Meunier, J.-L. (2009) "A simple thermal CVD method for carbon nanotube synthesis on stainless steel 304 without the addition of an external catalyst" *Carbon* 47 (1) pg. 313-318.

Baltimore Aircoil Company. "Ice Thermal Storage" Retrieved 2016 from http://www.baltimoreaircoil.com/english/products/ice-thermal-storage

Bartashevich, M. V.; Marchuk, I. V.; Kabov, O. A. (2012) "Numerical simulation of natural convection in a sessile liquid droplet" *Thermophys. Aeromech.* 19 (2) pg. 317-328.

Bartels-Rausch, T.; Bergeron, V.; Cartwright, J. H. E.; Escribano, R.; Finney, J. L.; Grothe, H.; Gutierrez, P. J.; Haapala, J.; Kuhs, W. F.; Pettersson, J. B. C.; Price, S. D.; Sainz-Diaz, C. I.; Stokes, D. J.; Strazzulla, G.; Thomson, E. S.; Trinks, H.; Uras-Aytemiz,

N. (2012) "Ice structures, patterns, and processes: A view across the icefields" *Rev. Mod. Phys.* 84 (2) pg. 885-944.

Bedecarrats, J. P.; Strub, F.; Falcon, B.; Dumas, J. P. (1996) "Phase-change thermal energy storage using spherical capsules: Performance of a test plant" *Int. J. Refrig.* 19 (3) pg. 187-196.

Bénard, H. (1900a) "Swirling movements of cellular structure. Optic study of free surfaces." *C. R. Hebd. Séances Acad. Sci.* 130 pg. 1065-1068.

Bénard, H. (1900b) "Tourbillons cellulaires dans une nappe liquide, 1ère partie. Description générale des phénomènes" *Rev. Gen. Sci. Pures Appl.* 11 pg. 1261-1271.

Berber, S.; Kwon, Y. K.; Tomanek, D. (2000) "Unusually high thermal conductivity of carbon nanotubes" *Phys. Rev. Lett.* 84 (20) pg. 4613-4616.

Bernal, J. D.; Fowler, R. H. (1933) "A theory of water and ionic solution, with particular reference to hydrogen and hydroxyl ions" *J. Chem. Phys.* 1 (8) pg. 515-548.

Bethune, D. S.; Kiang, C. H.; Devries, M. S.; Gorman, G.; Savoy, R.; Vazquez, J.; Beyers, R. (1993) "Cobalt-Catalyzed Growth of Carbon Nanotubes with Single-Atomic-Layerwalls" *Nature* 363 (6430) pg. 605-607.

Block, M. J. (1956) "Surface Tension as the Cause of Bénard Cells and Surface Deformation in a Liquid Film" *Nature* 178 (4534) pg. 650-651.

Bolling, G. F.; Cissé, J. (1971) "A theory for the interaction of particles with a solidifying front" *J. Cryst. Growth* 10 (1) pg. 56-66.

Bouchard, D.; Chang, X.; Chowdhury, I. (2015) "Heteroaggregation of multiwalled carbon nanotubes with sediments" *Environmental Nanotechnology, Monitoring & Management* 4 pg. 42-50.

Bugaje, I. M. (1997) "Enhancing the thermal response of latent heat storage systems" *Int. J. Energy Res.* 21 (9) pg. 759-766.

Bunker, B. C. (1994) "Molecular Mechanisms for Corrosion of Silica and Silicate-Glasses" *J. Non-Cryst. Solids* 179 pg. 300-308.

Buongiorno, J.; Venerus, D. C.; Prabhat, N.; McKrell, T.; Townsend, J.; Christianson, R.; Tolmachev, Y. V.; Keblinski, P.; Hu, L. W.; Alvarado, J. L.; Bang, I. C.; Bishnoi, S. W.; Bonetti, M.; Botz, F.; Cecere, A.; Chang, Y.; Chen, G.; Chen, H. S.; Chung, S. J.; Chyu, M. K.; Das, S. K.; Di Paola, R.; Ding, Y. L.; Dubois, F.; Dzido, G.; Eapen, J.; Escher, W.;

Funfschilling, D.; Galand, Q.; Gao, J. W.; Gharagozloo, P. E.; Goodson, K. E.; Gutierrez, J. G.; Hong, H. P.; Horton, M.; Hwang, K. S.; Iorio, C. S.; Jang, S. P.; Jarzebski, A. B.; Jiang, Y. R.; Jin, L. W.; Kabelac, S.; Kamath, A.; Kedzierski, M. A.; Kieng, L. G.; Kim, C.; Kim, J. H.; Kim, S.; Lee, S. H.; Leong, K. C.; Manna, I.; Michel, B.; Ni, R.; Patel, H. E.; Philip, J.; Poulikakos, D.; Reynaud, C.; Savino, R.; Singh, P. K.; Song, P. X.; Sundararajan, T.; Timofeeva, E.; Tritcak, T.; Turanov, A. N.; Van Vaerenbergh, S.; Wen, D. S.; Witharana, S.; Yang, C.; Yeh, W. H.; Zhao, X. Z.; Zhou, S. Q. (2009) "A benchmark study on the thermal conductivity of nanofluids" *J. Appl. Phys.* 106 (9) pg. 094312-(1-14).

Cahn, J. W.; Hillig, W. B.; Sears, G. W. (1964) "The molecular mechanism of solidification" *Acta Metall.* 12 (12) pg. 1421-1439.

Calmac (2014). "IceBank Energy Storage" Retrieved 2016 from http://www.calmac.com

Cao, G. (2004) "Nanostructures and Nanomaterials: Synthesis, Properties, and Applications", Imperial College Press, London, United Kingdom.

Carbone, A. S.; Ivall, J. R.; Servio, P. D. (2012) "H–Lw–V Equilibrium Measurements of Pure Methane Gas in the Presence of d-(+)-Glucose" *J. Chem. Eng. Data* 57 (3) pg. 974-977.

Carte, A. E. (1961) "Air Bubbles in Ice" *Proc. Phys. Soc.* 77 (3) pg. 757-768.

Chandrasekaran, P.; Cheralathan, M.; Kumaresan, V.; Velraj, R. (2014) "Solidification behavior of water based nanofluid phase change material with a nucleating agent for cool thermal storage system" *Int. J. Refrig.* 41 pg. 157-163.

Chandrasekhar, S. (1961) "Hydrodynamic and hydromagnetic stability", Clarendon Press, Oxford, United Kingdom.

Chang, R. (2000) "Physical Chemistry for the Chemical and Biological Sciences", University Science Books, Sausalito, CA, U.S.A.

Chaudhary, G.; Li, R. (2014) "Freezing of water droplets on solid surfaces: An experimental and numerical study" *Exp. Therm. Fluid Sci.* 57 pg. 86-93.

Cheng, X. L.; Zhong, J.; Meng, J.; Yang, M.; Jia, F. M.; Xu, Z.; Kong, H.; Xu, H. Y. (2011) "Characterization of Multiwalled Carbon Nanotubes Dispersing in Water and Association with Biological Effects" *J. Nanomater.* 2011 pg. 1-12.

Cheon, S.; Kihm, K. D.; Kim, H. G.; Lim, G.; Park, J. S.; Lee, J. S. (2014) "How to Reliably Determine the Complex Refractive Index (RI) of Graphene by Using Two Independent Measurement Constraints" *Sci. Rep.* 4 pg. 1-8.

Choi, S. U. S.; Eastman, J. A. (1995) "Enhancing thermal conductivity of fluids with nanoparticles" *ASME International Mechanical Engineering Congress and Exhibition*, San Francisco, CA, U.S.A., 12-17 November.

Choi, T. Y.; Poulikakos, D.; Tharian, J.; Sennhauser, U. (2005) "Measurement of thermal conductivity of individual multiwalled carbon nanotubes by the 3-omega method" *Appl. Phys. Lett.* 87 (1) pg. 1589-1593.

Cissé, J.; Bolling, G. F. (1971) "A study of the trapping and rejection of insoluble particles during the freezing of water" *J. Cryst. Growth* 10 (1) pg. 67-76.

Clift, R.; Grace, J. R.; Weber, M. E. (2005) "Bubbles, Drops, and Particles", Dover Publications, Mineola, NY, U.S.A.

Cryopak. Retrieved 2016 from http://www.cryopak.com/packaging-and-refrigerants/

Das, S. K.; Choi, S. U. S.; Yu, W.; Pradeep, T. (2007) "Nanofluids: Science and Technology", John Wiley & Sons, Inc., Hoboken, NJ, U.S.A.

Dash, S.; Chandramohan, A.; Weibel, J. A.; Garimella, S. V. (2014) "Buoyancy-induced on-the-spot mixing in droplets evaporating on nonwetting surfaces" *Phys. Rev. E: Stat., Nonlinear, Soft Matter Phys.* 90 (6) pg. 062407-(1-8).

De Volder, M. F. L.; Tawfick, S. H.; Baughman, R. H.; Hart, A. J. (2013) "Carbon Nanotubes: Present and Future Commercial Applications" *Science* 339 (6119) pg. 535-539.

Derjaguin, B. V.; Landau, L. (1941) "Theory of the stability of strongly charged lyophobic sols and of the adhesion of strongly charged particles in solutions of electrolytes" *Acta Physicochim. URSS* 14 pg. 633-662.

Dincer, I.; Rosen, M. A. (2001) "Energetic, environmental and economic aspects of thermal energy storage systems for cooling capacity" *Appl. Therm. Eng.* 21 (11) pg. 1105-1117.

Ding, Y. L.; Alias, H.; Wen, D. S.; Williams, R. A. (2006) "Heat transfer of aqueous suspensions of carbon nanotubes (CNT nanofluids)" *Int. J. Heat Mass Transfer* 49 (1-2) pg. 240-250.

Dresselhaus, M. S.; Dresselhaus, G.; Avouris, P. (2001) "Carbon Nanotubes: Synthesis, Structure, Properties, and Applications", Springer-Verlag, Berlin, Germany.

Dumore, J. M.; Merk, H. J.; Prins, J. A. (1953) "Heat Transfer from Water to Ice by Thermal Convection" *Nature* 172 (4375) pg. 460-461.

Eaves, J. D.; Loparo, J. J.; Fecko, C. J.; Roberts, S. T.; Tokmakoff, A.; Geissler, P. L. (2005) "Hydrogen bonds in liquid water are broken only fleetingly" *Proc. Natl. Acad. Sci. U. S. A.* 102 (37) pg. 13019-13022.

Edie, D. D.; Sandell, C. G.; Mullins, J. C. (1983) "Crystal-Growth Velocity of Sodium-Salt Hydrates" *J. Chem. Eng. Data* 28 (1) pg. 19-23.

Engel, P. A. (1978) "Impact wear of materials", 2nd Edition. Elsevier Scientific Pub. Co., Amsterdam, the Netherlands.

Estellé, P.; Halelfadl, S.; Maré, T. (2015) "Thermal conductivity of CNT water based nanofluids : Experimental trends and models overview" *J. Therm. Eng. (Istanbul, Turk.)* 1 (2) pg. 381 - 390.

Evans, J. (2007) "Manufacturing the carbon nanotube market." Royal Society of Chemistry, November, from http://www.rsc.org/chemistryworld/Issues/2007/November/ManufacturingCarbonNanotubeMarket.asp

Evans, W. S. (1998) "Ice storage cooling for campus expansion" *ASHRAE J.* 40 (4) pg. 66-68.

Evapco. Retrieved 2016 from http://www.evapco.com/products/thermal_ice_storage

Falenty, A.; Hansen, T. C.; Kuhs, W. F. (2014) "Formation and properties of ice XVI obtained by emptying a type sII clathrate hydrate" *Nature* 516 (7530) pg. 231-237.

Fan, L.; Khodadadi, J. M. (2012) "A Theoretical and Experimental Investigation of Unidirectional Freezing of Nanoparticle-Enhanced Phase Change Materials" *J. Heat Transfer* 134 (9) pg. 092301-(1-9).

Feuillebois, F.; Lasek, A.; Creismeas, P.; Pigeonneau, F.; Szaniawski, A. (1995) "Freezing of a Subcooled Liquid Droplet" *J. Colloid Interface Sci.* 169 (1) pg. 90-102.

Fletcher, N. H. (1970) "The Chemical Physics of Ice", Cambridge University Press, New York, NY, U.S.A.

Fukai, J.; Kanou, M.; Kodama, Y.; Miyatake, O. (2000) "Thermal conductivity enhancement of energy storage media using carbon fibers" *Energy Convers. Manage.* 41 (14) pg. 1543-1556.

Fukusako, S.; Yamada, M. (1993) "Recent Advances in Research on Water-Freezing and Ice-Melting Problems" *Exp. Therm. Fluid Sci.* 6 (1) pg. 90-105.

Garvin, J. W.; Udaykumar, H. S. (2004) "Drag on a particle being pushed by a solidification front and its dependence on thermal conductivities" *J. Cryst. Growth* 267 (3-4) pg. 724-737.

Garvin, J. W.; Yang, Y.; Udaykumar, H. S. (2007a) "Multiscale modeling of particle-solidification front dynamics, Part I: Methodology" *Int. J. Heat Mass Transfer* 50 (15-16) pg. 2952-2968.

Garvin, J. W.; Yang, Y.; Udaykumar, H. S. (2007b) "Multiscale modeling of particle-solidification front dynamics. Part II: Pushing-engulfment transition" *Int. J. Heat Mass Transfer* 50 (15-16) pg. 2969-2980.

Geissler, P. L.; Dellago, C.; Chandler, D.; Hutter, J.; Parrinello, M. (2001) "Autoionization in liquid water" *Science* 291 (5511) pg. 2121-2124.

Ghadimi, A.; Saidur, R.; Metselaar, H. S. C. (2011) "A review of nanofluid stability properties and characterization in stationary conditions" *Int. J. Heat Mass Transfer* 54 (17-18) pg. 4051-4068.

Girard, F.; Antoni, M.; Faure, S.; Steinchen, A. (2006) "Evaporation and Marangoni driven convection in small heated water droplets" *Langmuir* 22 (26) pg. 11085-11091.

Glicksman, M. E.; Mizenko, L. M.; Rettenmayer, M. E.; Marsh, S. P. (1994) "Dendritic Solidification of Undercooled Melts - Mushy Zone Recalescence Dynamics" *Mater. Sci. Eng., A* 178 (1-2) pg. 137-146.

Golnabi, H. (2012) "Carbon nanotube research developments in terms of published papers and patents, synthesis and production" *Sci. Iran.* 19 (6) pg. 2012-2022.

Griscom, D. L.; Hosono, H.; Bunker, B. C. (1994) "Molecular mechanisms for corrosion of silica and silicate glasses" *J. Non-Cryst. Solids: Proceedings of the First PAC RIM Meeting on Glass and Optical Materials* 179 pg. 300-308.

Hallett, J. (1964) "Experimental Studies of the Crystallization of Supercooled Water" *J. Atmos. Sci.* 21 (6) pg. 671-682.

Hasnain, S. M. (1998) "Review on sustainable thermal energy storage technologies, part I: Heat storage materials and techniques" *Energy Convers. Manage.* 39 (11) pg. 1127-1138.

He, Y. R.; Wang, S. F.; Ma, J. J.; Tian, F. L.; Ren, Y. T. (2011) "Experimental Study on the Light-Heat Conversion Characteristics of Nanofluids" *Nanosci. Nanotechnol. Lett.* 3 (4) pg. 494-496.

Hegseth, J. J.; Rashidnia, N.; Chai, A. (1996) "Natural convection in droplet evaporation" *Phys. Rev. E: Stat., Nonlinear, Soft Matter Phys.* 54 (2) pg. 1640-1644.

Heneghan, A. F.; Wilson, P. W.; Wang, G. M.; Haymet, A. D. J. (2001) "Liquid-to-crystal nucleation: Automated lag-time apparatus to study supercooled liquids" *J. Chem. Phys.* 115 (16) pg. 7599-7608.

Hillig, W. B.; Turnbull, D. (1956) "Theory of Crystal Growth in Undercooled Pure Liquids" *J. Chem. Phys.* 24 (4) pg. 914-914.

Hiura, H.; Ebbesen, T. W.; Tanigaki, K. (1995) "Opening and Purification of Carbon Nanotubes in High Yields" *Adv. Mater.* 7 (3) pg. 275-276.

Hordy, N. (2014) "Plasma Functionalized Carbon Nanotubes Suspensions for High Temperature Direct Absorption Solar Thermal Energy Harvesting" Doctoral Thesis, McGill University.

Hordy, N.; Coulombe, S.; Meunier, J.-L. (2013a) "Plasma Functionalization of Carbon Nanotubes for the Synthesis of Stable Aqueous Nanofluids and Poly(vinyl alcohol) Nanocomposites" *Plasma Processes Polym.* 10 (2) pg. 110-118.

Hordy, N.; Mendoza-Gonzalez, N.-Y.; Coulombe, S.; Meunier, J.-L. (2013b) "The effect of carbon input on the morphology and attachment of carbon nanotubes grown directly from stainless steel" *Carbon* 63 pg. 348-357.

Hordy, N.; Meunier, J. L.; Coulombe, S. (2015) "Thermal Stability of Plasma Generated Oxygenated Functionalities on Carbon Nanotubes" *Plasma Processes Polym.* 12 (6) pg. 533-544.

Hordy, N.; Rabilloud, D.; Meunier, J.-L.; Coulombe, S. (2014) "High temperature and long-term stability of carbon nanotube nanofluids for direct absorption solar thermal collectors" *Sol. Energy* 105 pg. 82-90.

Hu, H.; Argyropoulos, S. A. (1996) "Mathematical modelling of solidification and melting: A review" *Modell. Simul. Mater. Sci. Eng.* 4 (4) pg. 371-396.

Hu, H.; Larson, R. G. (2005) "Analysis of the effects of Marangoni stresses on the microflow in an evaporating sessile droplet" *Langmuir* 21 (9) pg. 3972-80.

IceEnergy. Retrieved 2016 from https://www.ice-energy.com

Iijima, S. (1991) "Helical Microtubules of Graphitic Carbon" *Nature* 354 pg. 56-58.

Iijima, S. (1993) "Growth of Carbon Nanotubes" *Mater. Sci. Eng., B* 19 (1-2) pg. 172-180.

Ivall, J.; Hachem, M.; Coulombe, S.; Servio, P. (2015a) "Behavior of Surface-Functionalized Multiwall Carbon Nanotube Nanofluids during Phase Change from Liquid Water to Solid Ice" *Cryst. Growth Des.* 15 (8) pg. 3969-3982.

Ivall, J.; Langlois-Rahme, G.; Coulombe, S.; Servio, P. (2016a) "Quantitative stability analyses of multiwall carbon nanotube nanofluids following water/ice phase change cycling " *Nanotechnology* pg. (Submitted).

Ivall, J.; Pasieka, J.; Posteraro, D.; Servio, P. (2015b) "Profiling the Concentration of the Kinetic Inhibitor Polyvinylpyrrolidone throughout the Methane Hydrate Formation Process" *Energy & Fuels* 29 (4) pg. 2329-2335.

Ivall, J.; Renault-Crispo, J.-S.; Coulombe, S.; Servio, P. (2016b) "Ice-dependent liquid-phase convective cells during the melting of frozen sessile droplets containing water and multiwall carbon nanotubes" *Int. J. Heat Mass Transfer* 101 pg. 27-37.

Jia, L. S.; Peng, L.; Chen, Y.; Wang, S. G.; Mo, S. P.; Li, X. (2014) "Solidification behaviors of water-based nanofluids" *Gongneng Cailiao / Journal of Functional Materials* 45 (9) pg. 07001-07005.

Jiang, H. F.; Zhang, Q.; Shi, L. (2015) "Effective thermal conductivity of carbon nanotube-based nanofluid" *J. Taiwan Inst. Chem. Eng.* 55 pg. 76-81.

Jin, Z. Y.; Jin, S. Y.; Yang, Z. G. (2013) "An experimental investigation into the icing and melting process of a water droplet impinging onto a superhydrophobic surface" *Sci. China: Phys., Mech. Astron.* 56 (11) pg. 2047-2053.

Jones, D. R. H.; Ashby, M. F. (2013) "Engineering Materials Volume 2: An Introduction to Microstructures, Processing and Design", 2nd Edition. Butterworth-Heinemann, Oxford, United Kingdom.

Jorge, L.; Coulombe, S.; Girard-Lauriault, P.-L. (2015) "Nanofluids Containing MWCNTs Coated with Nitrogen-Rich Plasma Polymer Films for CO2 Absorption in Aqueous Medium" *Plasma Processes Polym.* 12 (11) pg. 1311-1321.

Jorio, A.; Dresselhaus, M. S.; Dresselhaus, G. (2008) "Carbon Nanotubes: Advanced Topics in the Synthesis, Structure, Properties and Applications", Springer-Verlag, Berlin, Germany.

Kelley, D. H.; Ouellette, N. T. (2011) "Using particle tracking to measure flow instabilities in an undergraduate laboratory experiment" *Am. J. Phys.* 79 (3) pg. 267-273.

Kim, B.; Park, H.; Sigmund, W. M. (2003) "Electrostatic interactions between shortened multiwall carbon nanotubes and polyelectrolytes" *Langmuir* 19 (6) pg. 2525-2527.

Kim, N. J.; Park, S. S.; Kim, H. T.; Chun, W. (2011) "A comparative study on the enhanced formation of methane hydrate using CM-95 and CM-100 MWCNTs" *Int. Commun. Heat Mass Transfer* 38 (1) pg. 31-36.

Kim, P.; Shi, L.; Majumdar, A.; McEuen, P. L. (2001) "Thermal transport measurements of individual multiwalled nanotubes" *Phys. Rev. Lett.* 87 (21) pg. 215502-(1-4).

King, W. D.; Fletcher, N. H. (1973) "Pressures and stresses in freezing water drops" *J. Phys. D: Appl. Phys.* 6 (18) pg. 2157-2173.

Korber, C. (1988) "Phenomena at the Advancing Ice Liquid Interface - Solutes, Particles and Biological Cells" *Q. Rev. Biophys.* 21 (2) pg. 229-298.

Korber, C.; Rau, G.; Cosman, M. D.; Cravalho, E. G. (1985) "Interaction of Particles and a Moving Ice-Liquid Interface" *J. Cryst. Growth* 72 pg. 649-662.

Kumaresan, V.; Chandrasekaran, P.; Nanda, M.; Maini, A. K.; Velraj, R. (2013) "Role of PCM based nanofluids for energy efficient cool thermal storage system" *Int. J. Refrig.* 36 (6) pg. 1641-1647.

Kumaresan, V.; Velraj, R.; Das, S. K. (2012) "The effect of carbon nanotubes in enhancing the thermal transport properties of PCM during solidification" *Heat Mass Transfer* 48 (8) pg. 1345-1355.

Lamas, B.; Abreu, B.; Fonseca, A.; Martins, N.; Oliveira, M. (2012) "Assessing colloidal stability of long term MWCNTs based nanofluids" *J. Colloid Interface Sci.* 381 pg. 17-23.

Ledieu, A.; Devreux, F.; Barboux, P.; Sicard, L.; Spalla, O. (2004) "Leaching of borosilicate glasses. I. Experiments" *J. Non-Cryst. Solids* 343 (1-3) pg. 3-12.

Lindenmeyer, C. S.; Orrok, G. T.; Jackson, K. A.; Chalmers, B. (1957) "Rate of Growth of Ice Crystals in Supercooled Water" *J. Chem. Phys.* 27 (3) pg. 822-823.

Ling, E. J.; Uong, V.; Renault-Crispo, J. S.; Kietzig, A. M.; Servio, P. (2016) "Reducing Ice Adhesion on Nonsmooth Metallic Surfaces: Wettability and Topography Effects" *ACS Appl. Mater. Interfaces* 8 (13) pg. 8789-8800.

Lynden-Bell, R. M.; Morris, S. C.; Barrow, J. D.; Finney, J. L.; Harper Jr., C. L. (2010) "Water and Life: The Unique Properties of H2O", CRC Press, Boca Raton, FL, U.S.A.

MacDevette, M. M.; Myers, T. G. (2016) "Nanofluids: An innovative phase change material for cold storage systems?" *Int. J. Heat Mass Transfer* 92 pg. 550-557.

Maxwell, J. C. (1881) "A Treatise on Electricity and Magnetism", 2nd Edition. Clarendon Press, Oxford, United Kingdom.

Menini, R.; Farzaneh, M. (2011) "Advanced Icephobic Coatings" *J. Adhes. Sci. Technol.* 25 (9) pg. 971-992.

Merk, H. J. (1954) "The Influence of Melting and Anomalous Expansion on the Thermal Convection in Laminar Boundary Layers" *Appl. Sci. Res., Sect. A* 4 (5) pg. 435-452.

Missana, T.; Adell, A. (2000) "On the Applicability of DLVO Theory to the Prediction of Clay Colloids Stability" *J. Colloid Interface Sci.* 230 (1) pg. 150-156.

Mo, S. P.; Chen, Y.; Yang, J. Y.; Luo, X. L. (2011) "Experimental Study on Solidification Behavior of Carbon Nanotube Nanofluid" *Adv. Mater. Res.* 171-172 pg. 333-336.

Mullin, J. W. (2001) "Crystallization", 4th Edition. Elsevier Science, Oxford, United Kingdom.

Murshed, S. M. S.; de Castro, C. A. N. (2014) "Superior thermal features of carbon nanotubes-based nanofluids - A review" *Renewable Sustainable Energy Rev.* 37 pg. 155-167.

Nield, D. A. (1964) "Surface Tension and Buoyancy Effects in Cellular Convection" *J. Fluid Mech.* 19 (3) pg. 341-352.

Okawa, S.; Saito, A.; Minami, R. (2001) "Solidification phenomenon of the supercooled water containing solid particles" *Int. J. Refrig.* 24 (1) pg. 108-117.

Oro, E.; de Gracia, A.; Castell, A.; Farid, M. M.; Cabeza, L. F. (2012) "Review on phase change materials (PCMs) for cold thermal energy storage applications" *Appl. Energy* 99 pg. 513-533.

Pan, Z. C.; Sun, H.; Zhang, Y.; Chen, C. F. (2009) "Harder than Diamond: Superior Indentation Strength of Wurtzite BN and Lonsdaleite" *Phys. Rev. Lett.* 102 (5) pg. 055503-(1-4).

Parent, O.; Ilinca, A. (2011) "Anti-icing and de-icing techniques for wind turbines: Critical review" *Cold Reg. Sci. Technol.* 65 (1) pg. 88-96.

Park, K. J.; Kang, D. G.; Jung, D.; Shim, S. E. (2011) "Nucleate boiling heat transfer in nanofluids with carbon nanotubes up to critical heat fluxes" *J. Mech. Sci. Technol.* 25 (10) pg. 2647-2655.

Park, S. S.; Lee, S. B.; Kim, N. J. (2010) "Effect of multi-walled carbon nanotubes on methane hydrate formation" *J. Ind. Eng. Chem.* 16 (4) pg. 551-555.

Pasieka, J.; Coulombe, S.; Servio, P. (2013a) "Investigating the effects of hydrophobic and hydrophilic multi-wall carbon nanotubes on methane hydrate growth kinetics" *Chem. Eng. Sci.* 104 pg. 998-1002.

Pasieka, J.; Hordy, N.; Coulombe, S.; Servio, P. (2013b) "Measuring the Effect of Multi-Wall Carbon Nanotubes on Tetrahydrofuran–Water Hydrate Front Velocities Using Thermal Imaging" *Cryst. Growth Des.* 13 (9) pg. 4017-4024.

Pasieka, J.; Jorge, L.; Coulombe, S.; Servio, P. (2015) "Effects of As-Produced and Amine-Functionalized Multi-Wall Carbon Nanotubes on Carbon Dioxide Hydrate Formation" *Energy & Fuels* 29 (8) pg. 5259-5266.

Pasieka, J.; Nanua, R.; Coulombe, S.; Servio, P. (2014) "The crystallization of sub-cooled water: Measuring the front velocity and mushy zone composition via thermal imaging" *Int. J. Heat Mass Transfer* 77 pg. 940-945.

Pauling, L. (1935) "The structure and entropy of ice and of other crystals with some randomness of atomic arrangement" *J. Am. Chem. Soc.* 57 pg. 2680-2684.

PCM Products. Retrieved 2016 from http://www.pcmproducts.net/Phase-Change-Material-Solutions.htm

Pearson, J. R. A. (1958) "On Convection Cells Induced by Surface Tension" *J. Fluid Mech.* 4 (5) pg. 489-500.

Peppin, S. S.; Wettlaufer, J. S.; Worster, M. G. (2008) "Experimental verification of morphological instability in freezing aqueous colloidal suspensions" *Phys. Rev. Lett.* 100 (23) pg. 238301-(1-4).

Peppin, S. S. L.; Worster, M. G.; Wettlaufer, J. S. (2007) "Morphological instability in freezing colloidal suspensions" *Proc. R. Soc. A* 463 (2079) pg. 723-733.

Perry, R. H.; Green, D. W. (1997) "Perry's Chemical Engineers' Handbook", 7th Edition. McGraw-Hill Professional, New York, NY, U.S.A.

Petrenko, V. F.; Whitworth, R. W. (2002). Physics of ice. Oxford, United Kingdom, Oxford University Press.

Phuoc, T. X.; Massoudi, M.; Chen, R. H. (2011) "Viscosity and thermal conductivity of nanofluids containing multi-walled carbon nanotubes stabilized by chitosan" *Int. J. Therm. Sci.* 50 (1) pg. 12-18.

Posteraro, D.; Ivall, J.; Maric, M.; Servio, P. (2015) "New insights into the effect of polyvinylpyrrolidone (PVP) concentration on methane hydrate growth. 2. Liquid phase methane mole fraction" *Chem. Eng. Sci.* 126 pg. 91-98.

Potschke, J.; Rogge, V. (1989) "On the Behavior of Foreign Particles at an Advancing Solid Liquid Interface" *J. Cryst. Growth* 94 (3) pg. 726-738.

Prasad, A.; Lin, A. T. H.; Rao, V. R.; Seshia, A. A. (2014) "Monitoring sessile droplet evaporation on a micromechanical device" *Analyst* 139 (21) pg. 5538-5546.

Prasek, J.; Drbohlavova, J.; Chomoucka, J.; Hubalek, J.; Jasek, O.; Adam, V.; Kizek, R. (2011) "Methods for carbon nanotubes synthesis-review" *J. Mater. Chem.* 21 (40) pg. 15872-15884.

Pruppacher, H. R. (1967a) "Interpretation of Experimentally Determined Growth Rates of Ice Crystals in Supercooled Water" *J. Chem. Phys.* 47 (5) pg. 1807-1813.

Pruppacher, H. R. (1967b) "On Growth of Ice Crystals in Supercooled Water and Aqueous Solution Drops" *Pure Appl. Geophys.* 68 (1) pg. 186-195.

Qian, D.; Wagner, G. J.; Liu, W. K.; Yu, M.-F.; Ruoff, R. S. (2002) "Mechanics of carbon nanotubes" *Appl. Mech. Rev.* 55 (6) pg. 495-533.

Rayleigh, L. (1916) "On convection currents in a horizontal layer of fluid, when the higher temperature is on the under side" *Philos. Mag.* 32 (192) pg. 529-546.

Rempel, A. W.; Worster, M. G. (1999) "The interaction between a particle and an advancing solidification front" *J. Cryst. Growth* 205 (3) pg. 427-440.

Ryglowski, B. K.; Pollak, R. D.; Kwon, Y. W. (2010) "Characterizing the Stability of Carbon Nanotube-Enhanced Water as a Phase Change Material for Thermal Management Systems" *J. Therm. Sci. Eng. Appl.* 2 (4) pg. 041007-(1-6).

Saito, R.; Matsuo, R.; Kimura, T.; Dresselhaus, G.; Dresselhaus, M. S. (2001) "Anomalous potential barrier of double-wall carbon nanotube" *Chem. Phys. Lett.* 348 (3-4) pg. 187-193.

Sanz, A.; Meseguer, J.; Mayo, L. (1987) "The influence of gravity on the solidification of a drop" *J. Cryst. Growth* 82 (1–2) pg. 81-88.

Schatz, M. F.; Neitzel, G. P. (2001) "Experiments on thermocapillary instabilities" *Annu. Rev. Fluid Mech.* 33 pg. 93-127.

Schatz, M. F.; Vanhook, S. J.; Mccormick, W. D.; Swift, J. B.; Swinney, H. L. (1995) "Onset of Surface-Tension-Driven Benard Convection" *Phys. Rev. Lett.* 75 (10) pg. 1938-1941.

Schenk, J.; Schenkels, F. A. M. (1968) "Thermal Free Convection from an Ice Sphere in Water" *Appl. Sci. Res., Sect. A* 19 (6) pg. 465-476.

Scholander, P. F.; Flagg, W.; Hock, R. J.; Irving, L. (1953) "Studies on the physiology of frozen plants and animals in the Arctic" *J. Cell. Comp. Physiol.* 42 (Suppl. 1) pg. 1-56.

Scriven, L. E.; Sternling, C. V. (1964) "On Cellular Convection Driven by Surface-Tension Gradients - Effects of Mean Surface Tension and Surface Viscosity" *J. Fluid Mech.* 19 (3) pg. 321-340.

Shenogin, S.; Bodapati, A.; Xue, L.; Ozisik, R.; Keblinski, P. (2004) "Effect of chemical functionalization on thermal transport of carbon nanotube composites" *Appl. Phys. Lett.* 85 (12) pg. 2229-2231.

Shieh, Y. T.; Liu, G. L.; Wu, H. H.; Lee, C. C. (2007) "Effects of polarity and pH on the solubility of acid-treated carbon nanotubes in different media" *Carbon* 45 (9) pg. 1880-1890.

Siegel, R. (1977) "Solidification of low conductivity material containing dispersed high conductivity particles" *Int. J. Heat Mass Transfer* 20 (10) pg. 1087-1089.

Sloan, E. D. K. C. A. (2008) "Clathrate hydrates of natural gases", 3rd Edition. CRC Press, Boca Raton, FL, U.S.A.

Smith, B.; Wepasnick, K.; Schrote, K. E.; Bertele, A. H.; Ball, W. P.; O'Melia, C.; Fairbrother, D. H. (2009a) "Colloidal Properties of Aqueous Suspensions of Acid-Treated, Multi-Walled Carbon Nanotubes" *Environ. Sci. Technol.* 43 (3) pg. 819-825.

Smith, B.; Wepasnick, K.; Schrote, K. E.; Cho, H. H.; Ball, W. P.; Fairbrother, D. H. (2009b) "Influence of surface oxides on the colloidal stability of multi-walled carbon nanotubes: a structure-property relationship" *Langmuir* 25 (17) pg. 9767-76.

Sofrigam. Retrieved 2016 from http://www.sofrigam.com/insulated-cooling-packaging

Sokolov, S. V.; Tschulik, K.; Batchelor-McAuley, C.; Jurkschat, K.; Compton, R. G. (2015) "Reversible or Not? Distinguishing Agglomeration and Aggregation at the Nanoscale" *Anal. Chem.* 87 (19) pg. 10033-10039.

Sparrow, E. M.; Lee, L.; Shamsundar, N. (1976) "Convective Instability in a Melt Layer Heated from Below" *J. Heat Transfer* 98 (1) pg. 88-94.

Squires, T. M.; Quake, S. R. (2005) "Microfluidics: Fluid physics at the nanoliter scale" *Rev. Mod. Phys.* 77 (3) pg. 977-1026.

Stokes, G. G. (1851) "On the Effect of the Internal Friction of Fluids on the Motion of Pendulums " *Trans. Cambridge Philos. Soc.* 9 pg. 8-106.

Sun, Z. S.; Tien, C.; Yen, Y. C. (1969) "Thermal Instability of a Horizontal Layer of Liquid with Maximum Density" *AIChE J.* 15 (6) pg. 910-915.

Tam, D.; von Arnim, V.; McKinley, G. H.; Hosoi, A. E. (2009) "Marangoni convection in droplets on superhydrophobic surfaces" *J. Fluid Mech.* 624 pg. 101-123.

Tasis, D.; Tagmatarchis, N.; Bianco, A.; Prato, M. (2006) "Chemistry of carbon nanotubes" *Chem. Rev.* 106 (3) pg. 1105-1136.

Taylor, R.; Coulombe, S.; Otanicar, T.; Phelan, P.; Gunawan, A.; Lv, W.; Rosengarten, G.; Prasher, R.; Tyagi, H. (2013) "Small particles, big impacts: A review of the diverse applications of nanofluids" *J. Appl. Phys.* 113 (1) pg. 011301-(1-19).

Teng, T. P.; Fang, Y. B.; Hsu, Y. C.; Lin, L. (2014) "Evaluating Stability of Aqueous Multiwalled Carbon Nanotube Nanofluids by Using Different Stabilizers" *J. Nanomater.* 2014 pg. 1-15.

Thomas, S. K.; Cassoni, R. P.; MacArthur, C. D. (1996) "Aircraft anti-icing and de-icing techniques and modeling" *J. Aircr.* 33 (5) pg. 841-854.

Transparency Market Research (2016) "Carbon Nanotubes Market – Global Industry Analysis, Size, Share, Growth, Trends and Forecast 2015 – 2023".

Tseng, W. S.; Tseng, C. Y.; Chuang, P. K.; Lo, A. Y.; Kuo, C. T. (2008) "A High Efficiency Surface Modification Process for Multiwalled Carbon Nanotubes by Electron Cyclotron Resonance Plasma" *J. Phys. Chem. C* 112 (47) pg. 18431-18436.

Tyson, N. d. (2014) "Death by Black Hole: And Other Cosmic Quandaries", W.W. Norton & Company, New York, NY, U.S.A.

Vaisman, L.; Wagner, H. D.; Marom, G. (2006) "The role of surfactants in dispersion of carbon nanotubes" *Adv. Colloid Interface Sci.* 128 pg. 37-46.

Vandsburger, L.; Swanson, E. J.; Tavares, J.; Meunier, J.-L.; Coulombe, S. (2009) "Stabilized aqueous dispersion of multi-walled carbon nanotubes obtained by RF glow-discharge treatment" *J. Nanopart. Res.* 11 (7) pg. 1817-1822.

Vanier, C. R.; Tien, C. (1970) "Free Convection Melting of Ice Spheres" *AIChE J.* 16 (1) pg. 76-82.

Verwey, E. J. W.; Overbeek, J. T. G. (1948) "Theory of the Stability of Lyophobic Colloids: The Interaction of Sol Particles Having an Electric Double Layer", Elsevier, New York, NY, U.S.A.

Visagie, P. J. (1969) "Pressures inside freezing water drops" *J. Glaciol.* 8 (53) pg. 301-309.

Walford, M. E. R.; Hargreaves, D. M.; Stuartsmith, S.; Lowson, M. (1991) "Freezing of Water Drops on a Cold Surface" *J. Glaciol.* 37 (125) pg. 47-50.

Walton, H.; Judd, R. C. (1913) "The Velocity of Crystallization of Under cooled Water" *J. Phys. Chem.* 18 (9) pg. 722-728.

Wang, J.; Xie, H.; Xin, Z. (2008) "Thermal properties of heat storage composites containing multiwalled carbon nanotubes" *J. Appl. Phys.* 104 (11) pg. 113537-(1-5).

Wang, J.; Xie, H.; Xin, Z. (2009) "Thermal properties of paraffin based composites containing multi-walled carbon nanotubes" *Thermochim. Acta* 488 (1–2) pg. 39-42.

Wang, J. T.; Chen, C. F.; Kawazoe, Y. (2013) "New Carbon Allotropes with Helical Chains of Complementary Chirality Connected by Ethene-type pi-Conjugation" *Sci. Rep.* 3 pg. 1-6.

Wang, Z. Q.; Zhao, Y. P. (2012) "In Situ Observation of Thermal Marangoni Convection on the Surface of a Sessile Droplet by Infrared Thermal Imaging" *J. Adhes. Sci. Technol.* 26 (12-17) pg. 2177-2188.

Weber, J. W.; Calado, V. E.; van de Sanden, M. C. M. (2010) "Optical constants of graphene measured by spectroscopic ellipsometry" *Appl. Phys. Lett.* 97 (9) pg. 091904-(1-3).

Wilde, G.; Perepezko, J. H. (2000) "Experimental study of particle incorporation during dendritic solidification" *Mater. Sci. Eng., A* 283 (1–2) pg. 25-37.

Wilson, P. W.; Haymet, A. D. J. (2012) "The Spread of Nucleation Temperatures of a Sample of Supercooled Liquid Is Independent of the Average Nucleation Temperature" *J. Phys. Chem. B* 116 (45) pg. 13472-13475.

Xie, H. Q.; Cai, A.; Wang, X. W. (2007) "Thermal diffusivity and conductivity of multiwalled carbon nanotube arrays" *Phys. Lett. A* 369 (1-2) pg. 120-123.

Xie, H. Q.; Chen, L. F. (2011) "Review on the Preparation and Thermal Performances of Carbon Nanotube Contained Nanofluids" *J. Chem. Eng. Data* 56 (4) pg. 1030-1041.

Xie, H. Q.; Lee, H.; Youn, W.; Choi, M. (2003) "Nanofluids containing multiwalled carbon nanotubes and their enhanced thermal conductivities" *J. Appl. Phys.* 94 (8) pg. 4967-4971.

Xing, M. B.; Yu, J. L.; Wang, R. X. (2016) "Experimental investigation and modelling on the thermal conductivity of CNTs based nanofluids" *Int. J. Therm. Sci.* 104 pg. 404-411.

Yakobson, B. I.; Brabec, C. J.; Bernholc, J. (1996) "Nanomechanics of carbon tubes: Instabilities beyond linear response" *Phys. Rev. Lett.* 76 (14) pg. 2511-2514.

Yen, Y. C. (1968) "Onset of Convection in a Layer of Water Formed by Melting Ice from Below" *Phys. Fluids* 11 (6) pg. 1263-1270.

Yen, Y. C.; Galea, F. (1969) "Onset of Convection in a Water Layer Formed Continuously by Melting Ice" *Phys. Fluids* 12 (3) pg. 509-516.

Yu, M. F.; Lourie, O.; Dyer, M. J.; Moloni, K.; Kelly, T. F.; Ruoff, R. S. (2000) "Strength and breaking mechanism of multiwalled carbon nanotubes under tensile load" *Science* 287 (5453) pg. 637-640.

Yu, W.; Xie, H. Q. (2012) "A Review on Nanofluids: Preparation, Stability Mechanisms, and Applications" *J. Nanomater.* 2012 pg. 1-17.

Zalba, B.; Marin, J. M.; Cabeza, L. F.; Mehling, H. (2003) "Review on thermal energy storage with phase change: materials, heat transfer analysis and applications" *Appl. Therm. Eng*. 23 (3) pg. 251-283.

Zeng, J. L.; Liu, Y. Y.; Cao, Z. X.; Zhang, J.; Zhang, Z. H.; Sun, L. X.; Xu, F. (2008) "Thermal conductivity enhancement of MWNTs on the PANI/tetradecanol form-stable PCM" *J. Therm. Anal. Calorim*. 91 (2) pg. 443-446.

Zeng, Y.; Fan, L. W.; Xiao, Y. Q.; Yu, Z. T.; Cen, K. F. (2013) "An experimental investigation of melting of nanoparticle-enhanced phase change materials (NePCMs) in a bottom-heated vertical cylindrical cavity" *Int. J. Heat Mass Transfer* 66 pg. 111-117.

Zheng, L. X.; O'Connell, M. J.; Doorn, S. K.; Liao, X. Z.; Zhao, Y. H.; Akhadov, E. A.; Hoffbauer, M. A.; Roop, B. J.; Jia, Q. X.; Dye, R. C.; Peterson, D. E.; Huang, S. M.; Liu, J.; Zhu, Y. T. (2004) "Ultralong single-wall carbon nanotubes" *Nat. Mater*. 3 (10) pg. 673-676.

Appendix

Appendix A

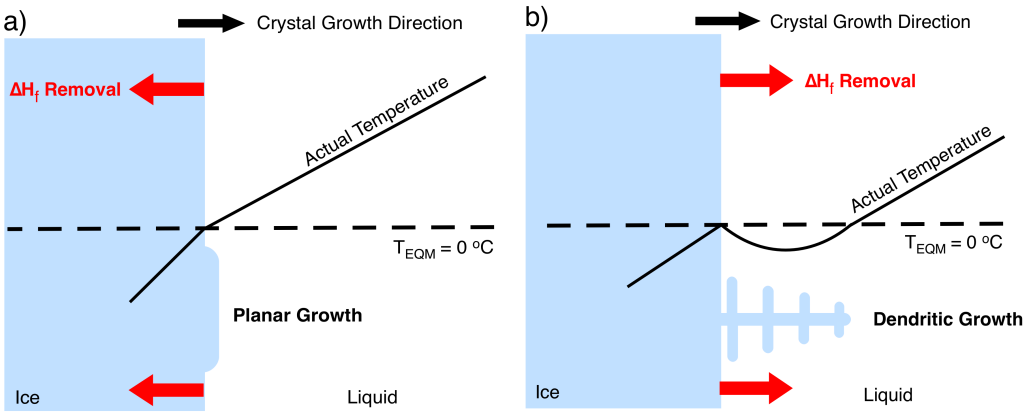

Figure A1. Temperature profiles in a solidifying system leading to a) planar; b) dendritic growth.

The appearance of embedded air pockets in the ice is due to a eutectic transformation of the water/air mixture. Water typically contains ~ 0.003 wt. % dissolved air (Jones and Ashby, 2013). In a planar growth geometry such as this, the buildup of air in the liquid ahead of the solid as a result of its rejection from ice triggers bubble formation when the concentration reaches the eutectic point at ~ 0.0038 wt. % air (at – 0.0024 °C) (Jones and Ashby, 2013). The liquid was not purposefully degassed for these experiments since most water contains some amount of dissolved air, and maintaining purity is difficult owing to the solubility of air in water and the amount of sample handling during experimentation. However, the sonication process used for MWCNT removal from meshes (and for resuspension) is a common protocol to degas liquids and may have already degassed the samples to a certain degree.

Appendix B

The information provided is a reproduction of the Supplemental Materials accompanying the article "Ice-dependent liquid-phase convective cells during the melting of frozen sessile droplets containing water and multiwall carbon nanotubes" that constitutes Chapter 4. This article was accepted by the *International Journal of Heat and Mass Transfer* (2016).

A video of the convective process occurring in a 50 ppm f-MWCNT nanofluid droplet melted at a substrate temperature of 20 °C will be posted by McGill University Graduate and Postdoctoral Services (GPS) on the Mycourses website. Please contact thesis.gps@mcgill.ca for further information.

Appendix C

The information provided is a reproduction of the Supplemental Materials accompanying the article "Quantitative Analysis into the Stability of Aqueous Oxygen-Functionalized Multiwall Carbon Nanotube Nanofluids after Liquid/Solid Phase Change Cycling" that constitutes Chapter 5. This manuscript was submitted to *Nanotechnology* (2016).

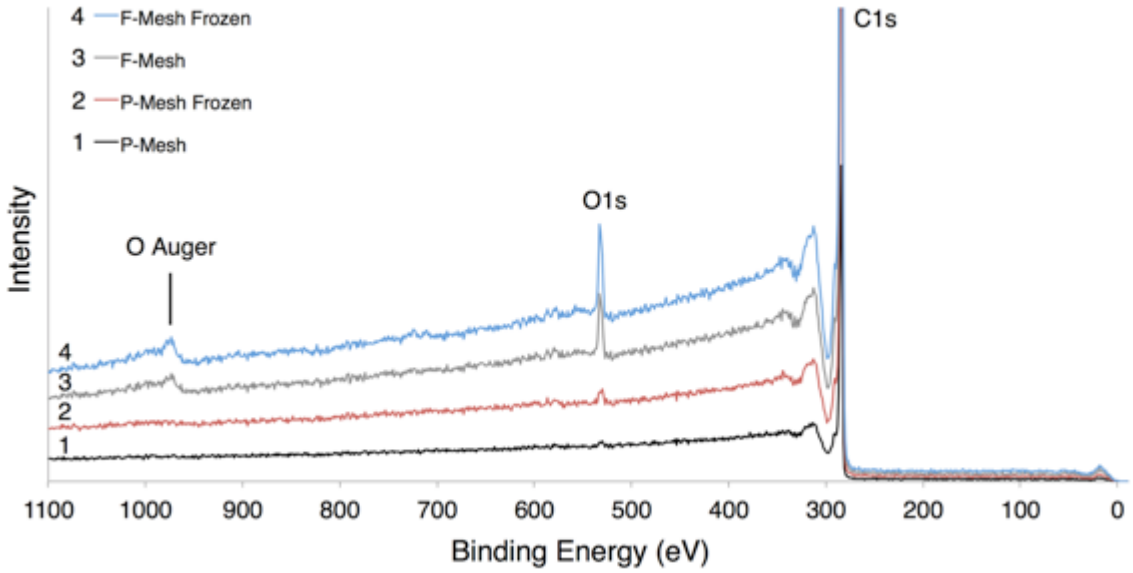

Figure C1: Sample XPS survey spectra used to calculated compositions in Table 4. (1) mesh covered with as-produced p-MWCNTs, (2) same mesh type but subjected to 10 freeze/thaw cycles, (3) mesh covered with f-MWCNTs, and (4) same mesh type but subjected to 10 freeze/thaw cycles.